©2009

JING-YI ZHENG

MICROSCOPY WITH SPATIAL FILTERING

FOR MONITORING SUBCELLULAR MORPHOLOGY

By

JING-YI ZHENG

A Dissertation submitted to the

Graduate School-New Brunswick

Rutgers, The State University of New Jersey

and

The Graduate School of Biomedical Sciences

University of Medicine and Dentistry of New Jersey

in partial fulfillment of the requirements

for the degree of

Doctor of Philosophy

Graduate Program in Biomedical Engineering

written under the direction of

Nada N. Boustany

and approved by

_____

_____

_____

_____

_____

New Brunswick, New Jersey

October 2009

ABSTRACT OF THE DISSERTATION

Microscopy with Spatial Filtering

for Monitoring Subcellular Morphology

By Jing-Yi Zheng

Dissertation Director:

Nada Boustany

Dynamic alteration in organelle morphology is an important indicator of cellular function and many efforts have been made to monitor the subcellular morphology. Optical scatter imaging (OSI), which combines light scattering spectroscopy with microscopic imaging, was developed to non-invasively track real-time changes in particle morphology *in situ*. Using a variable diameter iris as a Fourier spatial filter, the technique consisted of collecting images that encoded the intensity ratio of wide-to-narrow angle scatter (OSIR, optical scatter imaging ratio) at each pixel in the full field of view. For spherical particles, the OSIR was shown to decrease monotonically with diameter. In living cells, we reported this technique is able to detect mitochondrial morphological alterations, which were mediated by the Bcl_{xL} transmembrane domain, but could not be observed by fluorescence or DIC images[1]. However, the initial design was based on Mie theory of scattering by spheres, and hence only adequate for measuring spherical particles. This limits the applicability of OSI to cellular functional studies involving organelles, which are naturally non-spherical. In this project, we aim to enhance the current capability of the existing optical scatter microscope to assess size and shape information for both spherical and non-spherical particles, and eventually apply this technique for monitoring and quantifying subcellular morphology within living cells.

To reach this goal, we developed an improved system, in which the variable diameter iris is replaced with a digital micromirror device and adopted the concept of Gabor filtering to extend our assessment of morphology to the characterization of particle shape and orientation. Using bacteria and polystyrene spheres, we show how this system can be used to assess particle aspect ratio even when imaged at low resolution. We also show the feasibility of detecting alterations in organelle aspect ratio in situ within living cells. This improved OSI system could be further developed to automate morphological quantification and sorting of non-spherical particles in situ. In the future, we plan to pursue the assessment of morphology information for particles of arbitrary shape and seek to correlate gene expression and cell function with subcellular morphology, which may help in disease diagnosis and drug screening.

Acknowledgement

It is a pleasure to thank those who made this thesis possible.

I owe my deepest gratitude to my Ph.D. advisor, Dr. Nada Boustany, for her guidance during my research and study at Rutgers University. With her enthusiasm, her inspiration, and her great efforts to guide me through my research, I build the fundation to be a good scientist. Throughout my thesis-writing period, she provided encouragement, sound advice, good teaching, and lots of good ideas. I would have been lost without her. She has also made available her support in numerous ways other than research. I am grateful to have her as my advisor.

I would like to thank my committees, Dr. Li Cai, Dr. Dimitris Metaxas, Dr. Milind Rajadhyaksha and Dr. Eileen White. They have provided many ideas and advices to improve my research study and thesis writing. This thesis would not have been possible without the help from many people who I know: lab colleagues and collaborative lab colleagues, and from people who I do not know: those I only contact through phone or e-mail. There are so many of people who have helped me in so many ways, it is impossible to list all the names. However, my appreciation is not any less.

I am indebted to my many student colleagues and friends for providing a stimulating and fun environment in which to learn and grow. Please forgive me not listing your names here, I do not wish to let out any of you and do not want to merely list your names here. So many had happened during these years, I am grateful to have so many good friends accompany me through my life at Rutgers and in USA. Thank you for being happier than I am for my happiness, sadder than I am for my sadness and crying for me when I am out of tears. It seems to be digressional as a thesis acknowledgement;

however, all that has happened is irreplaceable and difficult to make a clean break. To all of you who I call friends, who now appear in my mind, the only thing I can say is thank you.

I cannot end without thanking my family, on whose constant encouragement and love I have relied throughout my life. I wish to thank my parents, We-Nan Yu and Su-E Zheng, my sister Pei-Chi and my brother Chih-Hung; they always back me up whenever I need support. To them I dedicate this thesis.

Contents

List of Figures

Chapter 1   Introduction

With the help of modern molecular biology, knowledge of the molecular basis of cell function has significantly increased. Dynamic alteration in the morphology of subcellular organelles is an important indicator of cellular function.   For example, mitochondria become fragmented when cells undergo apoptosis[2, 3] , or when cells are subjected to $Ca2^+$ overload mitochondria will round up[4]. Nevertheless, information about the cell's living, internal function is still lacking because of the absence of a proper tool that can monitor cells and subcellular organelles at the submicron level without disrupting their function.

Conventional optical microscopes have been used in studying biological structure and function at the cellular level. The observation is usually facilitated by staining (visible or fluorescent), since absorption of visible light by cellular structures is relatively weak. Phase contrast and differential interference contrast (DIC) work on the principle of phase shifts and interferometry respectively to gain information about the optical phase of the sample. Nevertheless, the spatial resolution of an optical microscope is limited by the diffraction limit, which is related to the wavelength of illumination used. Because of this limitation, morphology of subcellular organelles at the submicrometer level is difficult to assess. Super-resolution fluorescence methods (ex. PALM[5], STED[6], structured illumination microscopy[7]) provide nanoscale resolution and are facilitated by labeling samples with fluorescent dye. An important biological tool, electron microscopy (EM), can reveal change in subcellular organelle morphology with very high resolution. However, EM only works with nonfunctional cells since it requires fixing samples, dynamic and real-time study using EM is impractical.

1.1   Light scattering

Light scattering is another approach for non-invasive, dynamic study of viable cell function to assess morphology of subcellular particles, whose sizes are close to the optical resolution of microscopes. Light scattering is sensitive to changes in the size and shape of particles with diameter on the order of the wavelength. Different approaches of utilizing scattering features to assess particle morphological information were reported, such as angular-dependent scattering[8-11], wavelength-dependent scattering[12-15], angular and wavelength dependent[16], refractive index structure variation[17, 18], modified Michelson interferometer[19-21], confocal light absorption and scattering spectroscopic microscopy[22], and dynamic light scattering microscopy[23]. These techniques provide overall quantitative size distribution and could be used in the application of probing the preneoplastic colonic microvasculature[24], monitoring neoplastic progression[20], or detecting cancer at an early stage[13]. While these techniques provide good resolution and quantitative results, most of them utilize models based on Mie theory and work better for spherical particle measurement, which is not adequate for biological study since most biological objects, such as organelles, are not spherical. Many efforts were also put on studying non-spherical particles[25-29], however, these methods were mainly for airborne, liquid-borne particles or merely theoretical study.

1.2   Initial optical scatter imaging

In this study, we also use a light scattering approach to study particle morphology, our technique is called optical scatter imaging (OSI). Optical scatter imaging (OSI) was developed to non-invasively track real-time changes in particle morphology with sub-micron resolution without any exogenous labeling, cell fixing, or organelle isolation[4].

This technique was initially set up using an adjustable circular diaphragm with center beam stop in a conjugate Fourier plane to select circular symmetric angles of scattering and measure the size of spheres. For spherical particles, the intensity ratio of wide-to-narrow angle scatter (OSIR, Optical Scatter Image Ratio) was shown to decrease monotonically with diameter and agree with Mie theory. One advantage of the OSI technique is that it provides in situ morphological information as well as quantitative size distributions.

1.2.1 Initial optical scatter imaging system design

The optical scatter imaging technique (Figure 1-1) was described previously in detail[30]. Briefly, the specimens were mounted on the stage of an inverted microscope (Zeiss, Axiovert 200M, Göttingen, Germany), with epi-fluorescence and differential interference contrast imaging capabilities. The condenser was adjusted to central Kohler illumination with numerical aperture (NA) of 0.05 (condenser front aperture closed). A 10nm bandpass interference filter placed in the condenser housing yielded an incident red beam centered at λ=630nm. The images were collected with a 63X oil immersion
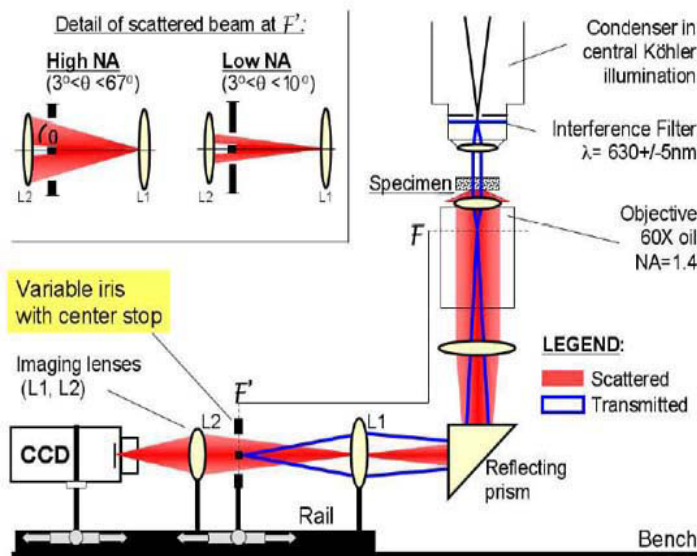
Figure 1-1 Optical Scatter Imaging setup. The scattered light (red beam) is used to image the specimen on the CCD. At F', a beam stop is placed in the center of an iris with variable diameter and blocks the transmitted light (blue line). The iris diameter is set in either a low NA, or a high NA position. (Adapted from Boustany et al., 2001)

objective, NA=1.4, and displayed on a charge coupled device camera (Roper Scientific, Cascade 512B, Tucson, AZ). In a Fourier plane conjugate to the back focal plane of the objective, a beam stop, diameter = 0.7mm, was placed in the center of an iris with variable diameter. The variable iris collected light scattered within a solid angle, and the iris diameter was manually switched between either a low NA ($3°<\theta<10°$), or a high NA ($3°<\theta<67°$) position.

1.2.2 *Optical scatter image acquisition and analysis*

For optical scatter imaging, two sequential dark-field images of each sample were acquired at high and low NA by manually switching the diameter of the variable iris. Dividing the background subtracted high NA images by their corresponding background subtracted low NA images resulted in ratiometric optical scatter images, which directly encoded the high-to-low NA optical scatter image ratio (OSIR) at each pixel in the field of view. The OSIR corresponds to the intensity ratio of wide-to narrow angle forward scatter defined as:

$$OSIR = \frac{\int_{\phi=0°}^{360°}\int_{\theta=3°}^{90°}F(\theta,\phi)\sin\theta d\theta d\phi}{\int_{\phi=0°}^{360°}\int_{\theta=3°}^{11°}F(\theta,\phi)\sin\theta d\theta d\phi} \qquad (1\text{-}1)$$

where $F(\theta,\phi)$ gives the intensity of the light scattered in a given direction defined by the angles θ and ϕ. θ is the angle between the scatter direction and the direction of propagation of the incident light, and ϕ is the azimuthal angle of scatter.

1.3 DMD & application of DMD on microscopy

The light scattering techniques described previously, including optical scatter imaging (OSI), are almost all based on theory or prediction for spherical particles. Hence, the size information/distributions extracted from these methods are actually "equivalent diameters", and the change in shape usually cannot be assessed. Naturally occurring particles, including organelles, are rarely perfectly spherical, and, under some conditions, organelles can change shapes. A method that is able to extract both size and shape information would be more practical. Hence, in this study, we extended our size-sensitive optical scatter imaging (OSI) method to analyze the size and shape of the particles. As is the initial OSI system described above, the new system relies on analyzing the transform of the sample object. The transform is formed in a Fourier conjugate plane of our imaging system and contains the scatter intensity at every scatter angle collected by the microscope's numerical aperture. However, the previous Fourier filter consisted of a circular iris with variable diameter and is insensitive to changes in scattering intensity as a function of the angle ϕ. In the improved system, we used a spatial light modulator (SLM) to generate Fourier filters, which allows us to analyze the scattered light intensity as a function of both θ and ϕ.

In conventional optical microscopes, the control of illumination and collection light is accomplished by combination of lenses and diaphragm, iris, annulus, pin hole, etc., and these components are usually static. To increase spatial resolution, gain flexibility, or get quantitative analysis, many efforts have been directed at improving conventional microscopy. One of many, besides scattering microscopy, is the implementation of spatial light modulators. A SLM is a device that can spatially adjust or modulate the intensity or phase of a light beam and the control of the patterns of illumination and detection is

usually computer programmable. Spatial light modulators can be divided into various classes, including electro-optic, magneto-optic, liquid-crystal (nematic, and ferroelectric), and deformable-mirror SLMs[31, 32]. In this study, we chose a digital micro-mirror device (DMD) for light modulation. The DMD is an array of rotatable aluminum mirrors (1024×768), monolithically fabricated over an address circuit consisting of conventional CMOS SRAM (static random access memory) cells. Each of these SRAM cells corresponds to a micromirror, and the micromirror is rotated as a result of electrostatic attraction between the mirror structure and the underlying memory cell. Each mirror operates in a bistable mode, tilted diagonally +12° or -12° about the hinge attached to the support post[33, 34].

The use of DMD spatial modulators in a microscopy system is mostly in a conjugate image plane as adjustable, dynamic apertures to increase spatial resolution, gain flexibility, or facilitate quantitative analysis. For instance, a DMD can be used to replace the simple circular or annular diaphragms of a conventional microscope to enable digital light microscopy and quantitative analysis[35, 36]. A DMD could be used to modulate light excitation for dynamic cell screening[37]. Also, optical sectioning programmable array microscopes can be incorporated with a DMD to replace the conventional Nipkow disc and achieve a multiple-aperture confocal imaging system[38, 39]. A high-speed addressable confocal microscope was built by combing an acousto-optic deflector with a DMD for point illumination and point detection[40]. A fiber-optic confocal microscopy used a DMD to sequentially illuminate fibers to improve the optical-sectioning ability and also allows endoscopic application[41]. Rector and colleagues used a DMD as a "virtual pinhole" and digitally reconstructed confocal images for microscopic or endoscopic application[42]. A DMD can also be used for digital fringe projection and phase-shift technique in a

microscopic 3-D shape measurement system[43] or controlled optical sectioning in a fullfield fluorescence microscope[44] to allow free control of optical sectioning strength. Modulated imaging utilizing projection of sinusoidal illumination patterns using a DMD was also used for quantification and mapping of optical properties in turbid tissue[45]. In contrast with theses studies, we use our DMD in a conjugate Fourier plane. When activated by a programmable actuator, the mirrors can be tilted in tens of microseconds to deflect the incoming light towards or away from the collection optics. The micro-mirror array therefore acts like an array of shutters, which can be used to pass or block the light scattered at any desired combination of scattering angles within the numerical aperture of the microscope system. This can in turn be used to characterize particle shape by analyzing the scattering pattern in two dimensions.

1.4   Gabor filtering

In order to characterize morphology of non-spherical particle, we need filters that are sensitive to changes in scattering intensity along azimuthal angle ϕ. For this purpose, we adopted the concept of Gabor filtering. The Gabor filters are band-pass filters with tunable center frequency, orientation and bandwidth. Gabor filters could be tuned to be sensitive to specific textures and insensitive to all others. By filtering the image with multiple band-pass filters tuned to the dominant frequency and orientation component of the textures, it is possible to locate each texture[46]. In addition, Gabor filters achieve an optimal joint resolution and localization properties in both frequency and spatial domain[47]. Gabor filters have been used in many applications, such as texture segmentation, target detection, fractal dimension management, document analysis, edge detection, retina identification, image coding and image representation[48].

A Gabor filter is a linear filter with a sinusoidal carrier of particular frequency and orientation, modulated by a Gaussian envelope. A complex Gabor function in space domain can be written as:

$$h(x, y) = s(x, y)g(x, y)$$

(1-2)

where $s(x, y)$ is a complex sinusoid, and $g(x, y)$ is a 2-D Gaussian-shaped function. The Gabor filter's impulse response in Fourier domain is:

$$H(u, \upsilon) = (2\pi\sigma_x\sigma_y) \cdot e^{-2\pi^2\left[(u-U)^2\sigma_x^2 + (\upsilon-V)^2\sigma_y^2\right]}$$

(1-3)

The parameters σ_x, σ_y are the standard deviation of the Gaussian envelope along x and y direction and determine the filter band width. The spatial center frequency of the Gabor function is defined by (U, V). Thus the Gabor function can be thought of as a Gaussian function shifted in frequency to position (U, V), at a distance of $F = \sqrt{U^2 + V^2}$ from the origin and at an orientation of $\phi = \tan^{-1}(V/U)$.

For isometric Gaussians, $\sigma_x = \sigma_y = \sigma$

$$H(u, \upsilon) = (2\pi\sigma^2) \cdot e^{-2\pi^2\left[(u-U)^2\sigma^2 + (\upsilon-V)^2\sigma^2\right]}$$

(1-4)

1.5   Thesis outline

In chapter 2, we will first demonstrate how the optical scatter imaging technique can be used to monitor cell function and cell response to specific genetic alterations by using initial OSI system. Since the initial OSI system is not adequate for measuring non-spherical particles, we introduced an improved DMD-based OSI system. However, the use of DMD in a conjugate Fourier plane results in significant chromatic and geometric

aberrations. In chapter 3, we will introduce the design of new DMD-based OSI system and show how the imaging artifacts may be overcome. With this new DMD-based OSI system established, we validated the new system with the measurement of OSIR, and compared the measurement with measurement obtained with the initial system and theory prediction. These validations will be illustrated in chapter 4. In chapter 5, we adopted the concept of Gabor filtering and generated optical Gabor-like size dependent and orientation dependent filter banks. We will demonstrate the feasibility of optical Gabor-like filtering on discriminating particles based on their size and roundness and demonstrate the feasibility of applying the new filtering scheme on living cells.

Chapter 2 The C-terminal Transmemberane Domain of Bcl-xL Mediates Changes in Mitochondrial Morphology

- This work was published in " J.Y. Zheng, Y.C. Tsai, P. Kadimcherla, R. Zhang, J. Shi, G.A. Oyler, N.N. Boustany, 'The C-terminal transmembrane domain of Bcl-x_L mediates changes in mitochondrial morphology', Biophysical J., 94 (1): 286-297, 2008".

2.1 Introduction

In a previous study using the optical scattering imaging (OSI) technique, it was reported that overexpression of mitochondria-bound Bcl-x_L can modulate changes in light scattering by measuring light scattering directly within subcellular compartments of living cultured cells[49]. This alteration in scattering property suggests morphological change of mitochondria, since Bcl-x_L is exclusively bound to mitochondria in our cell model and light scattering of a cell is mainly contributed by mitochondria[30, 50, 51]. By studying the effect of Bcl-x_L on modulating light scattering of living cells, we may reveal how the change in optical scattering imaging ratio or mitochondrial morphology relates to the anti-apoptotic ability of Bcl-x_L.

Proteins of the Bcl-2 family are important regulators of apoptosis, a highly controlled form of cell death fundamental to tissue development and homeostasis. Bcl-2 family members share Bcl-2 homology (BH) domains. The family includes multi-domain pro-apoptotic proteins (e.g. Bax, Bak) containing BH1-BH3, multi-domain anti-apoptotic proteins (e.g. Bcl-2, Bcl-x_L) containing all four BH1-BH4 domains, and "BH3-only" pro-apoptotic proteins (e.g. Bid, Bad, Bim, Noxa) containing only the BH3 domain. Multi-domain Bcl-2 family proteins also possess a transmembrane C-terminal region (TM domain), which can localize within organellar membranes including the outer membrane of the mitochondria. Bcl-2 family proteins can promote or inhibit apoptosis

by regulating the release of pro-apoptotic factors, such as cytochrome c, SMAC/DIABLO and OMI/HtrA2, from the mitochondria. Once released into the cytoplasm, these factors activate caspases resulting in nuclear fragmentation and orderly dismantling of the cell[52].

The mechanisms by which structural changes in the mitochondrial matrix and membranes may affect subsequent function have long been under study. Electron microscopy studies of mitochondria have shown that alterations in mitochondrial morphology are associated with different mitochondrial metabolic states[53-58]. More recent electron tomography studies of mitochondria strongly suggest that specific compartmentation of the mitochondrial matrix may help localize respiration, and in the case of apoptosis help to free cytochrome c, and facilitate its release from the intermembrane space[59-63]. As such, tracking changes in mitochondrial structure can provide a way to monitor mitochondrial function, and may provide important clues regarding the function of Bcl-2 family proteins in apoptosis at the level of the mitochondria.

Changes in the morphology of the mitochondrial matrix involve structural variation on the order of ten to several hundred nanometers, and are typically assessed by electron microscopy[64]. Electron microscopy is not easily amenable to study dynamic changes in mitochondrial structure within living cells or intact tissue. Thus, studies of isolated mitochondria[55, 58], and of mitochondria within living cells[11, 30, 49, 65], or in whole tissues[66, 67], have relied on light scattering as a method to probe mitochondrial morphology without sample fixation or freezing. Light scattering does not provide the level of morphological detail achieved by electron microscopy. However, the technique can be invaluable for continuous monitoring of nanoscale morphological activity, and ultimately discovering time points at which structural changes occur and can be further

evaluated. In this chapter, we will also demonstrate how the OSI technique could be used to monitor cell function and cell response to specific genetic alterations. Using this approach, we have found that the light scattering properties of apoptotic rat undifferentiated mesencephalic CSM 14.1 cells are altered after expression of Bcl-x_L fused to yellow fluorescent protein (YFP-Bcl-x_L)[49]. Utilizing the expression of a Bcl-x_L mutant lacking the C-terminal TM domain (YFP-Bcl-x_L-ΔTM), we further show in this study that the observed change in light scattering requires mitochondrial localization, and is accompanied by expansion of the mitochondrial matrix, as observed by electron microscopy. In addition we also show that expression of the Bcl-x_L C-terminal TM domain fused to YFP (YFP-TM), and lacking the rest of the Bcl-x_L protein, is by itself sufficient to alter mitochondrial morphology and confer a limited level of resistance to staurosporine induced apoptosis.

2.2 Methods

2.2.1 Gene constructs

Mouse Bcl-x_L was previously cloned into the pEYFP-C1 vector (Clontech, BD Biosciences, Palo Alto, CA) using the BglII restriction site to yield a plasmid encoding an enhanced yellow fluorescent protein (YFP) fused to Bcl-x_L [49]. Bcl-x_L-ΔTM, consisting of eYFP fused to Bcl-x_L, from which the last 63 bases were truncated, was generated by polymerase chain reaction (PCR) with Bcl-x_L as template and the upper primer, 5'-GGACTCAGATCTATGTCTCAGAGCAACCGGGAG-3', and lower primer 5'-CTGCAGAATTCTCAGCGGTTGAAGCGTTCCTGGCC-3'. Bcl-x_L-ΔTM was subcloned into the eYFP vector at the BglII/EcoRI sites. The sequence of the final product matched Bcl-x_L in the GenBank data base. Compared to the reference sequence,

and in addition to the C-terminal truncation, our sequence contained a C209G mutation, leading to a glycine (GGC) instead of an alanine (GCG) at amino acid # 70 in the Bcl-x_L protein. The same mutation was reported in one other Bcl-x_L Beta sequence listed in the public database.

YFP-TM, consisting of YFP fused to the last 63 bases of the Bcl-x_L gene, was generated by PCR with pEYP-C1 as template and the upper primer, 5'-AGATCCGCTAGCGCTACCGGTCGCCACCATGGTGAGC-3' and lower primer 5'-CGACTGCAGAATTCA<u>TTTCCGACTGAAGAGTGAGCCCAGCAGAACCACGCCG</u> <u>GCCACAGTCATGCCCGTCAGGAACCA</u>AGATCTGGATCC-3' (TM sequence underlined). YFP-TM was subcloned into the pECFP-C1 vector (Clontech, BD Biosciences, Palo-Alto CA) replacing the CFP sequence between the NheI and EcoR1 sites. The sequence of the final amplified and purified product after cloning into the pCFP-C1 vector confirmed the presence of 5'-<u>eYFP</u>-TCCGGACTCAGATCT-TM-TGA. The sequence between eYFP and TM is the same as the beginning of the multiple cloning site in the pEYFP-C1 vector.

2.2.2   Generation of stable cell-lines

Stable expression of YFP, and YFP-Bcl-x_L in inducible, rat mesencephalic CSM14.1 cells was described previously[49]. In this study CSM 14.1 cells were transfected at 80%-90% confluence with an empty plasmid encoding hygromycin resistance and either YFP-Bcl-x_L-ΔTM or YFP-TM (1:10 molar ratio, hygromycin plasmid: fluorescent protein plasmid) using lipofectamine 2000 in OptiMEM medium (Invitrogen, Rockville MD). Immortalized baby mouse kidney (iBMK) cells were transfected at 80%-90% confluence with YFP-Bcl-x_L, YFP-Bcl-x_L-ΔTM, YFP-TM or YFP. Twenty four hours

post-transfection, the cells were subcultured at 1000 cells/78.5 cm^2 (10cm-dish) in growth medium supplemented with 400μg/ml hygromycin B (Invitrogen, Rockville MD) for CSM 14.1 selection, or 1 mg/ml geneticin sulfate (G418, Invitrogen Rockville MD) for iBMK selection. Isolated foci with yellow fluorescence were picked, serially diluted and replated in 96-well plates to obtain clonal cell-lines. In CSM cells, expression of YFP constructs was confirmed by immunoblots and fluorescence microscopy; in iBMK cells, by fluorescence microscopy.

2.2.3   Cell culture

CSM 14.1 cell lines were maintained in Dulbecco's modified Eagle's medium (DMEM,) supplemented with 10% (V:V) fetal bovine serum (FBS), 1% (V:V, ~0.1mM) non-essential amino acid, 100 Units/ml penicillin, 100μg/ml streptomycin, and 1mg/ml geneticin sulfate (G418). DMEM, FBS, non-essential amino acids, penicillin and streptomycin were from Invitrogen, Rockville MD. CSM 14.1 cells were kept undifferentiated in culture at 32°C in a 5% CO_2 in air atmosphere. Stable CSM 14.1 cell-lines transfected in this study with YFP-Bcl-xL-ΔTM and YFP-TM were maintained in the growth medium described above supplemented with 400μg/ml hygromycin B. iBMK cells were maintained at 38°C in a 5% CO_2 in air atmosphere in DMEM supplemented with 10% (V:V) FBS (Gemini Bio-Products, West Sacramento, CA), and 100 Units/ml penicillin, 100μg/ml streptomycin. For microscopy, cells were cultured on glass cover slips, which only in the case of CSM 14.1 cells, were coated with poly-D lysine (molecular weight >300,000 kD, Sigma Chemical Co., St Louis, MO).

2.2.4 Immunoblots

CSM 14.1 cells were washed with phosphate buffered saline (PBS), and lysed in SDS buffer (10mM Hepes pH7.4, 38mM NaCl, 2% sodium dodecyl sulfate) supplemented with 1 µg/ml leupeptin, 1 µg/ml aprotinin, and 0.2mM phenylmethylsulfonyl fluoride (PMSF). Leupeptin, aptotinin and PMSF were from Sigma Chemical Co, St. Louis. MO. The lysates' protein content was determined by a colorimetric bicinchoninic acid analysis (BCA; Pierce, Rockford, IL). For each cell variant, 30µg of cell lysate protein were resolved by 12% standard sodium dodecyl sulfate-polyacrylamide gel electrophoresis (SDS-PAGE). After transfer to a polyvinylidene difluoride (PVDF) membrane by semidry electroblotter (Bio-Rad, Hercules, CA), blots were blocked with 5% milk with 0.05% Tween-20 in TBS buffer (20mM Tris, 500mM NaCl, pH 7.5) followed by incubation with mouse anti-GFP antibody (0.2µg/ml, Santa Cruz Biotechnology, Santa Cruz, CA, GFP-B-2, Cat. # SC-9996), and developed with enhanced chemiluminescence (ECL) reagents (Amersham, Piscataway, NJ).

2.2.5 Fluorescence microscopy

YFP fluorescence was imaged using a YFP filter cube (Carl Zeiss Filter # 46): excitation: 500 ± 20 nm bandpass; emission: 515nm dichroic mirror followed by a 535 ± 30 nm bandpass filter. Mitochondria were also specifically imaged by immunofluorescence of the complex V unit. For this, cells were grown on glass coverslips to ~70% confluence, washed with phosphate buffered saline (PBS), and fixed for 1 min in a 1:1 V:V, methanol:acetone solution, which had been stored at -20°C. After three washes in PBS, samples were incubated at 37°C for 1 hour in blocking buffer (2% fetal bovine serum in PBS) followed by 1 hour in blocking buffer supplemented with 2

μg/ml anti-OxPhos complex V subunit alpha mouse IgG2b (A21350, Invitrogen Rockville MD). The samples were washed in PBS and further incubated at 37°C for 1 hour in blocking buffer supplemented with 1.5 μg/ml Tetramethylrhodamine goat anti-mouse IgG (T2762, Invitrogen, Rockville, MD). Coverslips were finally washed three times with PBS and mounted on microscope slides with SlowFade® (S2828; Invitrogen, Rockville, MD). For the YFP CSM 14.1 cell variant, fixation and immunofluorescnece labeling were done at room temperature, immediately after imaging YFP fluorescence. Rhodamine fluorescence was detected with a standard rhodamine filter cube (Carl Zeiss filter #20): excitation: 546 ± 12 nm bandpass; emission: 560 nm dichroic mirror followed by a 575-640 nm band pass filter. For the same image acquisition time in each channel, the equivalent of 3.36% of rhodamine signal measured in the rhodamine channel spilled over into the YFP channel, while the equivalent of 3.44% of YFP signal measured in the YFP channel spilled over into the rhodamine channel. Fluorescence images of samples double labeled with YFP and anti-Complex-V/rhodamine were corrected for this spillover.

2.2.6 Optical scatter image acquisition and analysis

Each cover slip with attached live cells was mounted by means of a steel plate onto the stage of the inverted microscope. Just before mounting onto the microscope's stage, the DMEM growth medium was replaced with Leibovitz L15 medium (Invitrogen, Rockville, MD) supplemented with 10% fetal bovine serum, 100 Units/ml penicillin, and 100 g/ml streptomycin. The cells were monitored by DIC, fluorescence, and optical scatter microscopy at room temperature and room air. For optical scatter imaging, two sequential dark-field images of each cell sample were acquired at high and low NA by

manually switching the diameter of the variable iris. A sample of L15 growth medium was used to collect background scatter signal due to the microscope optics. Dividing the background subtracted high NA images by their corresponding background subtracted low NA images resulted in ratiometric optical scatter images, which directly encode the high-to-low NA optical scatter image ratio (OSIR) at each pixel in the field of view.

Optical scatter images were acquired in IPlab (BD Biosciences Bioimaging, Rockville, MD) and processed in Matlab (The Math Works, Natick, MA). In each experiment, a segment was manually defined around every cell in the DIC images. These segments were overlaid onto the optical scatter images such that data analysis was limited to regions containing a cell. Only positively fluorescent cells were analyzed in the transfected cell variants. In addition, we further segmented the regions in the YFP TM cells that corresponded to bright and punctate fluorescent mitochondria to measure the OSIR at these specific locations. Two criteria were used to locate these small bright regions in the YFP-TM fluorescence images. First, each of these regions was centered on a local maximum of the intensity profile. These local maxima were detected using a 2-D order-statistic filter (50). Second, local maxima with intensity above background were selected. Since the YFP-TM fluorescence images did not have uniform exposure, setting a single threshold was not possible. Instead, a Laplacian filter (51) was used to measure the second spatial derivative in the image, and only retrieve peaks with large intensity changes. At completion of the algorithm, we verified that the detected local peaks corresponded to the punctate mitochondria in the fluorescence images.

2.2.7 Cell death assay

Cell death resistance was assayed by measuring the percentage of dead cells in response to staurosporine (STS) treatment. Cells were cultured in 12-well plates, and

treated with 1μM STS (Sigma Chemical Co. St. Louis MO) at 90% confluence. After 24 hours, 40μM propidium iodide (Invitrogen, Rockville MD) was added to the incubated cultures for 15 minutes. The cells were collected from the plates by pipeting and trituration. Microscopic observation of the plates insured that all cells were collected by this process. The cell suspension was concentrated to approximately 5×10^5 cells/ml by centrifugation and partial removal of the supernatant. The number of cells with positive propidium iodide fluorescence in the final cell suspension was counted in a hemacytometer, and was taken to represent dead cells, which had lost membrane integrity. Propidium iodide fluorescence was visualized with the rhodamine filter cube described above (Zeiss Filter # 20).

2.2.8 Electron microscopy and mitochondrial counting

CSM 14.1 cells were grown to about 90% confluence in Sonic Seal Slide wells (Electron Microscopy Sciences, Hatfield, PA, # 70365-42). The cells were washed (2x 1 min.) in PBS, and incubated for two hours in Karnovsky's modified fixative (2.5% gluteraldehyde, 4% paraformaldehyde, 0.1M sodium cacodylate, 8mM calcium chloride, pH= 7.4; Electron Microscopy Sciences, Hatfield, PA). After two hours, the fixative was removed and replaced with another fresh aliquot of the same. Directly following this fixation, or after storage overnight at 4^oC, the cells were washed (2x 10 min.) in cacodylate buffer (0.1M sodium cacodylate, pH= 7.4), post-fixed for one hour at room temperature in cacodylate buffer supplemented with 1% osmium tetroxide, dehydrated in a graded series of acetone, and embedded in Epon-Spurr resin. Sections 90nm thin were cut on a Leica EM UC6 ultramicrotome (Leica Microsystems, Bannockburn, IL). Sectioned grids were stained with a saturated solution of uranyl acetate and lead citrate,

and observed at 80 kV on a JEOL 1200EX transmission electron microscope (JEOL, West Chester, PA).

The electron micrographs revealed two types of mitochondria: 1) mitochondria with a condensed matrix, which had visible cristae under 40,000 X magnification, and 2) mitochondria with an "expanded" matrix, in which the intracristal spaces were greatly reduced and the cristae were not visible under up to 50,000X magnification. The two types of mitochondria were counted at 40,000 X in several arbitrary fields. The number of fields, and therefore the total area spanned, in each of the cell variants was the same. Approximately 150 mitochondria were counted per sample, and the count generally spanned between 15 – 20 cells. Mitochondria with a matrix, which seemed partially expanded and partially condensed, were taken as having a condensed matrix.

(The Electron micrographs study was done by Pradeep Kadimcherla, an undergraduate senior at the time.)

2.3 Results

2.3.1 Expression of protein constructs in CSM 14.1 cells

To investigate the effect of Bcl-x_L localization on mitochondrial morphology, we generated four stable CSM 14.1 cell lines expressing YFP, YFP-Bcl-x_L, YFP-Bcl-ΔTM, or YFP-TM (Figure 2-1A). YFP-Bcl-x_L-ΔTM, consisted of YFP fused to Bcl-x_L lacking the last 21 amino acids at its C-terminal; YFP-TM of YFP fused to the last 21 amino acids Bcl-x_L. These 21 amino acids, WFLTGMTVAGVVLLGSLFSRK, constitute the C-terminal hydrophobic TM domain of Bcl-x_L[68]. YFP expression and subcellular localization were confirmed by immunoblots against YFP, and fluorescence microscopy, respectively (Figure 2-1B and C). Cell expressing YFP-Bcl-x_L and YFP-Bcl-x_L-ΔTM exhibited a band around 50 kD corresponding to expression of the fusion construct YFP-

Bcl-x$_L$. Cells transfected only with YFP or YFP-TM, and lacking Bcl-x$_L$, exhibited a band between 29 and 37 kD corresponding to YFP expression. Cells expressing YFP-Bcl-x$_L$ exhibited a filamentous yellow fluorescence distribution, which coincided with the distribution of the mitochondria assessed by immunofluorescence labeling of the ATP synthase (anti-OxPhos Complex V). When the TM domain of Bcl-x$_L$ was deleted, the
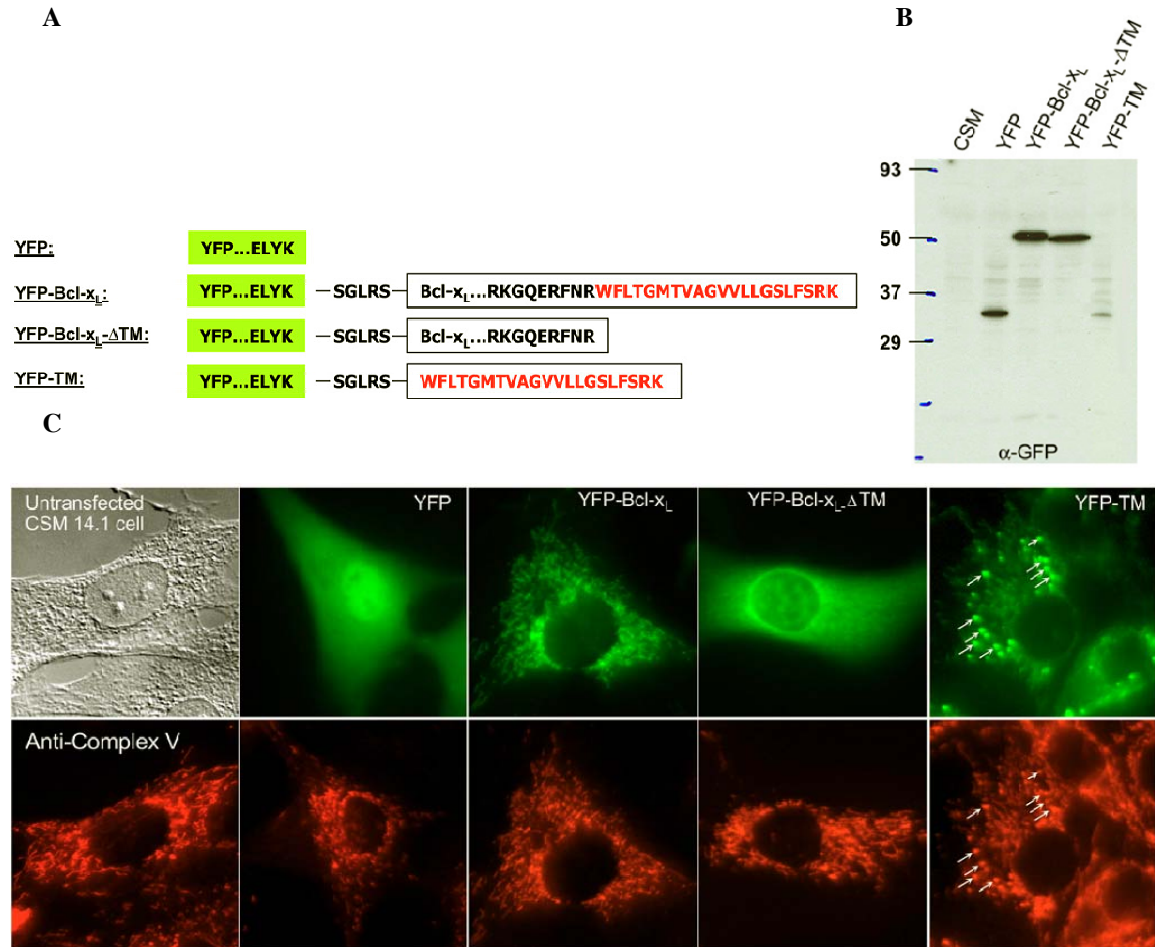
Figure 2-1 YFP constructs, YFP expression, and YFP localization in CSM 14.1 cell lines. (A) Bcl-x$_L$, Bcl-x$_L$-ΔTM, which lacks the last 21 amino acids of wild-type Bcl-x$_L$, or TM, which consists of the last 21 amino acids of Bcl-x$_L$, was fused to YFP. (B) YFP expression in CSM 14.1 cells was confirmed by Western blotting. As expected, a band between 29 and 37 kDa was found for cells transfected with YFP or YFP-TM. A band just above 50 kDa corresponds to the presence of YFP-Bcl-x$_L$ and YFP-Bcl-x$_L$-ΔTM (Bcl-x$_L$ is ;26 kDa). (C) Differential interference contrast (upper left panel) and fluorescent images of representative cells transfected with YFP, YFP-Bcl-x$_L$, YFP-Bcl-x$_L$-ΔTM, and YFP-TM. The distribution of YFP-Bcl-x$_L$ and YFP-TM (third and last panel pairs) coincides with the distribution of mitochondria labeled with anti-OxPhos Complex V antibody. Very bright and punctate mitochondria were also found in ~50% of the YFP-TM transfected cells (arrows in last panel pair). YFP distribution is diffuse in cells transfected with YFP and YFP-Bcl-x$_L$-ΔTM.

YFP-Bcl-x_L-ΔTM protein was diffusely distributed in the cells. In contrast, YFP fused to

the TM domain (YFP-TM) specifically targeted the mitochondria. In more than 50% of

the YFP-TM cells, we also found very round and bright punctate mitochondria (arrows in

last panel pair of Figure 2-1C). Using fluorescence images, which were corrected for

spillover between the YFP and Complex V rhodamine fluorescence channels, we

normalized the YFP signal per pixel to the Complex V signal per pixel. Within a given

cell, the normalized YFP-TM signal in these bright punctate mitochondria was typically
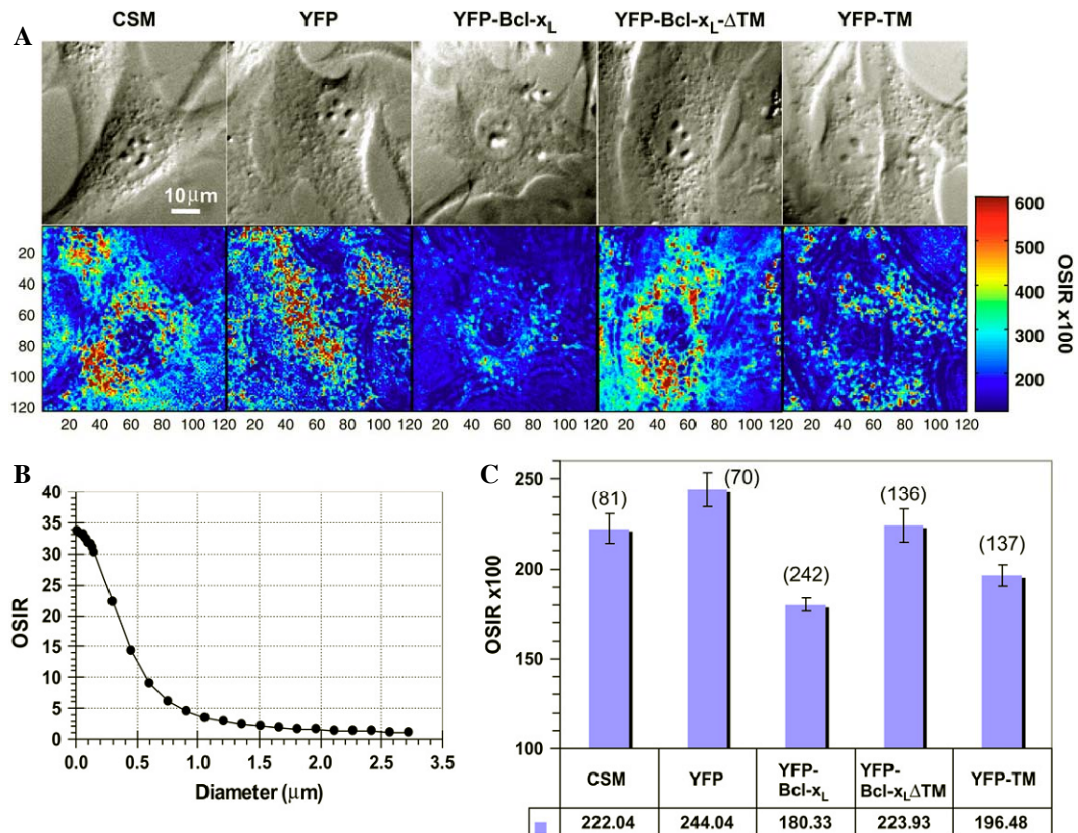
Figure 2-2 Optical scatter images (OSI) and optical scatter image ratio (OSIR) values in the CSM 14.1 cell variants. (A) Differential interference contrast (DIC, top panels), and OSI images of untransfected (CSM, leftmost panels) and transfected CSM 14.1 cells. OSI pixel values (color bar) encode local measurements of OSIR, which can be theoretically described by Eq. 1. Note that the image pixels encode OSIR×100. (B) Mie theory prediction of the average OSIR per pixel expected from images of homogeneous suspensions of spheres with a given diameter. For spheres, the OSIR is expected to decrease monotonically with increasing sphere diameter D, for 0.015 μm< D< 2.75 μm. (C) Mean OSIR per cell for each of the five CSM 14.1 cell variants. Error bars represent the 95% confidence interval of the mean, and the number in parenthesis is the number of cells tested.

around four times higher than the YFP-TM signal in their long and filamentous counterparts.

2.3.2 Effect of Bcl-x$_L$ and Bcl-x$_L$ mutants on light scattering by CSM 14.1 cells

Representative optical scatter images are shown alongside DIC images for the CSM cell variants (Figure 2-2A). In the optical scatter images, the pixels directly encode the local value of the OSIR, which corresponds to the intensity ratio of wide-to-narrow angle optical scatter (Equ. 1). For spheres with diameter between 0.015 μm and 2.72μm, and with refractive index ratio m= 1.04, the calculated OSIR, based on Mie theory, decreases non-linearly and monotonically from 33.65 to 1.15 as a function of diameter (Figure 2-2B). Thus, the OSIR can be utilized as a measure of subcellular morphological changes caused by expression of Bcl-x$_L$ or its mutants. Cell by cell analysis showed that the mean OSIR per cell was decreased from 2.22 for parental cells to 1.80 for YFP-Bcl-x$_L$, and 1.97 for YFP-TM cells. The difference between the OSIR values of YFP-Bcl-x$_L$ and parental cells, and YFP-TM and parental cells were significant with $p<10^{-14}$ by Student t-test. In contrast, the mean OSIR per cell for Bcl-x$_L$-ΔTM was 2.23, and similar (p= 0.78) to that of the parental cells (Figure 2-2C), while the mean OSIR value of the YFP cells, 2.44, was 10% higher than that of the untransfected cells ($p< 10^{-3}$).

OSIR was binned into 326 elements with 0.1 intervals spanning 1.15 to 33.65. Pixel histograms were normalized to the number of pixels with OSIR= 1.15, and are displayed in the OSIR range 1.15-12.00, which included more than 95% of the pixels (Figure 2-3A). The un-normalized histogram means, which represent the ensemble of pixel values collected within a given variant, largely corroborate the single cell analysis. In particular, the mean pixel value was 18% lower for YFP-Bcl-x$_L$ and 12% lower for YFP-

TM compared with untransfected parental cells. The mean pixel value of the Bcl-x$_L$-ΔTM cells was similar to that of the parental cells (Figure 2-3B). However, the increase in the mean pixel value for YFP was only 1.3% by this analysis. In addition, the YFP-TM histogram had a larger relative contribution from pixels with values above 200 compared with the YFP-Bcl-x$_L$. To find out whether this difference in the YFP-TM histogram could be accounted for by the presence of the bright and punctate mitochondria found by fluorescence (Figure 2-1C), we specifically segmented out these bright regions in the YFP-TM fluorescence images and obtained a pixel histogram of the OSIR values falling specifically on these image segments. This histogram (yellow line in Figure 2-3A) did not coincide with the YFP-TM histogram, and the pixel values associated with the bright and punctate mitochondria had an even larger proportion of pixels with values above 200. The segments associated with the bright and round mitochondria represented

A   B
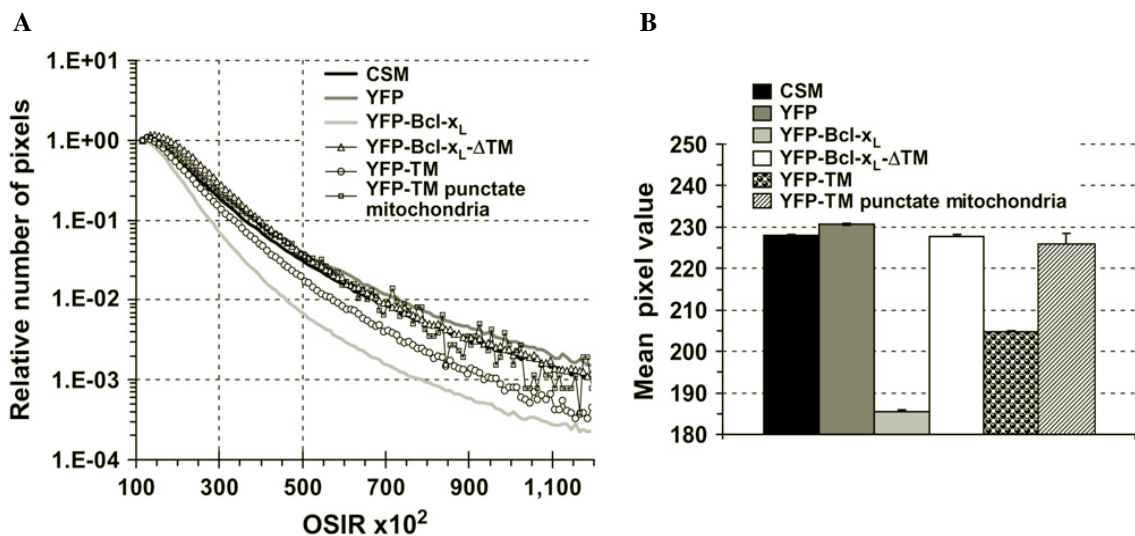
Figure 2-3 Pixel analysis of OSI images. (A) Pixel histograms normalized to the number of pixels with OSIR ¼ 1.15 for the untransfected CSM 14.1 cells (black) and transfected CSM 14.1 variants (dark gray, YFP; light gray, YFPBcl-x$_L$; triangles, YFP-Bcl-x$_L$-DTM; circles, YFP-TM). Each histogram includes pixels from all the segmented cell images considered within a given variant.
The line with connected small squares corresponds to the pixel histogram of the bright and punctate mitochondria, which were found by fluorescence in YFP-TM cells (see also last panel pair in Fig. 1 C) and segmented via a local intensity peak detection algorithm. (B) Mean of the unnormalized pixel histograms for each of the CSM 14.1 cell variants, and punctate mitochondria found in the YFP-TM cells. The error bar corresponds to the 95% confidence interval of the histogram mean.

only ~2%, of all the pixels analyzed in the YFP-TM case. Thus, their histogram could not fully account for the shift in the YFP-TM histogram above the YFP-Bcl-x_L histogram.
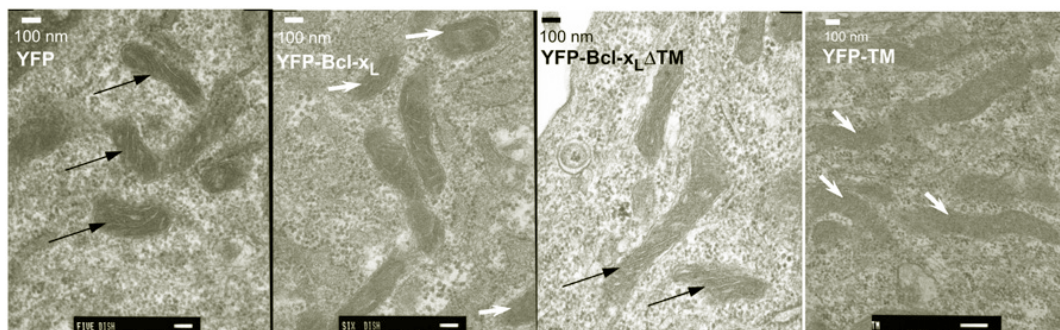
Figure 2-4 Representative electron micrographs of mitochondria with a condensed matrix (black arrows) or an expanded matrix (white arrows) found in the transfected CSM14.1 cell variants. Mitochondria with a condensed matrix were ones in which at least one crista could be discerned, while mitochondria with an expanded matrix had very reduced intracristal spaces, such that no cristae could be discerned under up to 50,000X magnification.

2.3.3 Effect of Bcl-x_L and Bcl-x_L mutants on mitochondrial morphology

Alterations in subcellular morphology underlie changes in light scattering. Thus to corroborate the scattering data, and better characterize the morphological changes at hand, we used electron microscopy to image the cell variants. Since our YFP constructs were designed based on their mitochondrial targeting properties, we specifically looked for alterations in mitochondrial morphology.
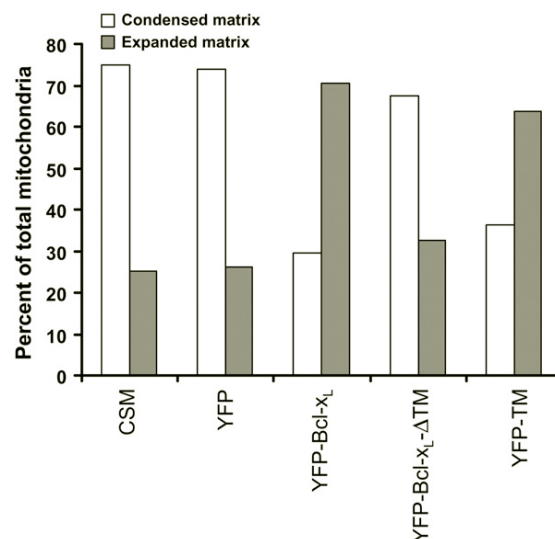
Figure 2-5 Proportion of observed mitochondria with expanded or condensed matrix within each cell variant.

We identified two types of mitochondria in the CSM 14.1 cell variants: 1) mitochondria with a condensed matrix, in which the cristae are clearly visible at 40,000X (Figure 2-4, black arrows), 2) mitochondria with an "expanded" matrix, in which the intracristal spaces were so reduced, the cristae could not be discerned under 40,000X or 50,000X (Figure 2-4, white arrows). By counting the number of each type of mitochondria in the cell variants considered, we found that cells expressing YFP-Bcl-x_L or YFP-TM have a significantly higher proportion of mitochondria with expanded matrix (~70%), in contrast with untransfected cells, cells expressing YFP, or cells expressing YFP-Bcl-x_L-ΔTM, in which the proportion of mitochondria with condensed matrix was significantly higher (Figure 2-5).

In addition, we found that unlike all other variants, a large number of YFP-TM cells showed evidence of autophagy (Figure 2-6). In particular, out of approximately 50 cells, 80% of the YFP-TM cells had more than 20 autophagocytic vesicles, while less than 15% of the cells had more than 20 autophagic vesicles in the other variants. Moreover, all YFP-TM cells observed under electron microscopy had a least one such vesicle, while many cells in the other variants had none.
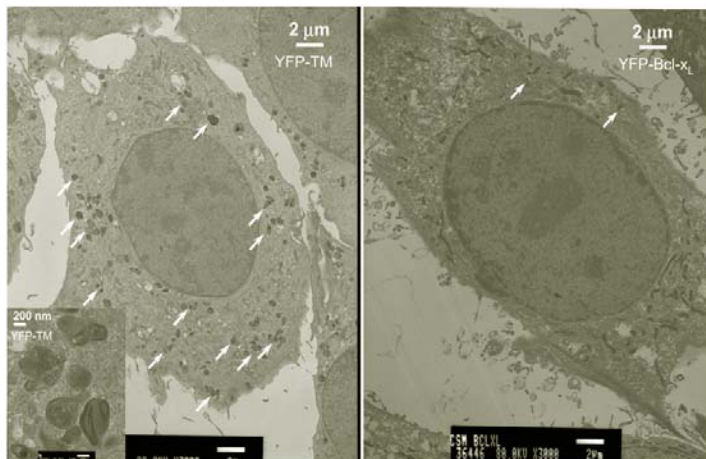
Figure 2-6 Low magnification electron micrographs showing a large number of autophagocytic vesicles (arrows) in a representative YFP-TM cell, and comparison with a typical YFP-Bcl-xL-expressing cell. (Inset) High magnification view of a few autophagocytic vesicles in a YFP-TM cell.

2.3.4 Effect of Bcl-x$_L$ and Bcl-x$_L$ mutants on apoptosis resistance

To study the potential relationship between mitochondrial morphology alterations and apoptosis resistance, we tested the effect of Bcl-x$_L$ and Bcl-x$_L$ mutants on cell death in response to staurosporine. Both CSM 14.1 and iBMK cells, which were tested in this part of the study, were previously shown to undergo apoptosis in response to staurosporine[49, 69]. After 24 hours of treatment with 1µM staurosporine, the percentage of dead cells was 31.7 ± 10.3% and 42.1 ± 6.3% for parental CSM 14.1 cells, and cells expressing YFP, respectively (Figure 2-7). As expected, CSM 14.1 cells expressing Bcl-x$_L$ were resistant to apoptosis and had only 2.3 ± 0.7% dead cells under the same treatment. YFP-Bcl-x$_L$-ΔTM induced as much cell death resistance as Bcl-x$_L$, 7.2 ± 5% dead cells. Surprisingly, in response to 24 hrs of STS treatment, CSM 14.1 cells also exhibited a moderate level of cell death resistance after YFP-TM transfection, 16.3% ± 5 dead cells, compared to 42.1 ± 6.3 dead cells for YFP. To test the reproducibility of these data in another cell line, we repeated our cell death resistance experiments in iBMK cells stably transfected with the same YFP constructs. The iBMK experiments corroborated the CSM 14.1 results. In both cases, Bcl-x$_L$-ΔTM conferred a strong level
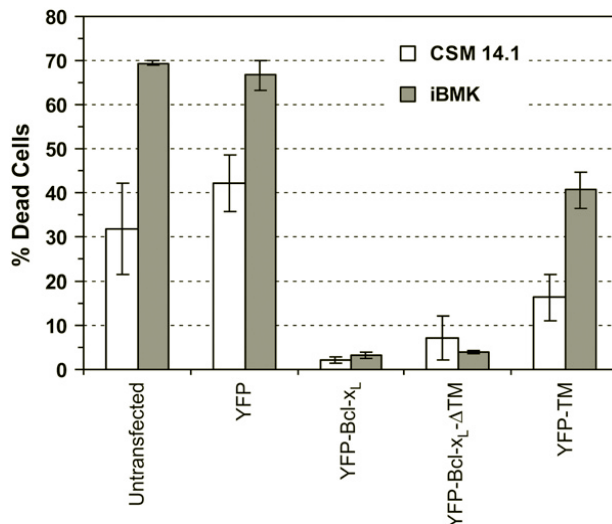
Figure 2-7 Percentage of dead CSM 14.1 and iBMK cells assessed by propidium iodide exclusion after 24 h of treatment with 1 µM staurosporine. Both cell types were stably transfected with YFP, YFP-Bcl-x$_L$, YFP-Bclx$_L$-ΔTM, or YFP-TM. Mean ± SD of at least three cell plates.

of resistance similar to that of Bcl-x$_L$, and YFP-TM provided a moderate level of resistance.

2.4   **Discussion**

We had previously observed that expression of YFP-Bcl-x$_L$ is specifically localized on the mitochondria, and alters angular light scattering by CSM 14.1 cells[49].   By measuring the intensity ratio of wide-to-narrow angle scatter, OSIR, we had found a decrease in OSIR in response to YFP-Bcl-x$_L$ expression. In the present study, we report that this optical scatter change correlates with a high incidence of mitochondria with an expanded matrix, in which the intracristal spaces were so reduced, they seemed absent as observed electron microscopy at high magnification.   About 70% of mitochondria exhibited an expanded matrix in cells expressing YFP-Bcl-x$_L$, compared with only 30% of mitochondria with an expanded matrix in parental cells, or cells expressing only YFP. The relative OSIR values reported in this manuscript reproduce our earlier data for untransfected, YFP and YFP-Bcl-x$_L$ CSM 14.1 cells[49]. In both studies we found a ~20% OSIR decrease for YFP-Bcl-x$_L$, and a ~5-10% OSIR increase for YFP, compared with untransfected cells. The OSIR increase in YFP cells could not account for the decrease in OSIR observed in response to YFP-Bcl-x$_L$ nor was it accompanied by alterations in mitochondrial morphology in this study.   Whether YFP alters other scatterers in the cytoplasm remains to be evaluated.

To investigate the role of the Bcl-x$_L$ TM domain and mitochondrial localization in mediating the observed optical scatter response and changes in mitochondrial morphology, we used a YFP-Bcl-x$_L$-ΔTM protein construct, in which Bcl-x$_L$ lacks its last 21 amino acids corresponding to the C-terminal TM domain.   In contrast to YFP-Bcl-x$_L$,

expression of YFP-Bcl-x_L-ΔTM was diffuse within the cells, did not localize specifically on the mitochondria, did not alter light scattering, and was not accompanied by an increase in the percentage of mitochondria with an expanded matrix. These results show that alterations in light scattering and mitochondrial morphology that are induced by expression of YFP-Bcl-x_L, require the C-terminal TM domain and localization of YFP-Bcl-x_L on the mitochondria.

To find out whether the BH domains of Bcl-x_L are necessary to induce the observed mitochondrial alterations, we synthesized a YFP-TM construct consisting of eYFP fused to the last 21 amino acids of Bcl-x_L, without the rest of the Bcl-x_L protein. As expected this construct targeted the mitochondria. In addition, like YFP-Bcl-x_L cells, cells expressing YFP-TM had a lower OSIR value and a larger proportion of mitochondria with an expanded matrix. Thus, the BH domains of Bcl-x_L are not required, and the TM domain is sufficient to elicit changes in mitochondrial matrix morphology. However unlike Bcl-x_L, a significant portion of the YFP-TM cells also exhibited a very large number of vesicles, suggestive of excessive autophagy. At the same time, more than 50% of the YFP-TM cells were found to contain very bright and punctate mitochondria observed by fluorescence (Figure 2-1C, last panel pair). By normalizing the YFP fluorescence to that of anti-complex V fluorescence, we found that the fluorescence intensity of the punctate mitochondria is greater than the fluorescence of filamentous looking mitochondria within a same cell. It is therefore conceivable that excessive YFP-TM expression on these punctate mitochondria may have targeted them for autophagy. The punctate mitochondria also had a larger proportion of pixels with high OSIR values compared with the bulk of the YFP-TM cells (Figure 2-3). A direct correlation between light and electron microscopy will be required to confirm whether

the autophagocytic vesicles are indeed the result of mitochondrial autophagy, and if they correspond to the bright and punctate mitochondria observed by fluorescence. Kaufman et al had reported that mitochondrial targeting requires two basic amino acids flanking the TM domain at each end [70]. While in our construct, the TM domain was not explicitly preceded by the x-domain of Bcl-x_L[70], it did include two basic amino acids at each end (Figure 2-1A): …K…R. on the YFP end, where K is part of the YFP terminus, and RK at the other end, coming from the original C-terminal of Bcl-x_L. This is consistent with the fact that fluorescence of our YFP-TM construct co-localized with anti-complex V fluorescence, and therefore was not simply a result of subcellular YFP-TM aggregation without specific localization to the mitochondria. Still, why YFP-TM, and not YFP-Bcl-x_L, should elicit an excessive autophagocytic response and whether this response is affected by the amino acids or the YFP protein surrounding the TM domain remains to be determined.

Finally, to investigate the role of the TM domain in apoptosis resistance, we measured the amount of cell death after 24 hours of staurosporine treatment, which was previously shown to induce apoptosis in CSM 14.1 and iBMK cells[49, 69]. These results showed that in both CSM 14.1 and iBMK cells, expression of YFP-Bcl-x_L-ΔTM confers similar cell death resistance as expression of YFP-Bcl-x_L. We also found, unexpectedly, that expression of YFP-TM confers a moderate level of apoptosis resistance (Figure 2-7). Our data suggest that the presence of the BH domains is sufficient for apoptosis resistance and does not require the TM domain or morphological alterations. This would be possible since for example, the hydrophobic pocket formed by the BH1-BH3 domains of Bcl-x_L-ΔTM could still sequester BH3-only proteins in the cytoplasm, and in this way inhibit activation of Bax and Bak. Cytoplasmic mutants of Bcl-x_L may also still have

minor associations with subcellular membranes and have been reported to retain effective anti-apoptotic activity[70]. Certainly, in the case of Bcl-2, a Bcl-2 cytoplasmic mutant lacking the transmembrane domain still pocesses anti-apoptotic activity[71], and the viral Bcl-2 homolog E1B19K, which targets organellar membranes by myristoylation, lacks the C-terminal transmembrane domain and inhibits apoptosis by binding Bax or Bak[72]. Nevertheless, our results do not exclude the possible secondary role of the TM domain in apoptosis resistance. In particular, the absence of the BH domains in the YFP-TM construct did not fully obliterate the construct's ability to confer apoptosis resistance, and YFP-TM expression did alter mitochondrial morphology. While the mitigating role of autophagy in response to staurosporine induced cell death in the YFP-TM cells is not clear, the TM domain of Bcl-x_L could still contribute to apoptosis resistance by mediating initial changes in mitochondrial morphology.

In this study, we have used light scattering and electron microscopy to show that the TM domain of Bcl-xL mediates changes in mitochondrial morphology. The OSIR in our study measures the intensity ratio of wide-to-narrow angle scatter. This ratio decreases monotonically as a function of diameter, D, as shown in Figure 2-2B. However, when particles are not spherical, the OSIR can be sensitive to particle shape, in addition to particle size[30]. We had also previously shown that for particle geometries approximating mitochondria, varying the refractive index ratio from 1.005 to 1.1 changes the OSIR by only 1.8%[30]. As such, changes in the refractive index, which could potentially correspond to changes in particle composition, cannot account for the measured changes in OSIR. One way to interpret the OSIR would be to state that the angular scattering properties of the mitochondria represented by the OSIR, are equivalent to the OSIR properties of a sphere of a given size. In this sense, the OSIR decrease measured in our

present study, corresponds to an increase in this "equivalent scattering diameter". However, the relationship between this equivalent diameter and the fine geometrical structure of the mitochondrial matrix is not clear. The expansion of the matrix and reduction in intracristal spaces seen by electron microscopy could correspond to an actual increase in matrix size, or could represent matrix reconfiguration without a significant change in matrix volume. A full three-dimensional characterization of the change in matrix geometry, membrane contact sites, and matrix volume will be necessary to further the electron microscopy and scattering results presented in this study.

Changes in mitochondrial morphology can be produced by several mechanisms, including control of matrix potassium, calcium and ADP content, changes in the configuration of the adenine nucleotide translocase (ANT) and interaction with dynamin related proteins that normally control mitochondrial fusion and fission. Bcl-2 family proteins have been shown to influence some of these processes. Nonetheless, the transient and steady-state modulation of mitochondrial morphology by Bcl-2 family proteins has not been fully characterized. An increase in mitochondrial volume effected by uptake of K^+ into the matrix has been shown to stimulate respiration [73]. However, t-Bid was shown to facilitate cytochrome c release by increasing mitochondrial K^+ uptake, while Bcl-2 was shown to inhibit K^+ uptake and cytochrome c release, and increase efflux of K^+ from the matrix [74]. At the same time, overexpression of Bcl-2 correlated with an increase in mitochondrial matrix volume, but no change in matrix K^+ concentration, and may be related to a greater capacity for calcium uptake into the matrix[75]. ADP induced phosphorylation leads to a change in mitochondrial morphology from the "orthodox" to the "condensed" configuration, in which the matrix is shrunken with increased intracristal and intermembrane spaces but without an obvious reduction in

total mitochondrial volume[55]. Conversely, binding of adenine nucleotide to the ANT, switches the ANT from its cytosolic to matrix facing conformation, can result in a decrease in intracristal spaces and inner membrane contraction without a change in matrix volume[76-80]. The ANT may be able to influence K^+ influx into the mitochondria[73, 81]. However, changes in morphology involving the ANT, may also be mediated by an alteration of inner/outer membrane contact sites rich in ANT (e.g. ANT-VDAC contact sites)[80, 82]. In this context, Bcl-xL was shown to facilitate ADP/ATP exchange across the ANT in response to growth factor withdrawal[83]. Consistent with this, Bcl-2 was shown to increase ANT mediated ADP/ATP exchange, while Bax was shown to decrease it[84]. Bax dimers are also thought to facilitate cytochrome c release by localizing and interfering with inner/outer membrane contact points involving the ANT[85]. Lastly, recent evidence points at the interaction of Bcl-2 family proteins with dynamin related proteins. Truncated Bid (tBid), can disrupt Optic atrophy 1 (OPA1) oligomers, which control cristae junctions, and was shown to facilitate cytochrome c release through a drastic inversion of inner membrane curvature and remodeling of intercristal spaces independently of mitochondrial fusion[59, 63]. On the other hand, Bax promotes mitochondrial fusion in healthy cells by interacting with mitofusin-2[2]. This interaction may be inhibited during apoptosis and contribute to unbalance Drp-1 induced mitochondrial fragmentation[2]. Changes in morphology involving matrix expansion, as observed here, could for example precondition mitochondria to counteract death promoting morphological alterations induced by pro-apoptotic Bcl-2 members, such as tBid and Bax/Bak. Alternatively, matrix expansion could provide a means to control mitochondrial metabolism and diffusion across mitochondrial membranes by controlling intracristal space and contact points between the inner and outer membranes. While the

specific (anti-apoptotic) function of Bcl-x$_L$ that requires localization to the mitochondria and alteration of matrix morphology even prior to a death stimulus has not been elucidated in this study, our results suggest that the requisite localization of wild type Bcl-xL to mitochondria may be necessary for a bioenergetic function mediated by the TM domain and matrix morphology, and distinct from and not requiring BH3 domain sequestration.

Chapter 3 Development of Optical Scatter Imaging System with a Digital Micromirror Device

3.1 Introduction

Alterations in the morphology of subcellular organelles are an important indicator of cellular function. To facilitate detection and tracking of subcellular morphology changes, an optical scatter imaging (OSI) technique was developed to assess subcellular particle size within living cells[4]. In a transmission microscope utilizing the central dark-ground method, wide and narrow angles of scatter were selected by varying the diameter of a circular diaphragm in a Fourier plane, conjugate to the objective's back focal plane. OSI non-invasively measures the intensity ratio of wide-to-narrow angle scatter (OSIR, Optical Scatter Image Ratio) in real-time and does not require any exogenous labeling, cell fixing, or organelle isolation.

For spherical particles, the OSIR was shown to decrease monotonically as diameter increases for D<2 μm and agrees with Mie theory prediction. In living cells, we showed in the previous chapter that this technique is able to detect mitochondrial morphological alterations, which were mediated by the Bcl-x_L transmembrane domain, but could not be observed by fluorescence or differential interference contrast images[1]. OSI provides in situ morphological information as well as quantitative size distribution. Furthermore, this method does not rely on fitting models to the measurements, the size information directly relates to the measurement of OSIR.

Nonetheless, one of the limitations of OSIR is that despite being sensitive to changes in particle shape and size, it could not distinguish between them. As most light scattering methods, OSI records the "equivalent diameter" but not the actual dimension neither the change in shape of non-spherical particles. However, naturally occurring

particles, including organelles, are rarely perfectly spherical, and, under some conditions, organelles can change shapes. For example, an increase in OSIR corresponds to a decrease in diameter for spheres, however, ellipsoidal particles rounding up to spherical with no change in volume also results in an increase in OSIR[30]. Therefore, it is difficult to interpret whether a change in OSIR corresponds to change in size or shape or both.

Light scattered by a scatterer depends on the scatterer's size, shape, and orientation. Hence, by manipulating scattering in Fourier plane, we will be able to characterize morphology of non-spherical particles. Thus, to quantify the shape of non-spherical organelles, such as mitochondria, and the anisotropic morphological changes that characterize their activity, we extended the previous OSI method by replacing our variable diameter iris with a spatial light modulator (SLM) as a Fourier filter. In this study, we chose a digital micro-mirror device (DMD) for light modulating. Compared with other spatial light modulators the DMD has several advantages, including high efficiency, and high contrast ratio. Also, the mirrors could be programmed to tilt within tens of microseconds providing high speed spatial filtering. The use of DMD spatial modulators in a microscopy system is typically in a conjugate image plane as adjustable, dynamic apertures to increase spatial resolution, gain flexibility, or get quantitative analysis. In contrast to theses studies, we use a DMD in a conjugate Fourier plane, which results in significant chromatic and geometric aberrations. In this chapter, we describe the design of a new DMD-based OSI system and how the imaging artifacts may be overcome.

3.2 Microscope setup

The digital micromirror device (DMD) based optical scatter imaging setup is shown in Figure 3-1. Narrow-band (see Results) laser light from a ~5 mW Helium-Neon laser ((Research Electro-optics, Boulder, CO, line at $\lambda_0 = 632.8$ nm) was passed through a ground glass diffuser (DG20-120, Thor Labs, NJ) spinning > 1,000 RPM. The diffused light was collected by an aspheric lens (C330TM-A, Thorlabs, NJ) with 3.10mm focal length and 0.68NA, collimated by an f25.4mm lens and coupled into a multimode fiber (F-MLD-C-5FC, NA=0.29 Newport, Irvine, CA) by an aspheric fiber collimation package (Thorlabs F220FC-B, f = 11 mm, NA=0.25). The fiber output was collimated using an f = 15.3 mm, NA=0.16 aspheric lens (F260FC-A, Thorlabs, NJ) and launched
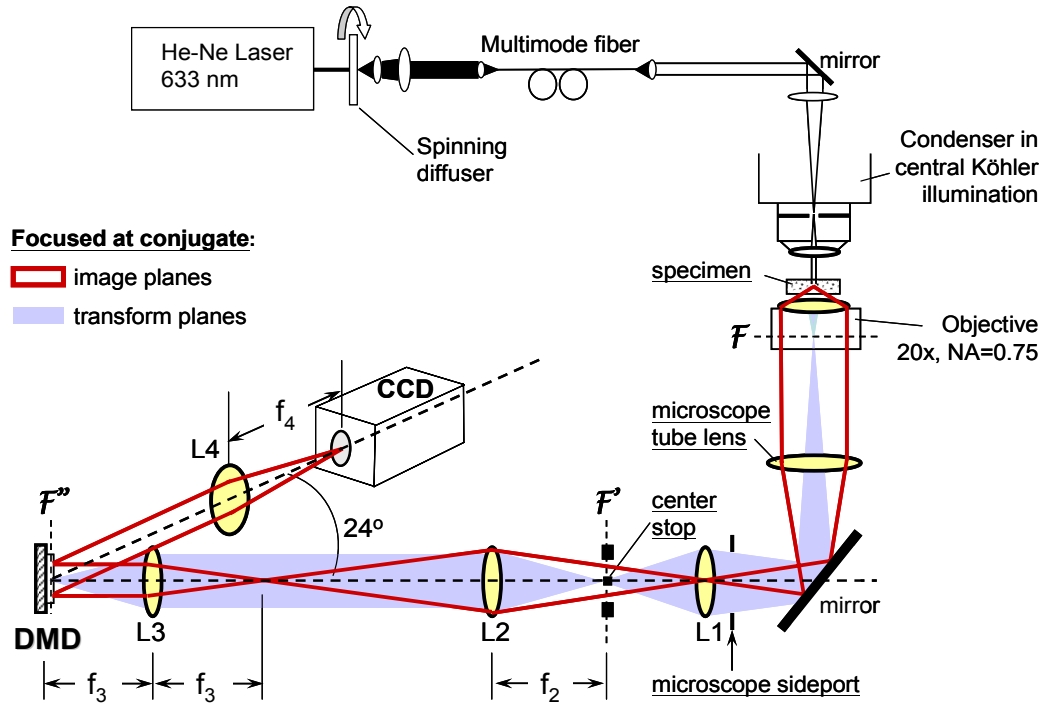
Figure 3-1 Digital micromirror device- (DMD-) based optical scattering imaging system. The DMD is placed in conjugate Fourier plane F". Unscattered light is blocked at F' and F" (light blue beam). The magnification of the Fourier plane on the DMD is controlled by lenses L2 and L3, while the magnification of the final image was varied by changing the focal length of L4. The imaging beam (red trace) is collimated on the DMD before final focusing onto the charged coupled device camera (CCD).

into the condenser of an inverted microscope (Zeiss, Axiovert 200M, Göttingen, Germany) aligned in central Köhler illumination (NA<0.05) to provide a spatially coherent plane wave. The microscope was fitted with a 20x objective (NA=0.75). The DMD (TI 0.7 XGA DMD, Texas Instruments) was placed in a conjugate Fourier plane, F'', outside the microscope side port. The DMD consists of 1024×768 array of aluminum micro-mirrors, 13.68×13.68 μm^2, each mirror operates in a bistable mode, tilted diagonally +12° or -12° [33, 34]. Four lenses, L1-L4 were used to control the magnification of the image transform on the DMD, to collimate the imaging beam (red beam) on the DMD, and to focus the specimen's image on the CCD camera (Cascade 512B, Roper Scientific). It was important to collimate the imaging beam on the DMD to avoid geometric aberrations originating from reflection by the array of tilted DMD mirrors. The camera was placed on a rail positioned at an angle of 24° with respect to the microscope's side port axis to collect scattered light reflected by the DMD mirrors tilted +12° ("on" mirrors). Scattered light reflected by mirrors tilted -12° ("off" mirrors) was directed away from CCD and blocked. Image acquisition consisted of collecting on the CCD a stack of spatially filtered dark-field images using a spatial filter bank generated by the DMD. A beam block consisting of a 0.3mm graphite pencil lead glued to a No. 1 cover slip was centered in F' (Figure 3-1) to minimize the dark-field background (See section 3.5).

3.3 Requirement of narrow-band light source to avoid chromatic aberrations

Due to the tilt of the DMD mirrors during on/off actuation, the desired image of the object is projected at the specular reflection angle relative to the DMD mirrors. Thus, when placed in a conjugate Fourier plane, the DMD mirrors act like a blazed grating, and the desired image is found in the sixth order of diffraction by the DMD rather than the zeroth order (m=6 for wavelength λ= 655.5nm). The DMD mirrors are 13.68μm x 13.68μm and tilt around their diagonal at 45°. Thus, if the microscope aperture were projected on the full width of the DMD, which has 768 mirrors, this grating would have N= 1536 lines with 9.67μm separation and its resolution would be $\lambda_0/\Delta\lambda$= mN= 9216 with $\Delta\lambda$=0.069nm around 633nm. Thus, a source bandwidth $\Delta\lambda$ >0.07nm will create a significant chromatic aberration consisting of smearing a point source object in the direction of the mirror tilt (the extent of the smear scales with the source bandwidth). An example is shown for a filtered halogen source with λ_o= 633 $\pm$ 0.5 nm (Figure 3-2A). This problem was resolved with the use of a narrow band laser source, such as the Helium Neon laser, and speckle removal as discussed in the next section (section 3.4).
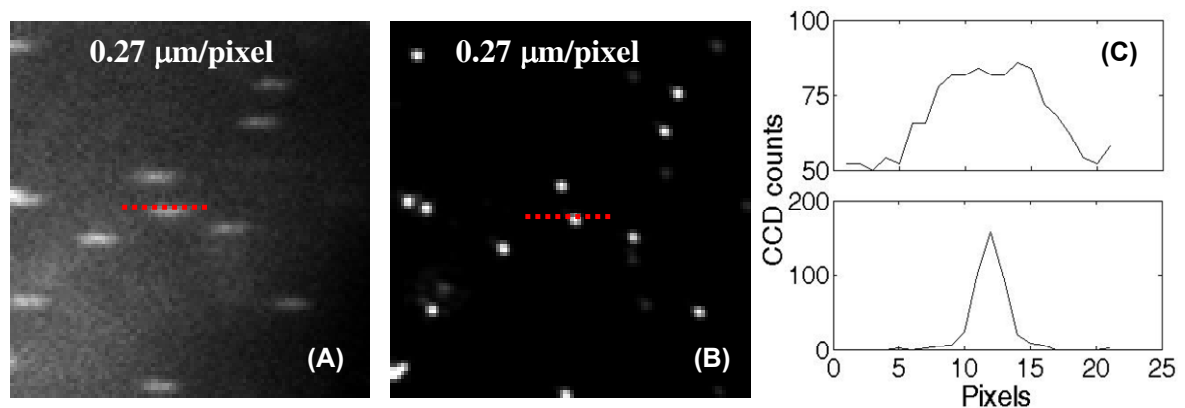
Figure 3-2 (A) Spheres (0.465μm) imaged using a filtered halogen lamp at 632.8±0.5nm (1500ms exposure). (B) The same spheres imaged using the He-Ne laser at 633nm (300ms exposure). (C) Upper panel: cross section of the signal in panel (A) at dashed red line, lower panel: cross section of the signal for the same sphere in panel (B). Each pixel corresponds to 0.27μm.

The bandwidth of our He-Ne laser was 0.0006 nm (Figure 3-2B). As can be seen in Figure 3-2 C lower panel, the current resolution of the system when operating in unfiltered dark field is 0.675μm. This resolution compares well with the 0.515μm diffraction limit resolution expected from our 0.75 NA objective using the Rayleigh criterion for distinguishing two point sources. Increasing the magnification would have allowed us to better sample the point spread function with more than two pixels.

3.4 Spinning diffuser reduced speckles

To reduce the speckle effect due to imaging with the laser source, we placed a ground glass diffuser spinning >1,000 RPM before collimating the laser into the optical fiber. Figure 3-3A shows the background imaged without the diffuser. The uniformity of the background in the whole image was 2261±1597 (mean ± standard deviation)
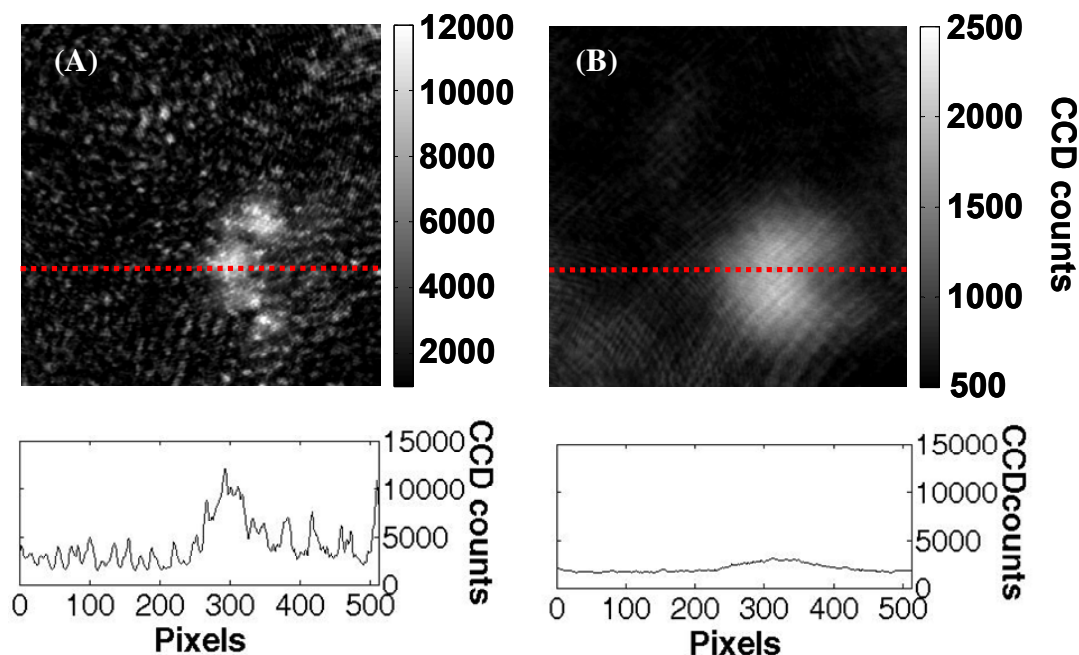
Figure 3-3. Images of the background using the He-Ne laser as light source (A) without the spinning diffuser (100ms exposure), and (B) with spinning diffuser (2000ms exposure). The background consisted of a water sample sandwiched between a microscope slide and coverslip. Lower panels show the cross section of the signal at the red dashed line in each corresponding image.

counts/100ms, which had a 70% coefficient of variation (CV). Using the spinning diffuser to wash out the speckle background, a more uniform background was obtained (Figure 3-3B), with 36±14 counts/100ms or a CV=39%. Focusing on the lower right regions with high signal, the uniformity of background without diffuser was 4408±2279 counts/100ms, CV=52% and the uniformity of background with diffuser was 66±17 counts/100ms, CV=26%. However, diffusing the laser light results in 98% loss of signal due to the compromised coupling of the laser light into the fiber and microscope.

3.5 Minimizing the dark-field background

Using the diffraction pattern of the graticule, we measured the intensity of the zeroth order diffraction pattern (undiffracted light) before and after blocking it with the DMD The contrast ratio of signal before and after turning the DMD mirrors off was 3200:1. In the imaging plane, the average background intensity was ~934±302 (mean±standard deviation of all pixels) counts with 2000 ms exposure when blocking the zeroth order with only the DMD in second conjugate Fourier plane (F" in Figure 3-1). To further reduce the dark-field background, we placed a beam stop made of a 0.3mm graphite
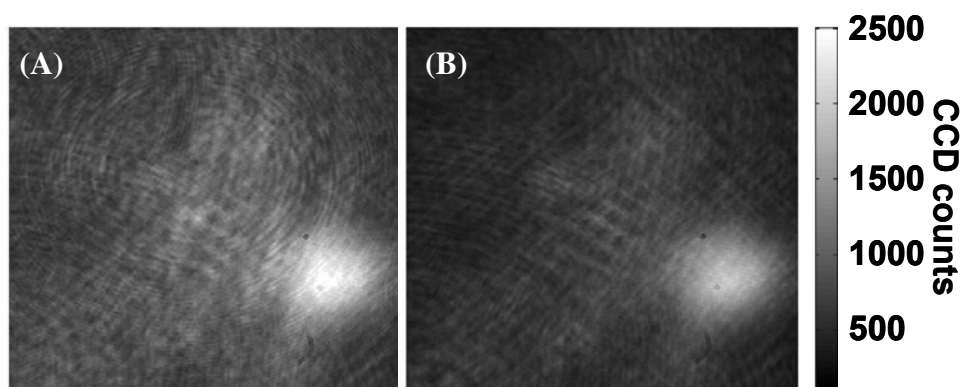
Figure 3-4. Images of a water sample sandwiched between a microscope slide and cover slip collected without (A) and with (B) the center stop at F'(see Fig. 1) 1000ms exposure.

pencil lead at the center of the first conjugate Fourier plane, *F'*, to block the zeroth order scatter. When the beam stop was added, the contrast was improved to 4200:1 and the average background intensity was reduced by 30% to ~647±243 counts with 2000 ms exposure (Figure 3-4).

3.6 DMD generated geometric aberrations

Using the DMD as a light modulator in a conjugate Fourier plane allows us to pass or block scattered light at any combination of angles within the numerical aperture of the microscope. To maximize spatial frequency resolution, the object transform should be magnified to fill the full 768-mirror diameter of the DMD. However, when this is the
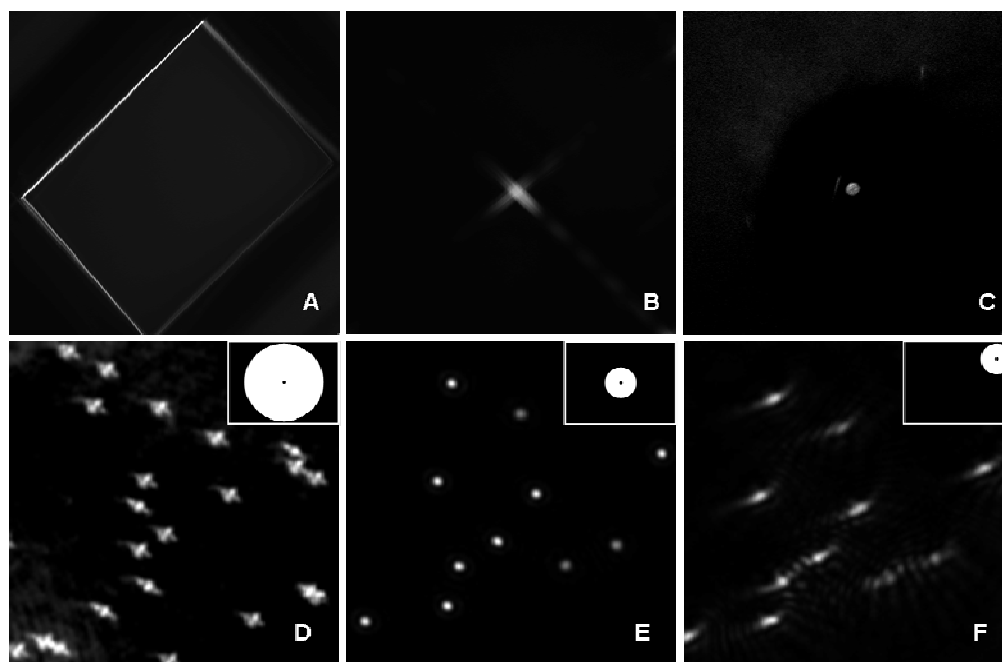
Figure 3-5. (A) Image of DMD with collimated light (diameter of 760 micro-mirrors) when all mirrors were turned off. The edges of the DMD were bright despite the fact that all the light should be reflected away by off mirrors. (B) Focus the collimated beam on the camera with a cross appearing on the focused spot. (C) Same as (B) but the diameter of collimated light was reduced to 600 micro-mirrors. (D) Dark field image of 0.465 μm spheres with transform occupying ~760 mirrors in diameter centered on DMD, (E) ~300 mirrors in diameter centered on DMD or (F) ~300 mirrors in diameter positioned at the upper right hand corner of the DMD. In this case, the DMD was translated to that the incident beam remained aligned with the shifted aperture. In each case, insets show the position of the DMD apertures; the white area indicates 'on' mirrors; the black area 'off' mirrors.

case, we obtained image aberrations (Figure 3-5D). The DMD possesses a band of 6-8 mirrors at the edge of its active surface. This "pond of mirrors" (POM) is always in the binary "0" position. For the DMD orientation chosen here, a binary value of "0" corresponds to the "on" position and deflects the light towards the CCD. To investigate whether this rectangle of inactive mirrors gave rise to the aberrations shown in Figure 3-5D, we shone a collimated beam toward DMD by removing L3 and imaged the DMD on the CCD camera. With all the mirrors turned off no light should be reflected by the DMD, but since the DMD blocking efficiency is not 100% (contrast = 3200:1), some light will still be sent to camera. However, the edges of DMD appeared brighter than the center (Figure 3-5A), indicating light was actually reflected toward the CCD by this POM. We adjusted L4 to focus the beam on the camera and found that the beam is not focused to a spot but shows a cross on top of it (Figure 3-5B). We reduced the diameter of incident beam with an iris diaphragm. When the beam covered a diameter of only 600 micro-mirrors the bright edges in Figure 3-5A disappeared, and the beam could be focused to a spot without aberration (Figure 3-5C). However, when the DMD was rotated by 180°, such that the rectangle of inactive mirrors with binary value of "0" was in the "off" position; a point source object could be imaged as a spot when in focus, but a cross shaped aberration appeared when slightly out of focus, despite precise alignment of the optics in the setup (data not shown and was done by lab colleague, Rob Pasternack). These geometric aberrations were ultimately eliminated by reducing the size of the Fourier plane by switching L3 from a 250mm lens to a 100mm lens to cover a diameter of only 300 micro-mirrors aligned to the center of the DMD (Figure 3-5E). We also found that when the Fourier plane covers a diameter of 300 micro-mirrors, but is placed near one of the DMD edges, the aberrations appeared again (Figure 3-5F). This was also

the case when DMD was rotated by 180°. These data suggest that in addition of POM, the edge of the device rather than the area of the DMD aperture is responsible for this effect. These aberrations were not due to the tilt of the DMD mirrors. Actuating the DMD mirrors to "float" mode (all mirrors kept flat) and rotating the whole device to reflect the light onto the CCD gave a similar result (data not shown).

3.7 Elimination of multiple images

The DMD is composed of a 2D array of periodically spaced mirrors so that the DMD acts as a 2D grating and forms images in every diffraction orders. The final image will contain multiple images of the object as the original image of the object becomes convolved with the pixels of the DMD. If the elements of the DMD device are too large compared to the width of the object transform, the desired image of the object will overlap with the images found in the adjacent diffraction orders. This effect is exacerbated by the fact that the transform was reduced to occupy less that the full area of the DMD (See section 3.6). An image of the field of view shows the extent of this multiple image overlap (Figure 3-6A). To avoid the multiple images, we closed the microscope aperture and imaged only the center non-overlapped field of view. However, this allows us to image only small field of view. To image a large sample area, the microscope field-stop needs be opened to increase the field of view, which results in image overlap. The additional images were deconvolved using a standard Wiener filter algorithm (Matlab's "deconvwnr" function). For this, three pixels were selected that were positioned on the same object feature, which appeared in the multiple images. These pixels were simultaneously shifted to let the point in the central image fall on the center of the image. The pixels were then weighted by their intensity in the original

image.   The image of the three centered and intensity weighted pixels (green pixels in Figure 3-6A) consisted of the point spread function used for the deconvolution algorithm. The deconvolved image is shown in Figure 3-6B. Figure 3-6C shows pixel histograms of two pairs of adjacent regions with and without overlap, before (regions (a1, a2) and (a3, a4) in Figure 3-6A) and after (regions (b1, b2) and (b3, b4) in Figure 3-6B) deconvolution. After deconvolution, the intensity distribution of areas (b1, b2) and (b3, b4) become largely similar attesting to the success of the algorithm at eliminating the overlapping signal. The intensity of the peripheral images was at most 12 % of the intensity in the central image.   Thus the additional shot noise contributed by the additional background in the overlapping image regions is not significant.
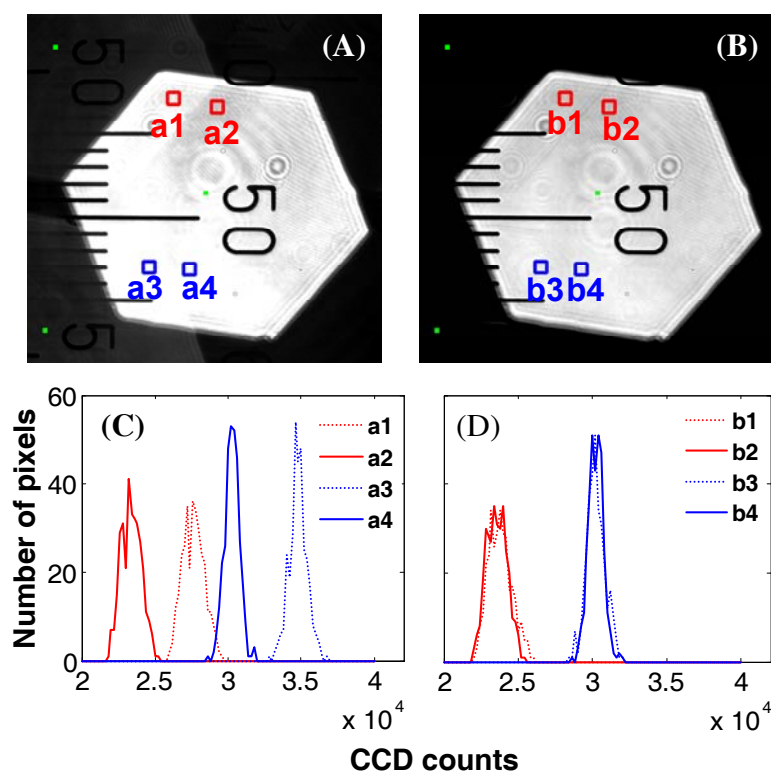
Figure 3-6. (A) Field of view showing image overlap due to diffraction at the DMD. The green spots are the pixels chosen for point spread function during deconvolution. Note that the spots were enlarged for clarity; only one pixel at the center of each spot was actually used for the point spread function. (B) Same image after deconvolution. (C) Pixel histograms of the areas within the red and blue squares in panel (A). (D) Pixel histograms of the same image areas in panel (B).

3.8 Current signal performance

To check the system performance, we measured the signal intensity as a function of the exposure time and calculated signal-to-noise ratio under each exposure. Using a uniform background, we measured the signal intensity corresponds to different exposure time. For each exposure time, we acquired 30 images and measured the signal intensity at one pixel. From the 30 images, we calculated the mean and standard deviation of intensity at each exposure time. In Figure 3-7A, we can see that the intensity increased linearly (R square = 1) from ~16 to ~60,000 counts as exposure time increased from 1 to 4000ms. Figure 3-7B shows the signal-to-noise ratio (2.7 to 220) as a function of intensity counts. The signal-to-noise ratio increases as intensity/exposure time increase, and it is close to the theoretical shot noise (square root of intensity). Hence, for signal intensity above 40 counts, the signal increases linearly as exposure time increase with signal-to-noise ratio above 10.
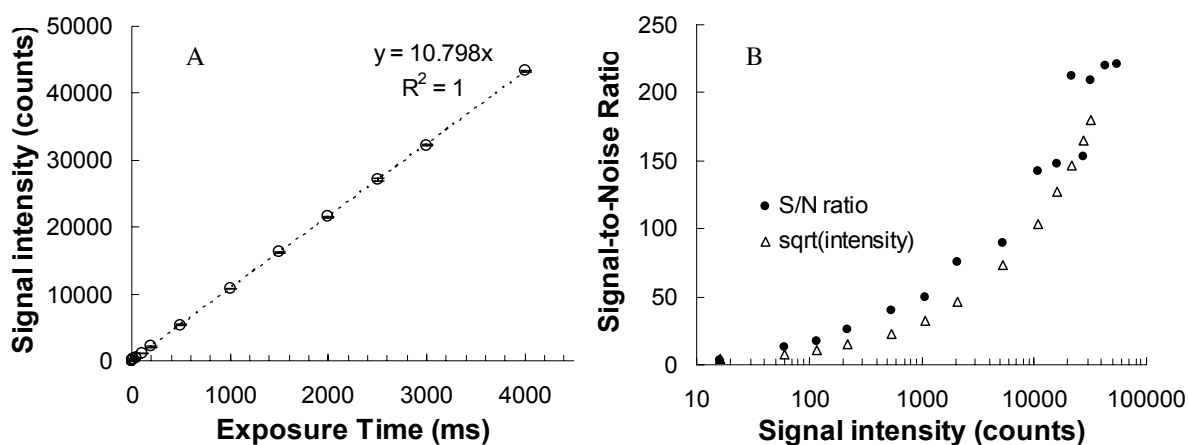
Figure 3-7. 30 images (128×128 pixels) were acquired for each exposure time and the signal intensity were getting from the same pixel of all images. (A) Linearity of signal intensity as the function of exposure time. (B) Signal-to-noise ratio (circles) as a function of signal intensity compared with theoretical shot noise (square root of intensity).

3.9 Discussion

In this study, we extended our size-sensitive optical scatter imaging (OSI) method to analyze the shape of the scattering objects by utilizing a spatial light modulator to perform spatial filtering. Here, we chose a digital micro-mirror device (DMD) for light modulation. While most DMD applications utilize the DMD in a conjugate imaging plane, we use the DMD in a conjugate Fourier plane. A DMD in the conjugate Fourier plane can select any angular combination of scattered light and enables the characterization of morphology of non-spherical particles. Compared with other spatial light modulators, such as liquid crystal devices, the DMD has several advantages, including high efficiency, high contrast ratio, and high mirror actuation speed. However these advantages were offset by specific issues pertaining to the use of the DMD in a conjugate Fourier plane. In addition to the DMD, we also tried to use a liquid-crystal (LC) microdisplay (LC 2002, Holoeye) for light modulation. Similar to the DMD, the LC microdisplay consists of 800×600 pixels, 32μm×32μm each, and is capable of filtering light in any arbitrary two-dimensional area but in transmission mode. When the DMD is used in a conjugate Fourier plane, it acts as a blazed grating and results in resolving light when the mirrors are tilted with a resolution of ~0.07 nm. Hence images are distorted if the light source is not monochromatic. For this reason, a He-Ne laser with an operating bandwidth of ~0.0006 nm is used. With the current system setup and light source used, the specular reflection falls between orders (m=6.21) and energy is distributed into multiple orders, which is an "off-blaze" condition. To utilize the energy more efficiently, the diffraction peak could be better lined up with an order to be in the "blazed" condition. For our system, the center blazed wavelength associated with the 6th order of diffraction is 656nm. Using this wavelength instead of 633nm could therefore

improve throughput. Currently, we measured a throughput of 45%, which is lower than the reported 68% efficiency in the manual specs, and is likely due to the off-blaze condition. To reduce speckles and interference fringes due to the coherence of the He-Ne laser, a spinning ground glass diffuser was used. However, diffusing the laser light resulted in significant loss of signal. On the other hand, when using the LC microdisplay, the diffraction peak happens at $\theta m = 0°$ hence the least resolvable wavelength difference $\Delta\lambda = \lambda/mN = \lambda^2/Na(\sin\theta m - \sin\theta i) \sim\infty$ and the light collected would not be spectrally resolved (where λ = wavelength of the light source, m = diffracting orders, N = number of pixels, a = distance between pixels, θi = incident angle and θm = diffracting angle). While the use of a monochromatic light source was not critical, the throughput of the LC microdisplay we used was very poor and the brightness of a regular halogen bulb was not adequate. We measured the signal-to-noise ratio of the DMD-based system using E. coli as model samples to find out the minimum exposure time required. Due to the images shifting issue and noise other than shot noise, we did not get a reasonable signal-to-noise ratio as the function of exposure time (data not show). However, for the intensity above 64 CCD counts, we got signal-to-noise ratio above 15; hence to get signal-to-noise ratio above 15 we need to expose the samples to get at least 64 counts. In this case, the exposure time was 5ms to get 64 counts of signal.

When micromirrors near the edges of DMD are used, an aberration with 45° orientation is observed regardless of the size of the Fourier plane. This effect is likely due the DMD geometric design. The POM around the edges of the DMD may leak stray light, which when reflected from these mirrors may be Fourier transformed into image plane and result in the observed aberration. However, there is another source of aberration due

to the DMD edges other than the POM. This aberration does not appear when the image is in focus, and appears and becomes worse when the image moves out of focus while the POM caused aberration is always there. In addition, the POM caused aberration appears to be straight and the other aberration appears somewhat like astigmatism. We suspect the other aberration might be due to the potential curvature of the DMD device. Using only 300×300 mirrors in the center area could eliminate this effect. Though the LC microdisplay consists only 800×600 pixels, an area diameter up to 600 pixels could be used and the edges did not affect image quality. In this case, the DMD allowed for Fourier filters with frequency increment of 0.00785 (cycles/μm)/mirror, while the LC microdisplay allowed for 0.004 (cycles/μm)/pixel increment. One big advantage of the DMD over the LC microdisplay is the image contrast, which is 1:3200 for the DMD and 1:100 for the LC microdisplay. This intensity ratio is important in our application, where inefficient blocking of the light at the chosen spatial frequencies can result in significant background and increased noise in the filtered images. In our system, we designed two conjugate Fourier planes, and placed an additional center stop at F' (Figure 3-1) to block the non-scattered light and further reduce background. For the DMD system, 30% of the background was reduced by adding this center block. However, blocking of other orders totally relies on SLM itself. Thus, compared with the DMD, the poor blocking efficiency of the LC microdisplay will result in increased background contributed by the inefficiently blocked higher order scatter. A state-of-the-art LCD with contrast reported around 1:1000 may improve this issue.

While the DMD could only perform binary modulation, a LC microdisplay could be used to display gray scale images or perform phase modulation. This advantage makes the LC microdisplay more flexible for complex Fourier filtering. The 2D array geometric

property of both DMD and LCD microdisplay results in multiple overlap image. The size of each pixel of a LCD microdisplay is bigger than a DMD, hence the overlapping is worse when using a LCD microdisplay. For the current application, since the size of field of view was not an issue, we simply avoided this problem by using only the center non-overlapping area of the image. This overlapping issue could be solved by image deconvolution, and our preliminary deconvolution results demonstrated the feasibility of eliminating multiple images with deconvolution method.

Based on the OSI prototype, we developed an improved optical scatter imaging system with a digital micromirror device. As in the initial OSI system[4], the system relies on analyzing the transform of the sample object. The transform is formed in a Fourier conjugate plane of our imaging system and contains the scatter intensity at every scatter angle collected by the microscope's numerical aperture. However, the previous Fourier filter consisted of a circular iris with variable diameter and only permitted the collection of scatter intensity integrals between a center stop and the outer edge of the iris. In contrast, the DMD Fourier filter used here consists of a 1024x768 array of micro-mirrors $13.7x13.7\mu m^2$ each. When activated by a programmable actuator, the mirrors can be tilted in tens of microseconds to deflect the incoming light towards or away from the collection optics. The micro-mirror array therefore acts like an array of shutters, which can be used to pass or block the light scattered at any desired combination of scattering angles within the numerical aperture of the microscope system. This can in turn be used to characterize particle shape by analyzing the scattering pattern in two dimensions.

Chapter 4   Validation of OSIR Measurements Using The DMD-based Optical Scatter Imaging System

4.1 Introduction

Using the initial optical scatter imaging (OSI) setup with the variable circular iris as Fourier filter, we successfully predicted sphere diameter from the optical scatter imaging ratio (OSIR) measurement. We were also able to detect alterations in mitochondrial morphology mediated by the C-terminal transmembrane of Bcl-x_L in living CSM cells (see chapter 2). This circular iris was manually adjusted to be open (for high-NA filtering) or closed (for low-NA filtering), and these two positions though reproducible may not be exactly the same during every adjustment due to human error or error of the mechanical device. In the previous chapter, we described an improved OSI system using a programmable digital micro-mirror device (DMD) for generating 2-D binary filters. The DMD can be programmed to display desired filter patterns precisely. In addition, using the diffraction orders of a graticule falling on the mirror position, we could calibrate the filtering frequency for every alignment of the system and get precise filter angles.

To investigate the performance of the new DMD-based optical scatter imaging system in this study, we implemented the circular high- and low- NA filters on the DMD and performed the OSIR measurements. We first measured the optical scatter imaging ratio of spheres of different size in aqueous suspensions and compared the measurements to the results obtained from the previous OSI system and Mie theory prediction. The Brownian motion of the spheres in aqueous suspensions results in position changes of spheres between images captured at high- and low-NA filters or later using the filters of

an optical Gabor-like filter bank. Therefore, we embedded the spheres in polyacrylamide gel and also measured the optical scatter imaging ratio of these stationary spheres.

To see whether the effect of the Bcl-x_L TM domain on mediating the morphology of mitochondria can also be observed in other cell types, we measured the optical scatter imaging ratio immortalized baby mouse kidney (iBMK) cells. We used two types of iBMK cell lines: the Bax/Bak expressing iBMK cells (W2 cells), and Bax- and Bak-deficient iBMK cells (D3 cells). Like the CSM cell variants, we stably transfected W2 and D3 cells with YFP, YFP-Bcl-x_L, YFP-Bcl-x_L-ΔTM, and YFP-TM. Using the three sets of cell lines, we investigated whether the effect of the Bcl-x_L TM domain is cell type dependent or Bax- and Bak- dependent.

The optical scatter imaging ratio is a function of particle diameter. Using the relationship between OSIR and particle diameter, we converted the measured optical scatter imaging ratio to particle size and converted the OSI pixel histograms to particle size distributions. We applied this conversion to spheres and found the peaks to fall approximately at the corresponding size. Applying the conversion to the CSM cell data, we found that cells over-expressing Bcl-x_L or the transmembrane domain of Bcl-x_L contain particles with larger "equivalent scattering diameter".

4.2 Materials and methods

4.2.1 Generation of DMD OSIR filters

Binary images in Bitmap format were loaded onto the DMD via the DMD Discovery 1100 control software (Texas Instruments). Bitmap images were generated containing 768×1024 pixels with values of 0 or 1 that matched the individual positions of the micromirrors in the DMD array. A pixel value of zero results in turning on the

corresponding mirror such as light falling on it is deflected towards the CCD, while a pixel value of 1 corresponds to turning off the mirror and deflecting its reflection away from the CCD.

Using the diffraction pattern of a graticule with line spacing b=10μm, we converted mirror positions on the DMD to spatial frequency in cycles/μm. For the graticule, each order of diffraction collected by the objective falls at an angle, θ, with respect to the optical axis. The spatial frequency passed by the 20x dry objective was defined as $\sin\theta/\lambda_0 = m/b$; m is the order number. The positions of the diffraction orders were measured in mirrors from the zeroth order position (zero frequency component at the center of the DMD) in the Fourier plane with the aid of a mirror ruler consisting of DMD passbands at regular intervals and plotted against diffraction order number (or spatial frequency). For the 63x oil immersion objective, the spatial frequency was defined as $n\sin\theta/\lambda_0$ where n is the refractive index of the immersion oil = 1.515.

For the system setup using the 20x objective, a linear fit to the measurements gave 12.55 mirrors per diffraction order, or 0.00796 cycles/μm/mirror and a correlation coefficient of 0.99. The maximum aperture (NA= 0.75) corresponds to NA/λ_0= 1.185 cycles/μm or a radius of 149 DMD mirrors. The microscope aperture was not projected on the full width of the DMD to avoid image aberrations originating from the edges of the device (See Chapter 3). A central area with 12 mirrors in radius was turned off to block zeroth order scattering. For high NA (HNA) filter, the 13th to 260th mirrors from the center were turned on to pass $3° < \theta < 48°$; and for low NA (LNA) filter, mirrors 13th to 32nd were turned on to pass $3° < \theta < 9°$.

For the system setup using the 63x objective, a central area of 23 mirrors in radius was turned off to block scattering corresponding to $\theta < 3°$. For the HNA filter, the 24th to 384th mirrors from the center were turned on to pass $3° < \theta < 67°$; and for the LNA filter, mirrors 24 to 70 were turned on to allow $3° < \theta < 10°$ to pass. The angles of the HNA and LNA filters were chosen to match the design of the initial OSI system with variable iris as filter.

4.2.2 *Homogeneous aqueous suspensions of spheres*

Monodisperse polystyrene spheres (Polysciences, Warrington, PA) with refractive index = 1.6 were suspended in water and adjusted to have scattering coefficient $\mu_s \sim 0.01 \mu m^{-1}$. The aqueous sphere suspensions were sandwiched between a microscope slide and a 22mm × 22mm coverslip separated by 75 μm thick double sided tape (Scotch®, 3M) and then sealed with VALAP (1:1:1 v/v/v mixture of Vaseline, lanolin and paraffin). For the initial OSI setup, spheres with diameter 0.356, 0.548, 0.771, 1.053, 2.061, 3.156, 6.359 μm were used; and for the DMD-based OSI system, 0.356, 0.465, 0.771, 0.989, 1.53, 1.826, 3.156 and 5.778 μm spheres were used.

4.2.3 *Stationary spheres*

Polystyrene spheres were diluted in 2.5% polyacrylamide gel solution (stacking gel solution for Tris-glycine SDS-polyacrylamide gel); a 3μL aliquot of these spheres in polyacrylamide was placed between a microscope slide and a 22mm x 22mm coverslip and allowed to gel thus immobilizing the particles within the sample. The thickness of the gel was approximate 5.2 μm. The final concentration of spheres corresponded to a scattering coefficient, $\mu_s = 0.0025 \ \mu m^{-1}$ for sphere diameters smaller than 1μm and $\mu_s = 0.005 \ \mu m^{-1}$ for spheres larger than 1μm. Samples were prepared at very low

concentration so that particles were separated from each other and individual particles could be observed.

4.2.4   Cell culture and generation of stable cell lines of iBMK W2 & D3

Bax/Bak expressing iBMK cells (W2), and Bax- and Bak- deficient iBMK cells (D3) were generously provided by Dr. Eileen White[86]. iBMK W2 and iBMK D3 cells were transfected with YFP, YFP-Bcl$_{xL}$, YFP-Bcl$_{xL}$-ΔTM or YFP-TM using lipofectamine 2000. Stable clones were selected by gneticin (G418) sulfate (Invitrogen) and isolated foci with yellow fluorescence were picked, serially diluted and replated in 96-well plates to obtain clonal cell-lines.

The iBMK W2 and D3 cell lines were maintained in Dulbecco's modified Eagle's medium (DMEM) supplemented with 10% (V:V) fetal bovine serum (FBS), 100 Units/ml penicillin, and 100 μg/ml streptomycin. FBS was from Germini Bio-Products, DMEM, penicillin, streptomycin were from Invitrogen. iBMK cells were kept in culture at 38°C in an 8.5% CO2 in air atmosphere. 24 hours before imaging, iBMK cells were cultured on glass coverslips to allow attachment. Coverslips were then mounted on a steel plate and sealed with VALAP; the growth medium was replcaced with Leibovitz's L-15 medium (Invitrogen) supplemented with 10% FBS, 100 Units/ml penicillin, and 100 μg/ml streptomycin.

4.3 Validation of OSIR in homogenous aqueous sphere suspensions

4.7.1   OSIR calibration curve with 63x objective

Aqueous suspensions of polystyrene spheres, diameters spanning 0.3 to 6μm, were used to illustrate the dependence of OSIR on particle size for index ratio m= 1.2 (=

$n_{polystyrene}/ n_{water}= 1.6/1.33$). The suspensions were 75 μm thick and had scattering

coefficient $\mu s \sim 0.01 \mu m^{-1}$. Since samples were suspended in water, the scattering angles of

high- and low- NA filters for calculating Mie theory prediction should account for the

refraction index of water, n_{water}. The corresponding spatial frequencies associated with

the high and low NA filters become $n_{water}\sin\theta/\lambda_0$ As a result, the calibrated angles for

high NA become $3.38° < \theta < 90°$, and $3.38° < \theta < 11.29°$ for low NA. We compared the data

acquired from the initial setup with circular iris with that obtained from the DMD-based

system using 63x oil objective in both cases. Figure 4-1(A) shows representative

ratiometric images of spheres with different diameters measured with the initial OSI

setup. Experimental data collected with both systems agreed with OSIR predictions

calculated from Mie theory for m=1.2 (Figure 4-1 (B)). For diameter <2μm, OSIR

decreased monotonically as diameter increased. This result shows that our new DMD-
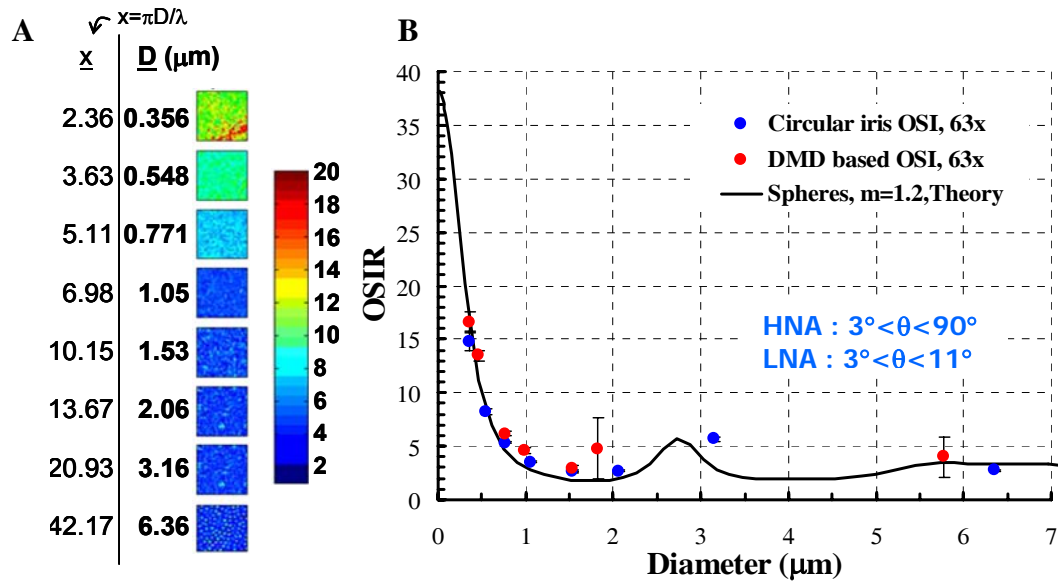
Figure 4-1 A) Representative ratiometric images of spheres with different diameters, color bar indicates OSIR. B) Dependence of OSIR on particle diameter for index ratio m= 1.2. Experimental data taken with initial OSI system with circular iris (blue circles) and data taken with DMD-based OSI system (red circles) are compared with OSIR predictions (black line) calculated from Mie theory. The error bar indicates standard deviation in a given ROI.

 based OSI system produces the expected measurement of OSIR. In this 63x setup using the DMD system, we projected the microscope aperture on the full width of the DMD and did not correct for image aberrations originating from the edges of the device (chapter 3). Even though the images had these aberrations, the system provided good OSIR measurement, which depends on the signal collected independently of image quality.

4.3.1   OSIR calibration curve of the DMD-based setup with 20x objective

To increase the field of view for acquiring data from a larger sample area, we set up the system using 20x objective. Again, we measured the dependence of OSIR on particle diameter using aqueous suspensions of polystyrene spheres with diameters spanning 0.3 to 3µm. The scattering angles for high NA are $2.58°<\theta<34.32°$, and $2.58°<\theta<6.91°$ for low NA after taking water's refractive index into account. Figure 4-2 shows experimentally measured OSIR data as a function of sphere size. Though they flatten a bit faster, the experimental data are close to the theoretical predictions.
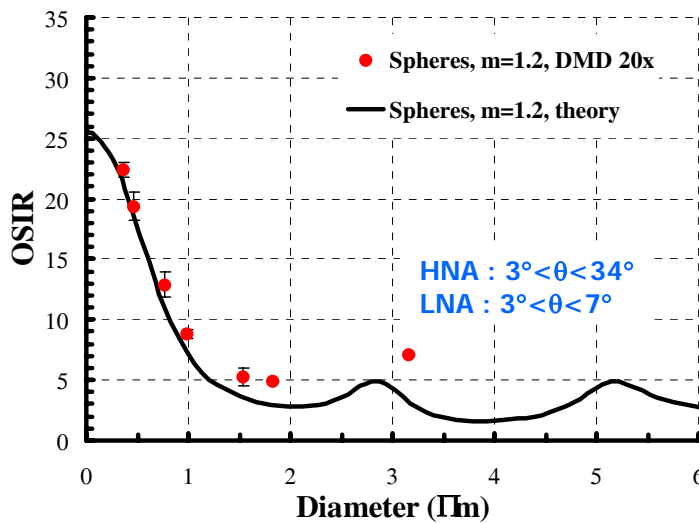
Figure 4-2 Dependence of OSIR on particle diameter for index ratio m= 1.2. Experimental data taken with DMD based OSI system with 20x objective (red circles) is compared with OSIR predictions (black line) calculated from Mie theory. Error bars represent standard deviation of three different experiments. Size 1.826 and 3.156 µm were only measured one.

4.4 Validation of OSIR in stationary spheres

The OSIR measurements of aqueous suspensions of polystyrene spheres agree well with Mie theory prediction. However, for cells and most practical cases, the particles are usually not homogeneous but a mixture of different sizes and shapes. In addition, to better understand their optical scattering property, it is necessary to study the behavior of individual spheres. Spheres suspended in water move around due to Brownian motion so that the position of the spheres changes between images captured at high-NA and low-NA filters. The movement of particles makes the spheres suspension impractical for studying mixtures of different particles if the scattering is to be correlated with the position of spheres of a given size. To study individual spheres and investigate if the OSI technique is able to distinguish particles with different diameters, we prepared sphere samples in 2.5% polyacrylamide gel to immobilize the spheres. We then applied the
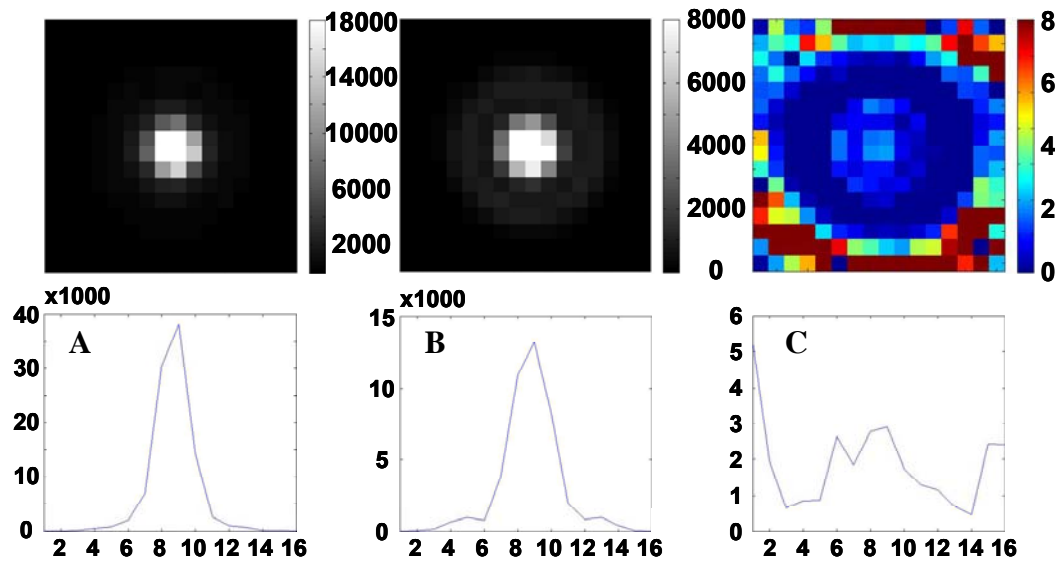
Figure 4-3 Images taken with the initial OSI setup with 63x objective. (A) Upper panel: high-NA image of single stationary 1.53 μm sphere, color bar shows intensity counts. Lower panel: cross section of the high-NA image. (B) Upper panel: low-NA image of the sphere shown in A, color bar shows intensity counts. Lower panel: cross section of the low-NA image. Red dash shows where the segmentation is applied (C) Upper panel: OSIR image of the sphere, color bar shows OSIR. Lower panel: cross section of the OSIR image.

OSIR measurements on these stationary spheres to see if we can still extract a correct size measurement.

An ideal situation for the OSI study would be for every individual sphere to give a uniform OSIR everywhere inside the pixels it occupies. However, because of diffraction, it is obvious that there will be OSIR differences within a sphere's image, and that the ratio image of a sphere occupies more pixels than the sphere's actual size (Figure 4-3) due to the low-NA filtering. As shown in Figure 4-3 (C), there appear high ratios around a sphere due to the very low low-NA signal there. To avoid of these effects and noise from the background, segmentation was applied. For images taken with the initial setup and the 63x objective, the images were segmented around the first bright ring of the low-NA image of the spheres and the OSIR was then averaged within this segment. Figure 4-3 (B) shows an example of where the segmentation is applied around a 1.53μm sphere (red dash). For images taken with DMD-based system and the 20x objective, segmentation was applied around the first dark ring of the high-NA image. Figure 4-4 shows the OSIR calibration curves of stationary spheres taken with either the OSI system with circular iris at 63x or the DMD-based OSI system at 20x. For smaller spheres
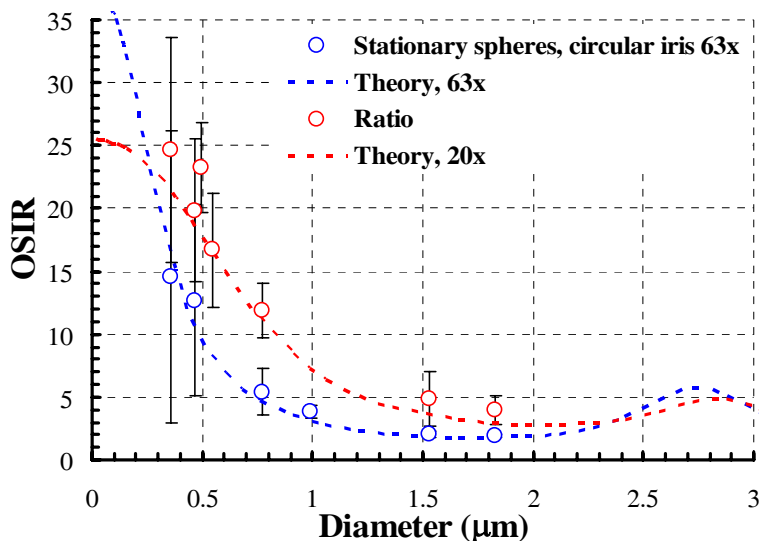
Figure 4-4 OSIR measured from stationary spheres compared with theory. Blue circles are data acquired with system using the circular iris for filtering, and blue dashed line is the theoretical prediction. Red circles are taken with DMD based OSI system with 20x objective and red dashed line is the corresponding theoretical prediction. Error bars represent standard deviation among OSIR measured from individual spheres.

(diameter < 0.5μm), the errors were very large though the average OSIR is close to theory. The large errors were likely due to the low signal of these spheres and poor signal-to-noise ratio. In the case of aqueous suspensions, signals were collected from large number of spheres (ex. 2.66×10^{11} spheres/ml for 0.35μm spheres) which therefore increased the signal-to-noise ratio.

4.5 Theoretical dependence of OSIR on refractive index and collecting angle

When angles of high-NA and low-NA were fixed, numerical simulation of light scattering by spheres shows that the OSIR is independent of refractive index ratio, m, for 1<m<1.1, which is about the ratio for subcellular organelles (Figure 4-5, solid lines). On the other hand, a slight difference in the low-NA angle will result in a big difference in OSIR (Figure 4-5, dash). This can cause measurement errors while using manually adjusted iris diaphragm, and the angles must be controlled precisely when aligning the system. The property that OSIR only depends on particle diameter and angles of high and low-NA is still an advantage when applying the OSI technique for subcellular study;
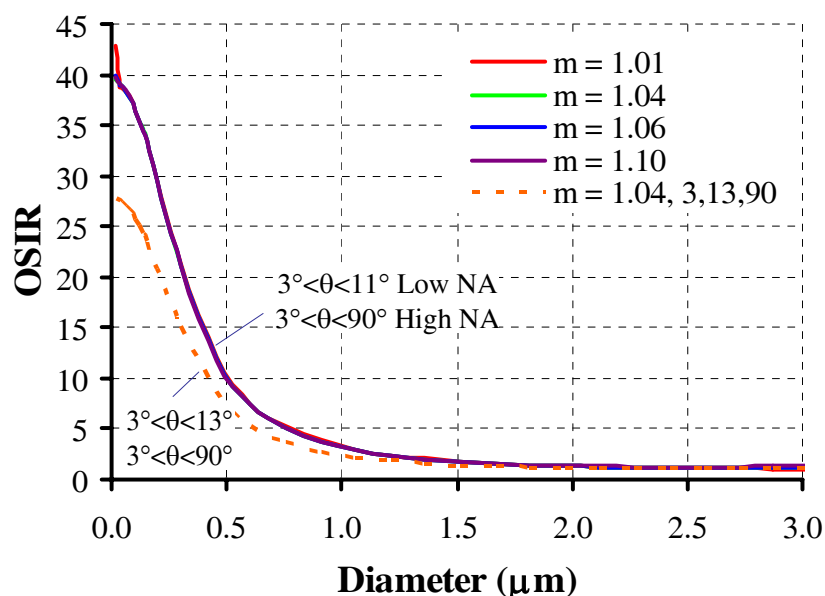
Figure 4-5 Numerical simulations of light scattering by spheres with index ratio, m = 1.01, 1.04, 1.06, or 1.10 for high-NA angle = 3°<θ<90° and low-NA angle = 3°<θ<11°; and with m = 1.04 for high-NA angle = 3°<θ<90° and low-NA angle = 3°<θ<13°

when the system is well aligned or calibrated, the slight differences of index ratio within cellular samples could be ignored.

4.6 Effect of Bak/Bax on the optical scatter imaging ratio

4.6.1 OSIR of iBMK W2 variants – 63x initial OSI system

In chapter 2, we have shown in CSM cells that the C-terminal transmembrane domain of Bcl-x_L could mediate changes in mitochondrial morphology which resulted in a decrease in OSIR when cells over-expressed YFP-Bcl-x_L or YFP-TM. To see whether the effect of Bcl-x_L TM domain can also be observed in other cell types, we repeated the experiments on iBMK W2 cells. We generated a set of W2 cell lines over-expressing YFP, YFP-Bcl-x_L, YFP-Bcl-x_L-ΔTM, and YFP-TM, like the CSM cell variants, and investigated subcellular changes caused by these variants by acquiring the ratiometric

	W2	W2YFP	W2ΔTM	W2Bcl-xL	W2TM
	0.93	1.00	0.81	0.87	0.88
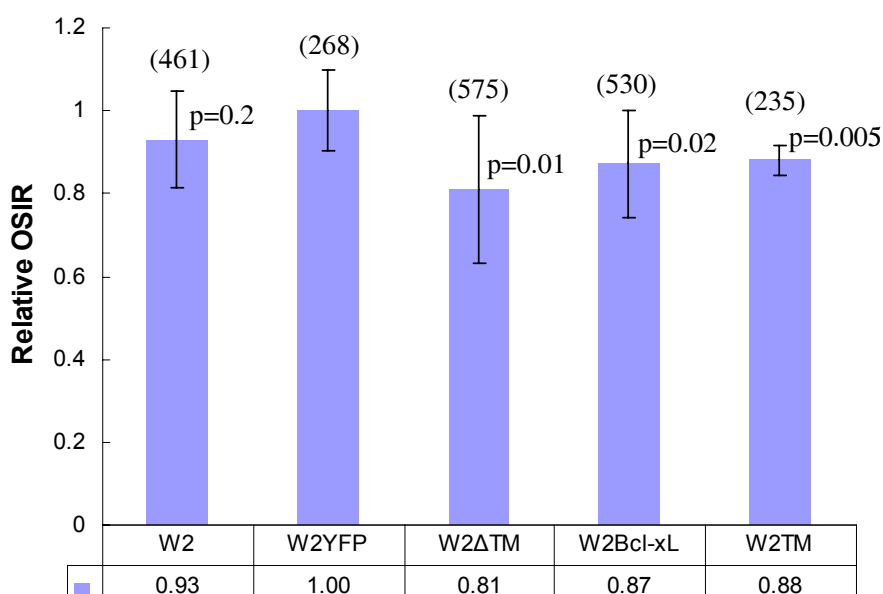
Figure 4-6 Mean OSIR per cell normalized to mean OSIR of W2YFP for each of the five BMK W2 cell variants. Error bars represent standard deviation of mean. Numbers next to each bar showing the p-value of student t-test of each variant compared to W2YFP, and the numbers in parenthesis are the number of cells tested.

optical scatter images (OSIR) using the 63x initial OSI system. To investigate the differences in OSIR among cell variants, the cell-by-cell average OSIR was measured. However, the results were collected from two system alignments at different times with slightly different low-NA angles. As we have shown in previous section, a small difference in filter angle will result in big difference in OSIR (Figure 4-5); these two sets of data could not be compared directly in terms of their raw OSIR value. To combine these results together, the cell-by-cell average OSIR of each variant was normalized to the average OSIR of the YFP variants taken at the same filter positions. Setting the average OSIR of YFP variant to one, we then compare relative changes of the OSIR to the YFP variant (Figure 4-6). As for the CSM variants, untransfected W2 cells show no significant change to W2 YFP (p=0.2, t-test). When YFP-Bcl-x_L or YFP-TM is over-expressed, the OSIR is 13% and 12% lower than W2 YFP variant, respectively (p<0.05). However, the OSIR measurements of W2 YFP-Bcl-x_L-ΔTM are 19% lower than W2-YFP.

4.6.2   OSIR of iBMK W2 vs. D3 – 63x initial OSI system

To investigate whether Bak and Bax play a role in the observed alterations of mitochondrial morphology mediated by the C-terminal transmembrane domain of Bcl-x_L, a Bak- and Bax- deficient cell line, iBMK D3, was used. We measured average OSIR per cell of iBMK W2 and D3 cells using either the initial OSI system with the 63x objective or the DMD-based OSI system with the 20x objective (Figure 4-7). The OSIR values of W2 and D3 cells are different when measured with initial OSI system or DMD-based system (2.51 vs. 1.91 for W2 cells, 3.33 vs. 2.93 for D3 cells, respectively) since the high- and low-NA angles are different. In addition, the OSIR values for the 20x DMD system correspond to particle diameters which are higher than the ones inferred from the

60x manual iris system. This was not expected since the same cell types were tested in both systems. Nevertheless, the D3 cells show higher OSIR than W2 cells in both systems (by a factor of 1.33 for the initial system and a factor of 1.5 times for the DMD-based system). The different OSIR values between W2 and D3 cells imply different subcellular morphology. This was also confirmed that there were more round features in the D3 cells compared with W2 cells by a lab colleague using optical-Gabor-like filtering (see chapter 5) with the DMD-based OSI system[87].
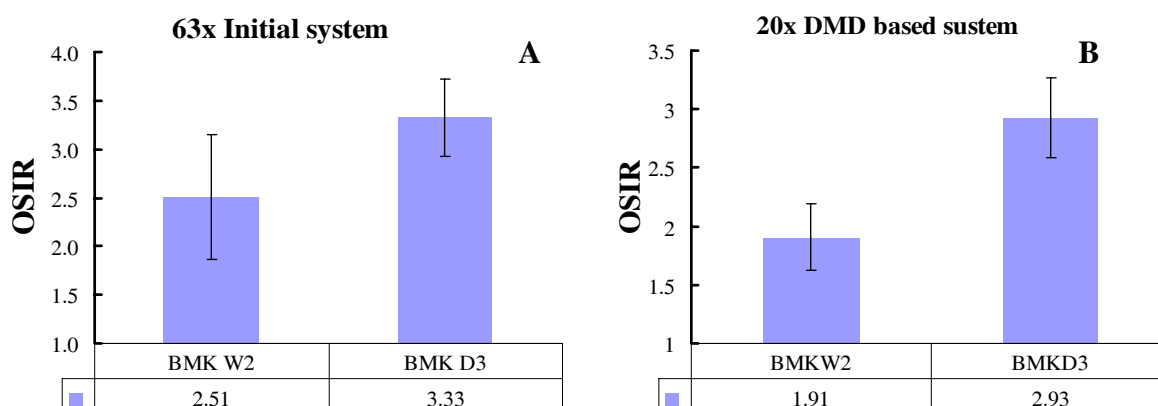
Figure 4-7 Mean OSIR per cell of iBMK W2 and iBMK D3. (A) Using the initial OSI system with 63x objective. (B) Using the DMD-based OSI system with 20x objective. The error bar represents the standard deviation of the mean.

4.6.3 OSIR of iBMK D3variants – DMD-based OSI system

In the previous sections we validated the new DMD-based OSI system against the previous system by comparing OSIR measurements of aqueous and stationary spheres and W2 and D3 cells. Here we use the DMD-based OSI system to measure the average OSIR of D3 variants. We compared the cell-by-cell average OSIR of the D3 cells variants to the D3 YFP variant and used a student t-test to compare each pair of data sets (Figure 4-8). D3 cells over-expressing YFP-Bcl-x_L have significantly lower average OSIR than D3 cells over-expressing YFP (p = 0.004). D3 cells over-expressing YFP-TM

also have a lower OSIR compared to D3 YFP, although the difference is not significant (p=0.16). As for the W2 cells, the D3 cells over-expressing Bcl-x_L-ΔTM also have a lower OSIR although this decrease is not as significant as for Bcl-x_L.

	BMKD3	D3YFP	D3ΔTM	D3Bcl-xL	D3TM
■	2.93	3.12	2.73	2.72	2.85
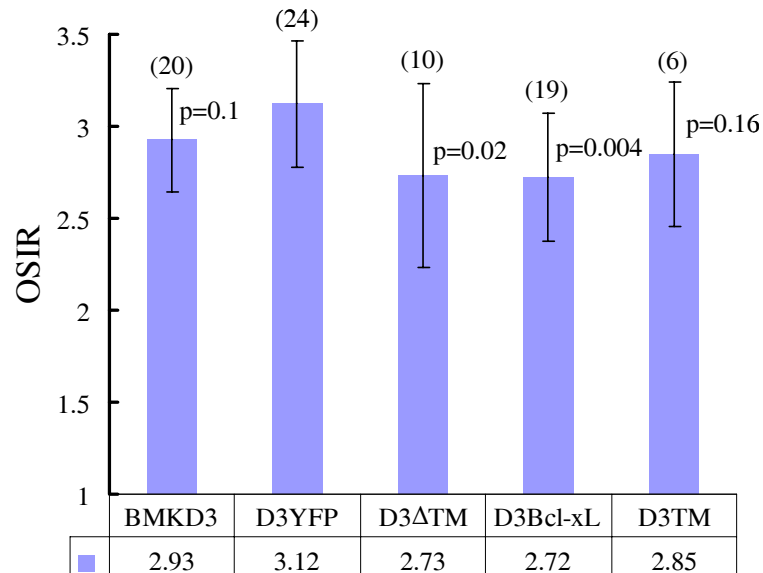
Figure 4-8 Mean OSIR per cell for BMK W2 and five BMK D3 cell variants. Measurements were taking with DMD-based OSI system with 20x objective. The error bars represent standard deviation of the mean. The numbers next to each bar showing the p-value of t-test of each variant compare to D3YFP, and the numbers in parenthesis are the number of cells tested.

4.6.4   Changes of OSIR of CSM, iBMK W2 and iBMK D3 variants

After normalizing the OSIR of the iBMK cell variants to the average OSIR of the YFP labeled cells, and the OSIR of CSM variants to the average OSIR of CSM YFP cells, we can then compare the OSIR among the CSM, W2 and D3 variants (Figure 4-9). When compared with untransfected cells, only CSM variants show significant differences. W2 and D3 variants have slightly different OSIR values compared to YFP cells, but the difference is insignificant (Figure 4-9 red stars). Cells over-expressing only YFP always have slightly higher OSIR than untransfected cells (~10%, though this was not as significant for W2 and D3 cells when tested with student t-test) and since all the

variants expressed YFP, cell variants over-expressing only YFP were used as control. In this case, over-expression of YFP-Bcl-x$_L$ resulted in significantly lower OSIR for all three cell types. Also, the level of Bcl-x$_L$ induced OSIR decreases was similar for W2 and D3 cells (13% decreases). CSM and W2 cells overexpressing Bcl-x$_L$-TM had lower OSIR, while D3 Bcl-x$_L$-TM showed no significant difference. While in the case of the CSM cells, Bcl-x$_L$ variants have slightly lower OSIR than the TM variants, the effect of Bcl-x$_L$ and TM was similar in the case of the W2 cells. In all three cell types, Bcl-x$_L$-ΔTM resulted in significant lower OSIR compared to the YFP variants.

	CSM/W2/D3	YFP	ΔTM	BCL-xL	TM
CSM	0.91	1.00	0.92	0.74	0.81
W2	0.93	1.00	0.81	0.87	0.88
D3	0.94	1.00	0.87	0.87	0.91
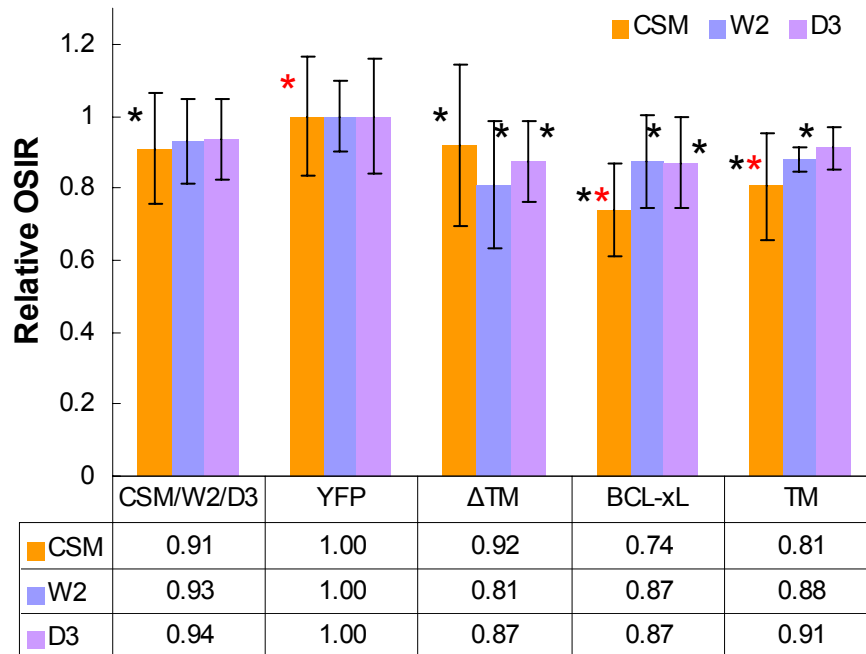
Figure 4-9. Relative OSIR per cell for CSM, iBMK W2 and iBMK D3 cell variants. OSIR of CSM, iBMK W2 and iBMK D3 cell variants was normalized to the average OSIR of CSM YFP, W2 YFP and D3 YFP, respectively. Black stars indicate t-test p value <0.05 when compared with YFP transfected cells. Red stars indicate p <0.05 when compared with untransfected cells.

4.7 Conversion of OSIR to particle size

4.7.1 *Particle size distribution of spheres in aqueous suspensions*

Ratiometric images could be plotted as pixel histograms to observe the detailed difference between samples rather than just compare the average values of OSIR. Figure 4-10 (B) shows examples of pixel histogram obtained from ratiometric OSI images of
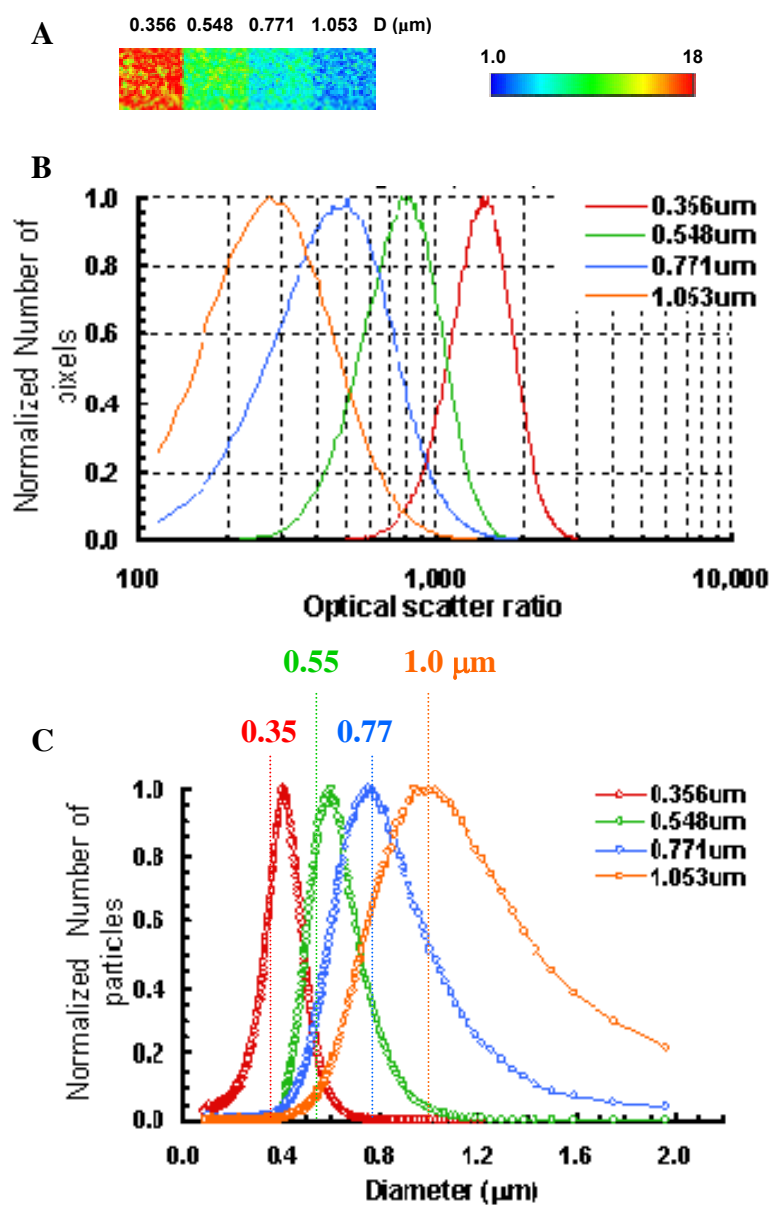
Figure 4-10 A) Ratiometric images of aqueous polystyrene spheres with diameter 0.3, 0.5, 0.7 and 1.0. B) Pixel histograms of ratiometric images shown in A. Histograms were normalized to the maximum number of pixels. C) Particle diameter distributions converted from pixel histograms. Distributions were normalized to the maximum number of particles.

different size spheres (aqueous suspensions). The histograms show good discrimination between the different particle sizes. Using the calibration curves shown previously (Figure 4-1), the pixel histograms could be converted to particle diameter distributions. Hence, for the x-axis, the OSIR was converted to diameter based on calibration curve obtained from Mie theory prediction (Figure 4-1, for m=1.2). For the y-axis, the unnormalized number of particles, N, was calculated as N = (unnormalized number of pixels $\times$ a^2) / π(D^2/4), where 'a' is the corresponding length of one image pixel in the object plane, and D is the corresponding diameter. Figure 4-10 (C) shows particle diameter distributions converted from pixel histograms (Figure 4-10 (B)). The peaks fall close to the expected particle diameter, dash lines in Figure 4-10 (C) indicate the expected peaks for those sphere sizes. For 0.771 and 1.053µm spheres the peaks fall roughly on the expected size and for smaller sizes, 0.356 and 0.548µm, the peaks are about 0.05µm bigger than the expected sizes. The variance in the estimated diameter increases as particle diameter increases. This is likely due to the variance in OSIR pixel value across a given particle when the pixel size is smaller than the particle's geometric cross section.

4.7.2   *Particle size distribution of cell variants*

OSIR is a function of particle diameter, and we have shown that the pixel histogram of spheres can be converted to particle size distribution. The bigger the particle the more pixels it occupied; hence number of pixels was divided by the corresponding cross section to get an estimate of particle numbers. Since this calculation is based on theory for spheres, and each sphere occupied more pixels than its actual size, the particle number and diameter are not absolute but give a relative relationship. Pixel histograms of OSI images of CSM cells resulted in a particle size distribution (Figure 4-11) with average

diameter D~1.65 µm, consistent with a significant mitochondrial contribution. Of course,

other organelles in this size range would also be included; but the different distributions

among variants should mostly due to mitochondrial morphology since they are

mitochondria targeting. The average diameter in Bcl-xL and TM cells was increased to

2.0 µm, while that of Bcl-xL-ΔTM cells slightly decreased to 1.6µm.
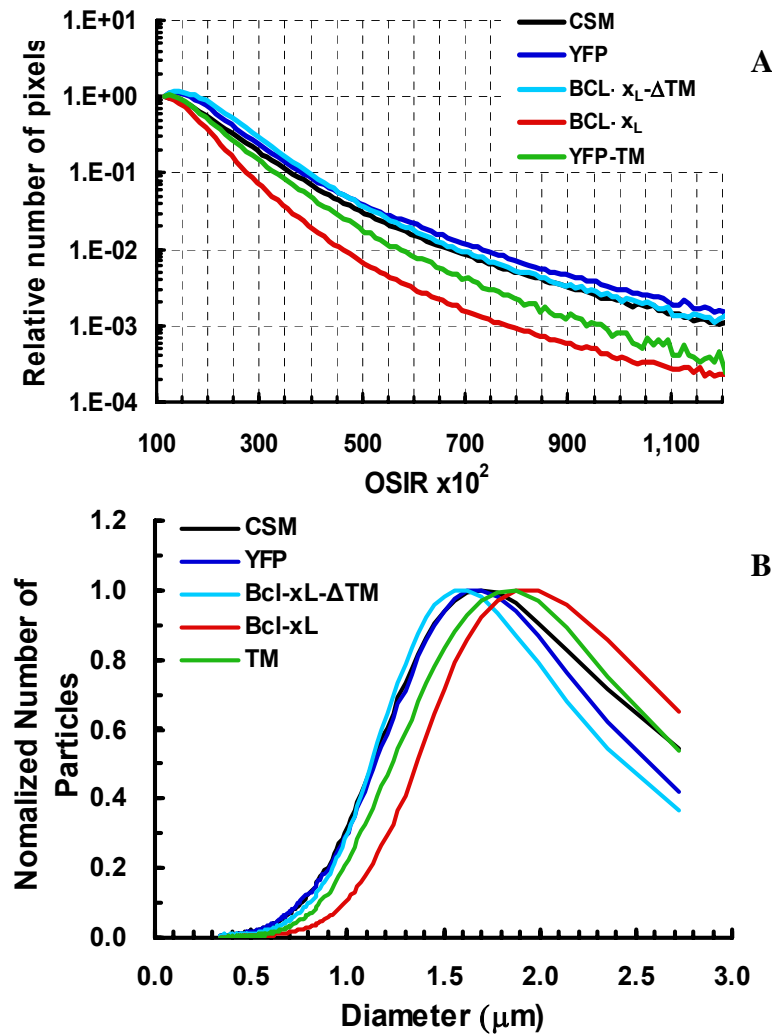
Figure 4-11 A) Pixel histograms of CSM cell variants normalized to the number of pixels with OSIR=1.15. B) Organelles size changes in CSM cell

4.8 Discussion

In this study, we validated the new DMD-based OSI system by utilizing the OSIR measurement. We measured the OSIR of homogenous aqueous and acrylamide immobilized spheres standards and compared the results with measurements taken with initial OSI system and Mie theory prediction. The ratiometric images were highly affected by the background subtraction, especially in the case of stationary spheres; strong background and poor background subtraction would yield high OSIR in the background region. In addition, around a sphere where the high-NA signal is divided by a very weak low-NA signal, the resulting OSIR could be extremely high. Thereafter, to get the expected OSIR value of stationary spheres, the images were segmented. To optimize the results, for the initial variable iris OSI system (63x), the sphere segments were set within the first bright ring of the low-NA image; and the sphere segments were set within the first dark ring of the high-NA image for the 20x DMD system. The use of different segmentation conditions was due to the use of different objectives: the 20x objective yielded lower resolution hence a larger Airy disk. The smaller the sphere size, the weaker the signal, thus stationary spheres with diameter <0.5μm have poor signal-to-noise ratio and the errors of their OSIR measurement were very large (CV~102% for 0.356μm spheres) although the averages were close to theoretical prediction. The aqueous suspensions contained large amount of spheres and provided enough signal even for small size particles so the error was smaller (CV~7% for 0.356μm spheres). Therefore, though the particle suspensions do not mimic biological conditions, they offer a good model sample for calibrating the system.

YFP is not expected to alter biological function and therefore should not alter subcellular morphology. In addition, YFP has its excitation maximum at 513 nm and its

emission spectrum has a peak at 527 nm, which should not interfere with light used in our system, with λ_0= 633nm. However, in all three cell types, cells over-expressing YFP always have slightly higher OSIR than untransfected cells (~10%) indicating YFP could be changing the scattering properties of the cytoplasm. OSIR simulations (Figure 4-5) show that for particle diameters smaller than 2μm, changes of OSIR due to difference of the refractive index ratio from 1.01 to 1.1 were not detectable. Whether YFP alters other scatterers in the cytoplasm remains to be evaluated. Nevertheless, since the existence of YFP causes the OSIR to increase, we compared the OSIR of the other variants to the YFP cells since all the variants expressed protein constructs that contained YFP.

According to theory, the value of the OSIR should be higher in the case of 20x setup than that of 63x setup for particle size bigger than 0.3μm (Figure 4-4, dash). However, we obtained a lower OSIR when testing cells in the 20x setup (Figure 4-7). In the case of 20x DMD-based system, the signal is much weaker (due to the spinning diffuser) and the signal-to-noise ratio is low. Therefore, the signal is buried in the noise and results in lower OSIR than expected. This would be remedied by using a higher power laser to get correct OSIR reading. Even though the absolute OSIR was lower than prediction in the case of the 20x DMD-based system, the relative difference between W2 and D3 cells was reproducible. Using either the initial OSI system with variable iris or the new DMD-based OSI system; we measured an increase in OSIR in untransfected D3 cells compared to untransfected W2 cells. Using optical Gabor-like filters, which will be described in next chapter, a lab colleague observed that there were more round features in D3 cells than W2 cells. This also correlated with the simulation results that rounding features have higher OSIR value than elongated ones for the same particle volume[30]. It was shown that Bax or Bak is required for normal fusion of mitochondria into elongated tubules in

healthy cells[2]. Lacking Bax and Bak, D3 cells may therefore contain more short, fragmented mitochondria and with higher OSIR.

In CSM cells, we reported that expression of YFP-Bcl-x_L and YFP-TM decreased OSIR and that the C-terminal transmembrane domain of Bcl-x_L mediates morphological changes of mitochondria. This alteration of forward light scattering is coincident with an increase in the proportion of mitochondria with an expanded matrix having greatly reduced intracristal spaces observed by electron microscopy (Chapter 2). However, when compared with cells overexpressing YFP, expression of YFP-Bcl-x_L-ΔTM also confirmed a decrease in OSIR although less significant. We might hypothesize that Bcl-x_L alters scattering properties mostly through its TM domain and partially from its BH domains. Interestingly, OSIR decreases induced by YFP-TM and YFP-Bcl-x_L-ΔTM are 19% and 8%, respectively; the sum of the decreases (~27%) is close to the YFP-Bcl-x_L induced OSIR decrease, which is 26%. Electron micrographs did not observe mitochondrial structure alteration caused by Bcl-x_L-ΔTM, however, Bcl-x_L-ΔTM could interact with Drp1 or Mfn2 to induce mitochondrial fragmentation or elongation. Especially Drp1, which recycles between the cytoplasm and mitochondria with a half-time of 50s[88], may interact with Bcl-x_L-ΔTM in the cytoplasm. Whether Bcl-x_L-ΔTM results in mitochondrial elongation/fragmentation or other morphological alteration requires further investigation. Currently, we are uncertain as to whether this alteration in scattering property was also observed in iBMK cells and whether it is affected by Bax/Bak, since the data collected are not sufficient (experiments were done twice for W2 cells and once for D3 cells). From the current data collected, the effect of Bcl-x_L and Bcl-x_L-ΔTM on reducing OSIR does not seem to be affected by the presence of Bax and Bak.

When Bax and Bak are absent, TM alone could not cause a significant OSIR alteration. This might suggest that the Bcl-x$_L$ transmembrane domain interacts with Bax or Bak and results in mitochondrial morphological changes. However, the decrease in OSIR induced by Bcl-x$_L$-ΔTM is similar to that of Bcl-x$_L$, or even higher in the case of W2 cells, which is inconsistent with the effects observed in CSM cells. Whether this observation is cell type dependent or due to experimental error requires further investigation. Also, since the OSIR is insufficient to characterize the morphology of non-spherical particles, this issue could be further studied using optical Gabor-like filtering, which will be described in next chapter.

We tried to convert OSIR to particle diameter and pixel numbers to particle numbers to get the particle size distribution within the tested samples. This conversion is successful in the case of 63x setup (Figure 4-10) for the spheres data. In the case of 20x setup, when only the x-axis was converted from OSIR to diameter and the y-axis remained to be number of pixels, we obtained histograms peaked at roughly the correct sphere size (data not shown). However, the conversion of the y-axis to number of particles failed, and for D=0.356μm we could not even get a peak. In the ratiometric images, a sphere occupies more pixels than its actual size, and this is even more significant in the case of 20x setup; since the high- and low NA angles are smaller the Airy disks are bigger. Therefore, though the crude approximation of number of particles, N = (number of pixels × a^2) / π(D^2/4), could still hold true for 63x setup, it failed for 20x setup. To get a better interpretation of particle size distributions, the actual pixels occupied by a sphere should be taken into account.

Though the OSIR only provides characteristic size, and could not reveal actual particle morphology, the simple measurement of OSIR is still a good indicator of subcellular morphological difference. It could for example be applied to quickly screen for the time point at which morphological changes take place after a given treatment, and further investigation could then be performed.

Chapter 5   Particle Sorting Based on Particle Size and Aspect Ratio

5.1 Introduction

In the previous chapters, we introduced a DMD-based OSI system validated this system using our relatively well established OSIR measurement. In this chapter, we apply the concept of Gabor filtering to characterize particle morphology. We designed optical filter banks consisting of Gabor-like filters with various scales or orientations. Gabor filters have been widely used for localization of spatial and frequency information in digital image and texture analysis [89]. A Gabor filter is a linear filter composed of a Gaussian envelope multiplied by a complex sinusoidal carrier. The Fourier transform of a Gabor filter's impulse response is the convolution of the Fourier transform of the harmonic function and the Fourier transform of the Gaussian function. The Gaussian envelope confines the filters in both space and k domain which optimizes the trade off between image resolution and spatial frequency resolution. Usually, a filter bank consisting of Gabor filters with various scales and orientations is created. The scale (or the period of the carrier) is sensitivity to the size of the object and the orientation is sensitive to the orientation an aspect ratio of the object. Gabor filters are usually used in digital imaging for localization of spatial and frequency information, texture analysis, target detection, fractal dimension management, document analysis and edge detection. They are widely used in image processing, computer vision, neuroscience and psychophysics[48].

Using model samples consisting of sphere and E coli, we applied the optical Gabor filtering on measuring the roundness, orientation and size of particles. We also showed that the method could be used at low resolution even when the image of the particle is blurred and the shape is not readily visualized. Furthermore, preliminary results suggest

the method could be applied on living cells to distinguish two populations of mitochondria with different morphology.

5.2 Materials and methods

5.2.1 Generation of DMD filters

We adopt the idea of Gabor filtering for discriminating particles based on their roundness, orientation and size. An optical Gabor-like filter bank consists of filters with various scales and rotations, where the scale is sensitive to the size and the rotation is sensitive to the orientation and aspect ratio of the particle. Here, we used the DMD to generate two Gabor-like filter banks to measure either the orientation or the size of a particle. Using the DMD to generate optical Gabor-like filters was described in a previous publication[90].

5.2.1.1 Optical Gabor-like orientation dependent filter bank

To measure particle orientation, a filter bank with frequency center at ~0.803 cycles/μm (or mirror #101 from the DMD center) and spanning various orientations (0° - 170°, with 10° increment) was used to infer particle roundness and aspect ratio. Since the DMD could only perform binary modulation, we approximated each Gaussian shaped Gabor filter by generating four binary concentric discs and continuously cycling them on the DMD at 150 frames/s during image acquisition on the CCD. This results in summing four intensity images instead of filtering both the phase and amplitude of the E-field in the Fourier plane, but provides a good approximation since the phases of the resulting four images are not significantly different due to the co-localization of the concentric disks in the Fourier plane.

5.2.1.2 Optical Gabor-like size dependent filter bank

For the measurement of particle size, we designed a filter bank with center frequencies spanning 0.28 to 1.25 cycles/μm and at three orientations (60°, 120° and 180°). We applied these filters to sphere samples. Since spheres have circular symmetry, various filter rotations are expected to produce similar intensity responses. Hence, we averaged the responses of the filters with a given scale over the different rotations.

5.2.2   Sample preparation

5.2.2.1 Immobilized spheres and E. coli sample for orientation measurement

Samples of stationary particles consisting of polystyrene spheres (Polysciences, Warrington, PA, diameter = 0.465 μm or 0.494 μm) and fixed E. coli bacteria were used in this study to demonstrate the feasibility of quantifying particle asymmetry with the DMD-based optical scatter imaging setup. The 0.494 μm microspheres are labeled with three different fluorescent dyes with excitation maxima of 377, 517 and 588nm, and emission maxima of 479, 546 and 612nm, respectively.

E. coli were first fixed with 2% paraformaldehyde for 15 minuites followed by three washes in phosphate buffered saline (PBS) and stored in water at 4°C. Spheres and E.coli were either used alone or mixed together and were embedded in 2.5% acrylamide gel. The final concentration of E. coli in acrylamide was around 6.5×10^8 cells/mL, and the final concentration of spheres corresponded to a scattering coefficient, μ_s, = 0.0025 μm^{-1}. A 3μL aliquot was placed between a microscope slide and a 22mm x 22mm coverslip and allowed to gel thus immobilizing the particles within the sample. The

thickness of the gel was 5.2 μm. Samples were prepared at very low concentration so that particles were separated from each other and individual particles could be observed.

5.2.2.2 Spheres sample for size measurement

Polystyrene spheres with diameter 0.356, 0.465, 0.494, 0.771, 1.53, 1.826 μm were either immobilized in polyacrylamide gel as describe in the previous section or prepared in aqueous suspensions. The sphere samples suspended in water were 75 μm thick and placed between a microscope slide and a 22mm × 22mm coverslip and had scattering coefficient $\mu_s \sim 0.01 \mu m^{-1}$.

5.2.2.3 Living cells experiments

Immortalized baby mouse kidney (iBMK) cells were maintained in Dulbecco's modified Eagle's medium (DMEM) supplemented with 10% (V:V) fetal bovine serum (FBS), 100 Units/ml penicillin, and 100 μg/ml streptomycin. FBS was from Gemini Bio-Products, DMEM, penicillin, streptomycin were from Invitrogen. iBMK cells were kept in culture at 38°C in an 8.5% CO2 in air atmosphere. 24 hours before imaging, the cells were cultured on glass coverslips to allow attachment. Before transfer to the microscope stage, the cells were incubated for 30 minutes in growth medium supplemented with 50nM Mitotracker Green (Invitrogen) to visualize specifically the mitochondria. Coverslips were then mounted on a steel plate and the growth medium was replaced with Leibovitz's L-15 medium (Invitrogen) supplemented with 10% FBS, 100 Units/ml penicillin, and 100 μg/ml streptomycin.

5.2.2.4 Ellipse fit to measured Gabor filters responses

To discriminate particles based on their roundness using optical Gabor-like filters, an optical Gabor-like orientation dependent filter bank consisting of 18 filters was generated. For each sample, this filter bank was used to generate 18 filtered images. At each pixel, 18 intensity responses to the 18 rotations of the optical Gabor-like filters could be plotted on a polar plot, where the radial position 'ρ' indicates the magnitude of the intensity response and the angle 'ϕ' indicates the orientation of Gabor filter (Figure 5-1). In this study, we considered only the center point of each particle. To get the center points, we first segmented the particles by setting an intensity threshold using Otsu's method[91]. A few out of focus objects which appeared dimmer than those that were segmented were not analyzed. With this segmentation setting, we disregarded particles that were very out of focus. Each segment was then shrunken to contain only its center pixel by an image eroding method[92, 93]. The responses at the center points of each particle could be fitted to an ellipse model to assess whether a particle is circular or ellipsoidal. We fitted the responses to the ellipse function "$x^2 + Bxy + Cy^2 - D = 0$" using a nonlinear least-squares method (MATLAB 'lsqnonlin' function). The fitting returned coefficients B, C, D and the residuals of the fit. Using coefficients B, C, D, we obtained the rotation angle θ and semi-axes lengths of the fitted ellipse:

$$\text{Rotation}: \theta = -\frac{1}{2}\cot^{-1}(\frac{C-1}{B})$$

$$\text{Semi-axes lengths}:$$

$$a = \sqrt{\frac{2D}{\left[\sqrt{(C-1)^2 + B^2} - (C+1)\right]}}$$

$$b = \sqrt{\frac{2D}{\left[-\sqrt{(C-1)^2 + B^2} - (C+1)\right]}}$$

5.3 Results

5.3.1 Sensitivity of Gabor filtering to object aspect ratio

To evaluate the sensitivity of our DMD-based OSI system to object shape, we implemented a Gabor-like filter bank as described in the methods section. The filters were centered at ~0.803 cycles/μm and spanned orientations $0° \leq \theta < 180°$. Optically filtered images of spheres and bacteria were collected and analyzed pixel by pixel for their intensity as a function of filter orientation. Figure 5-1 A-C shows representative dark field images of the objects (E. coli or 0.465μm sphere), and the corresponding polar plots of filter intensity response as a function of filter orientation. The polar plots are shown for a pixel located at the center of the object, although the response plot was similar for all pixels within the object (data not shown). By switching the focal length of
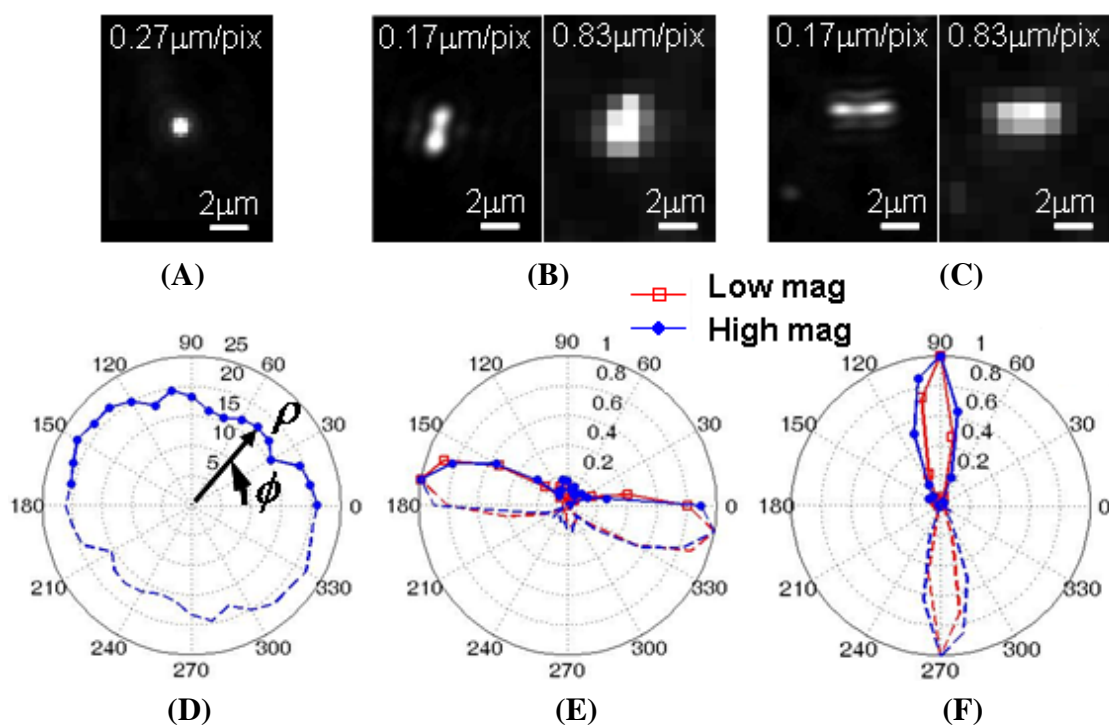
Figure 5-1 Dark field images of (A) 0.465μm sphere, and (B), (C) E. coli and high and low magnification. Corresponding intensity response, ρ, of a pixel located at the center of the object as a function of Gabor filter orientation, ϕ, for (D) the sphere and (E) & (F) the E. coli. In (E) and (F) the responses were normalized to the maximum intensity.

lens L4 (Figure 3-1) from 250mm to 50mm, we acquired filtered images at ~0.168μm/pixel and ~0.83μm/pixel respectively, for the E. coli (Figure 5-1 B and C). The pixel intensity response for the sphere varied little as a function of Gabor filter orientation (Figure 5-1D). In contrast, for the E. coli, a maximum response significantly above the average of the responses was obtained at an angle perpendicular to the orientation of the object (Figure 5-1 E and F, filled blue circles). Since the signal was filtered in the Fourier plane, the measurements were not affected by the resolution of the images. Thus, even at low magnification, when the shape of an E. coli could not be observed from the image itself, the response plot could still retrieve the same scattering pattern with similar result as for high resolution (Figure 5-1 E and F, compare red squares with blue circles)

To assess the potential of this method to differentiate a large number of particles, we analyzed the filtered responses of 66 spheres and 60 E. coli. We defined "aspect ratio" as the maximum filtered intensity response over the average of the 18 responses. Figure 5-2A, left panel, shows a representative dark field image of a mixture of spheres (D = 498μm) and E. coli. In the mixture, we used fluorescent spheres to distinguish them from
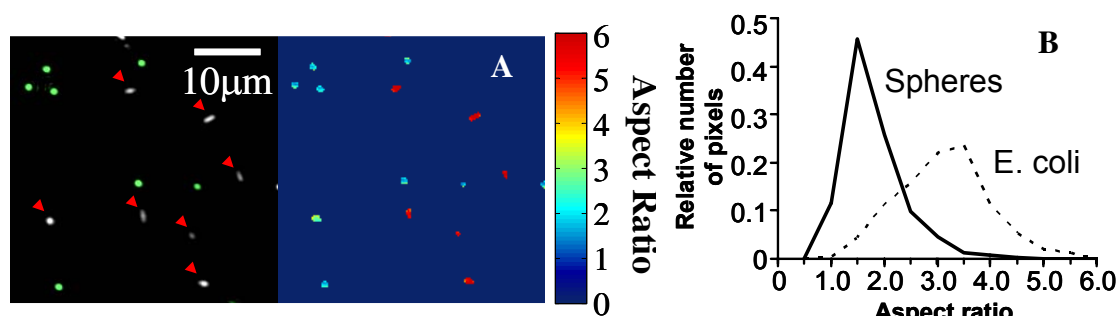
Figure 5-2 (A) Left panel: representative dark-field image showing the location of the fluorescent spheres (green) and unstained bacteria (red arrowheads). Right panel: color coded image of the bacteria-sphere mixture. The color scale corresponds to the aspect ratio parameter taken as the ratio of maximum intensity to average intensity response. (B) Aspect ratio distributions for the 66 spheres and 60 E. coli tested.

E.coli. The background was removed by setting an intensity threshold based on the dark field image, and the aspect ratio of the response was calculated for each remaining pixel. A color-coded image directly encoding aspect ratio is shown in Figure 5-2A right panel. In Figure 5-2B the "aspect ratio" distribution is shown for all the spheres and bacteria tested. The histogram of spheres has a sharp peak at aspect ratio ~1.5 and the histogram of E. coli has aspect ratio between 2 to 10 due to their varied length and rotation with respect to the optical axis. A student t-test yielded a p value <<0.001 indicating that the histograms are significantly different.

5.3.2   Feasibility of collecting Gabor filtered data within living cells

The two distinct distributions of aspect ratio parameter for the spheres and E. coli
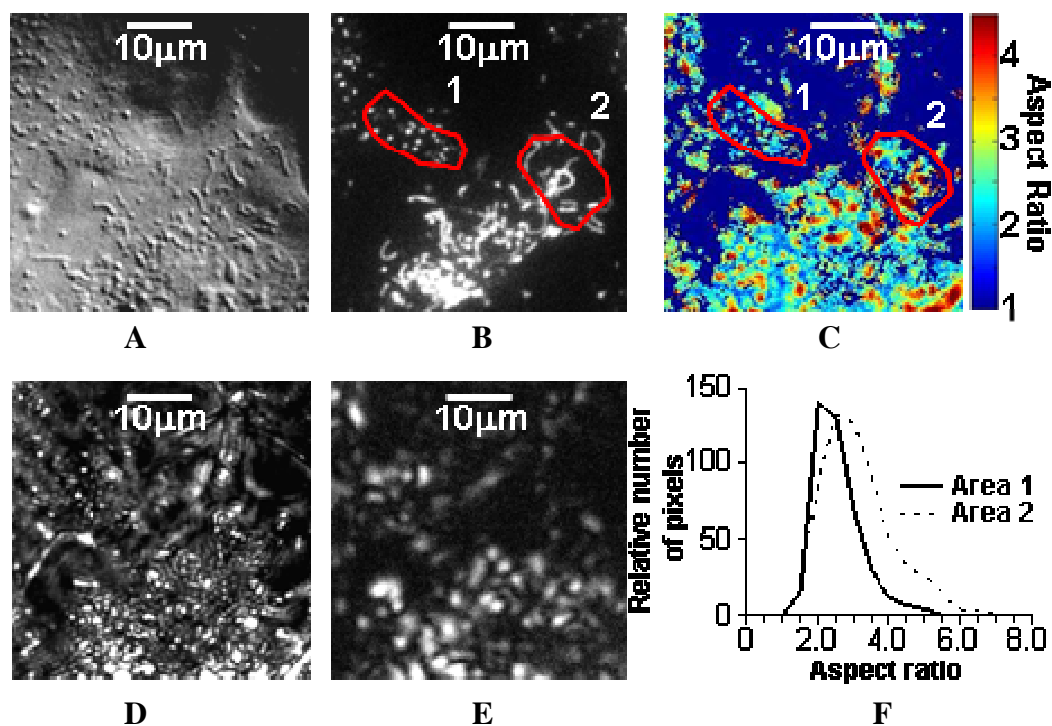
Figure 5-3 Images of iBMK cells: (A) DIC. (B) Mitotracker Green fluorescence to visualize specifically the mitochondria. (C) Color coded image encoding aspect ratio of scattering response at each pixel. The aspect ratio was measured as maximum/average intensity of filtered responses. (D) Dark field. (E) Representative Gabor filtered image. (F) Aspect ratio distribution for the pixels in Area 1 and Area 2. The two segmented areas include round and punctate mitochondria (Area 1) or tubular mitochondria (Area 2). Pixel numbers were normalized to the total number of pixels within each area.

indicate the feasibility of applying this technique on discriminating particles based on their roundness. To evaluate the feasibility of using the DMD-based setup to measure subcellular morphology, we applied the same orientation dependent Gabor filter bank on living iBMK cells. Figure 5-3A shows differential interference contrast (DIC) of two cells. At each pixel, we collected 18 intensity responses for each of the filter orientation as for the sphere and bacteria data set discussed above. Object aspect ratio was again measured by taking the ratio of maximum to average filter response. A threshold was used to remove background pixels for which the average filter response was less than 4000 counts. Figure 5-3 D and E show the dark-field image, and an example of Gabor filtered image. A color image encoding the value of the measured aspect ratio parameter is shown in Figure 5-3C. These data suggest that sufficient signal may be collected from living cells to perform the Gabor based optical filtering. One of the advantages of the optical scatter imaging method in contrast with non-imaging spectroscopy is that the scattering signal can be localized to specific regions within the cells. Thus one can quantify subcellular morphology in situ and correlate the morphological information with biochemical data obtained by fluorescence. To demonstrate this possibility, the cells were labeled with mitotracker green, and we segmented two areas, one in which mitochondria are mostly round and punctate in appearance (Area 1), and the other containing mostly tubular mitochondria (Area 2). Note that the broadband fluorescent emission was collected on a different microscope port and camera to avoid reflection and chromatic aberration at the DMD. Pixel histograms based on the measurement of the "aspect ratio" parameter are shown in Figure 5-3F for the two areas. The histograms were normalized to the total number of pixels. Area 1, which has mostly round punctate mitochondria, has more pixels with aspect ratio less than 2; and area 2, which has mostly tubular

mitochondria, has more pixels with aspect ratio higher than 3. Using the student t-test, we found the two areas to be significantly different with p-value << 0.001 indicating the potential for distinguishing different subcellular morphologies.

5.3.3 *Particle discrimination based on roundness*

In the previous section (5.3.1) we have shown that the spheres and E. coli have two distinct populations of aspect ratio, which was defined as maximum over mean response. However, the overlap between the two populations makes it difficult to completely discriminate the particles. Thereafter, we tried to better estimate the aspect ratio by fitting the responses to an ellipse function to get an estimate of the local particle's aspect ratio, and orientation of the response. The orientation and aspect ratio of this ellipse model are directly related to the orientation and aspect ratio of the objects. In particular, the intensity response as a function of angles for spheres are not expected to vary greatly and should give an aspect ratio close to one for the fitted ellipse, while elongated objects are expected to result in ellipsoidal fits with larger aspect ratios. It is also important to note that the Gabor filter response for elongated objects will give a maximum response at angles that are perpendicular to the long axis of the particle. Thus the orientation of the fitted ellipse is rotated by 90° with respect to the actual object orientation in the sample.

Figure 5-4 and Figure 5-5 show the intensity responses (blue dots) and their ellipsoidal fitting (red lines) for the spheres (Figure 5-4) and E. coli (Figure 5-5). Figure 5-6 shows the aspect ratio distributions for the spheres and E. coli calculated based on the results of the fits shown in Figure 5-4 and Figure 5-5. The histogram of the spheres has a sharper peak at aspect ratio ~1.5 compared with the previous results (Figure 5-2B); however, using the aspect ratio alone still cannot completely sort the spheres and E coli apart.
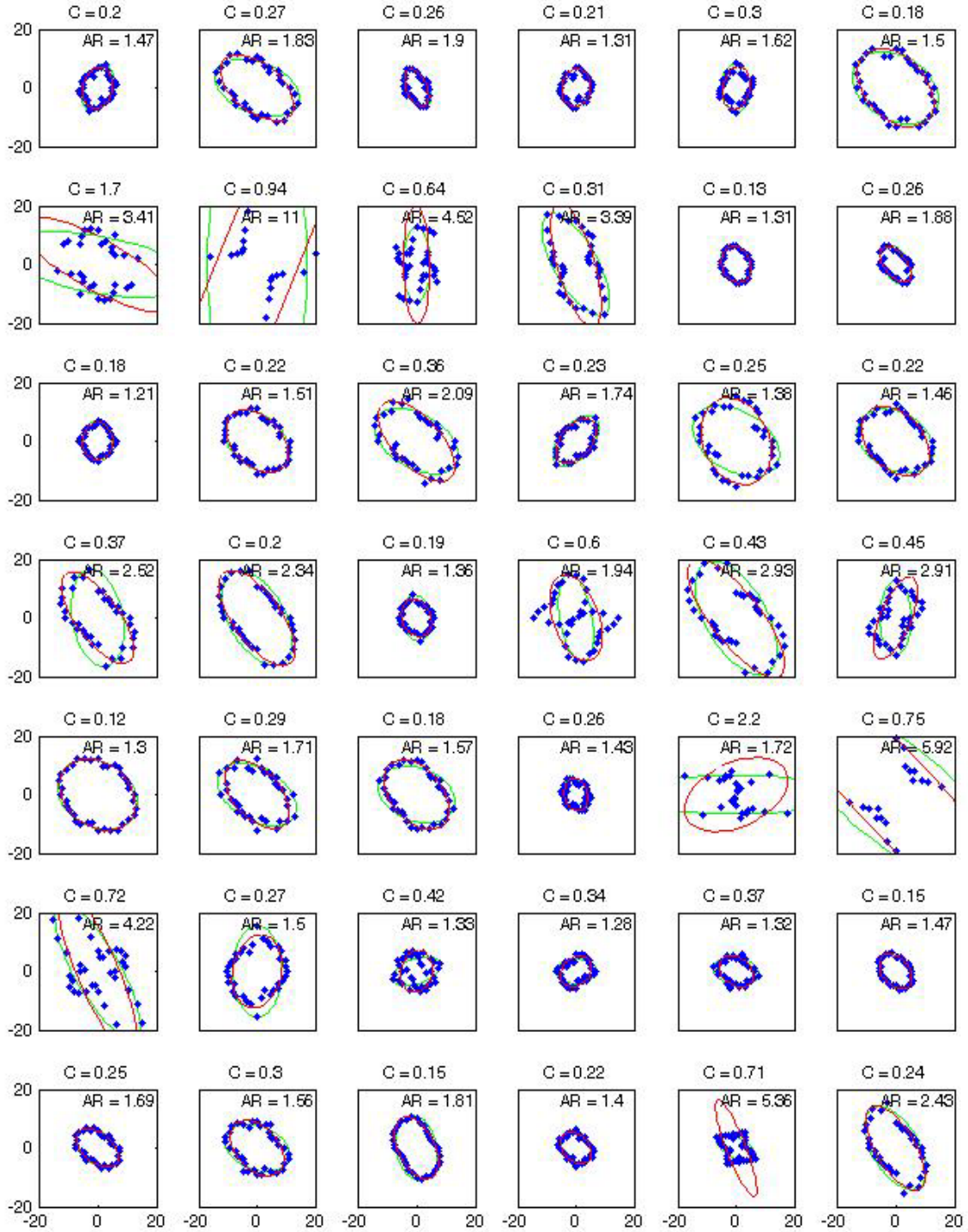
Figure 5-4 Intensity responses (blue dots) and their ellipsoidal fitting (red lines) of spheres in Figure 5-7. The green line is the initial guess of the ellipse setting the maximum response as the major axis, the average of the minimum and mean responses as minor axis, and the filter rotation giving maximum response as the orientation. C = [standard deviation of the residuals/short axis]^2 and AR = aspect ratio of fitted ellipse.
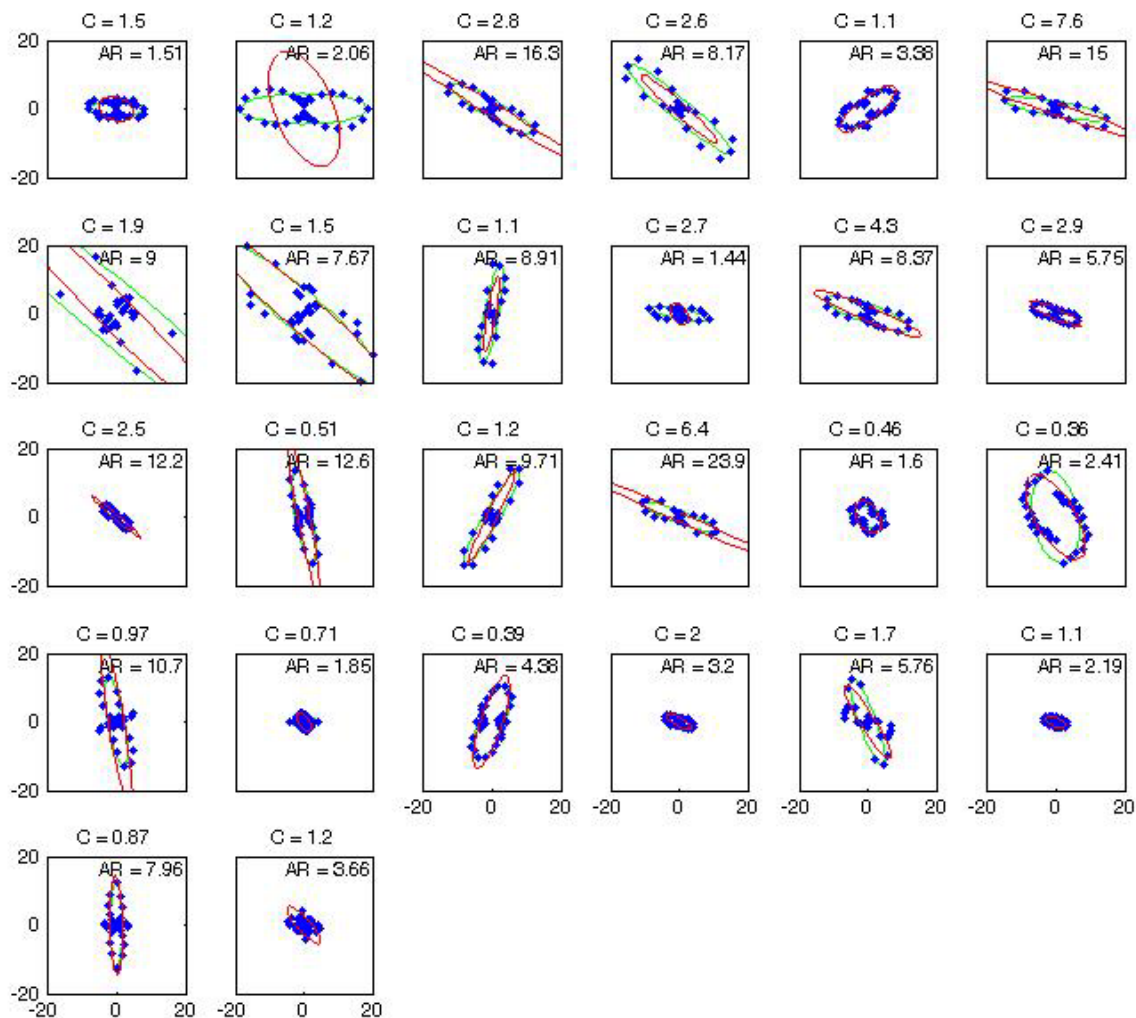
Figure 5-5 Intensity responses (blue dots) and their ellipsoidal fitting (red lines) of Ecoli in Figure 5-7. The green line is the initial guess of the ellipse setting the maximum response as the major axis, average of minimum and mean responses as minor axis, and the filter rotation giving maximum response as the orientation. C = [standard deviation of the residuals/short axis]^2 and AR = aspect ratio of fitted ellipse.

Therefore, a sorting criterion other than aspect ratio would be required. An E. coli is not exactly ellipsoidal, neither are its intensity responses (Figure 5-5), while the ellipse model is a better fit to spheres responses. Hence, for a response that gave a better fit to the ellipse model and whose aspect ratio of response was smaller than 3.5, we defined the corresponding particle as a sphere. We set the criteria for better fitting as "the square of

standard deviation of the residuals normalized to the short axis of the fitted ellipse must be smaller than 1". The criteria were chosen for they provided the best result. The rest of the objects that were not defined as spherical were then considered as elongated objects (i.e. E. coli) and the ellipse fit was only used to find their orientations.
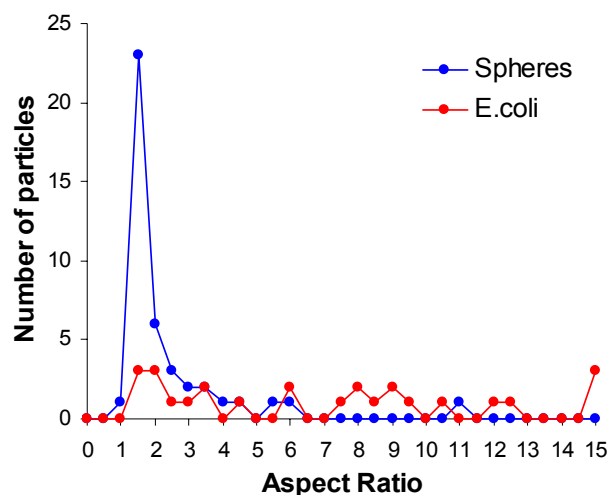
Figure 5-6 Pixel histograms of aspect ratio obtained from the ellipses that were fitted to the filter responses of the spheres and E. coli.

For the objects that were measured as spheres, we drew a circle around the center point. For those that were considered E. coli, we drew a line tilted at the measured object orientation (Figure 5-7B); this preferred orientation is defined as the angle perpendicular to the orientation of the fitted ellipse. Note that the size of the circles and lines in Figure 5-7B does not represent their actual size. With this filter bank and choice of criteria, pooling all 0.494μm spheres (n=66) and all e-coli (n= 60) tested, we measured 93% of the spheres as spherical particles and 84.6% of the E coli as elongated particles. The 3 falsely labeled spheres (pink circles in Figure 5-7) did not actually appear circular in the image. This may due to the fact that these spheres are not quite in focus. Since the gel is 5.2μm thick and the spheres are only 0.494 μm in diameter, not all the spheres will be in the same focal plane. While 4 of the total 27 E. coli were measured as spheres in Figure 5-7B, 3 of them appeared circular in the image (yellow circles in Figure 5-7) potentially due to their being oriented along the optical axis. As for finding orientations of the E. coli, 87% of the correctly labeled E. coli were found to have the correct orientation

(measured directly from the dark field images) with less than 5° error, and the remaining

13% with less than 15° error.
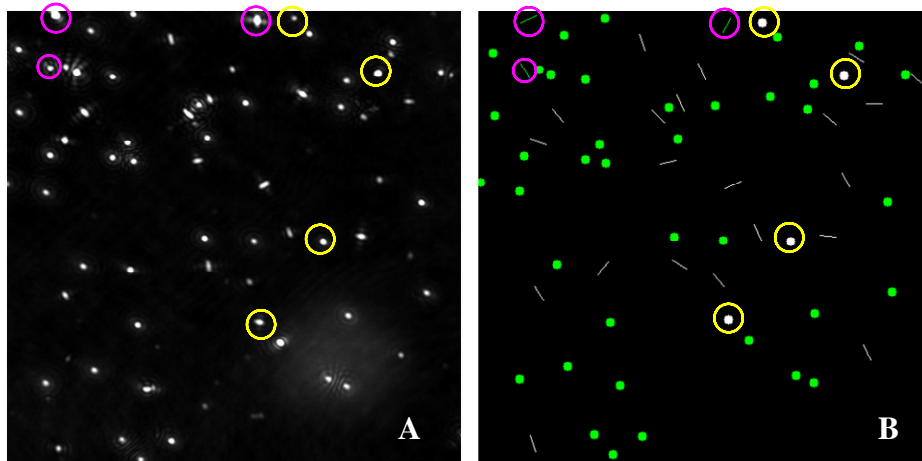
Figure 5-7 (A) Dark field image of mixture of fluorescent spheres (0.494 μm) and E. coli. The pinks circles show examples of spheres, which did not appear circular. The yellow circles are examples of an E. coli appearing circular. (B) Particles are labeled based on their roundness. Circles indicate particles without preferred orientation; lines are rotated according to the measured particles' orientation. Particles labeled green are the fluorescent spheres; particles labeled white are not fluorescent (i.e. E. coli).

5.3.4   *Relative particle sizing using the Gabor filter bank*

Monodispersed polystyrene spheres (diameter spanning 0.3 to 1.8 μm) either

embedded in polyacrylamide gel or suspended in water were used as standards to

evaluate the ability of the optical Gabor-like size dependent filter bank to discriminate

between particles of different size. This size dependent filter bank resulting generating 36

filtered images for each sample. For suspended spheres, we averaged the pixel intensities

of each entire filtered image. For stationary spheres, we considered only the center point

of each spheres with the segmentation and eroding method described earlier (section

5.2.2.4). For each sphere, we took the intensity of the center pixel to represent the

intensity response to the corresponding filter. We then plotted intensity responses as a

function of Gabor filter spatial frequencies. A Gaussian was fit to the responses (>0.90

correlation) to find the Gabor filter spatial frequencies that gave the maximal intensity. Figure 5-8A shows an example of intensity responses for the sphere suspensions and the Gaussian fit to these responses. The relative particle numbers vs. Gabor spatial frequency giving maximum response for each stationary sphere size are shown in the histograms in Figure 5-8B. The mean +/- standard deviation of center frequencies giving maximum responses of suspended and stationary spheres is plotted vs. sphere size in
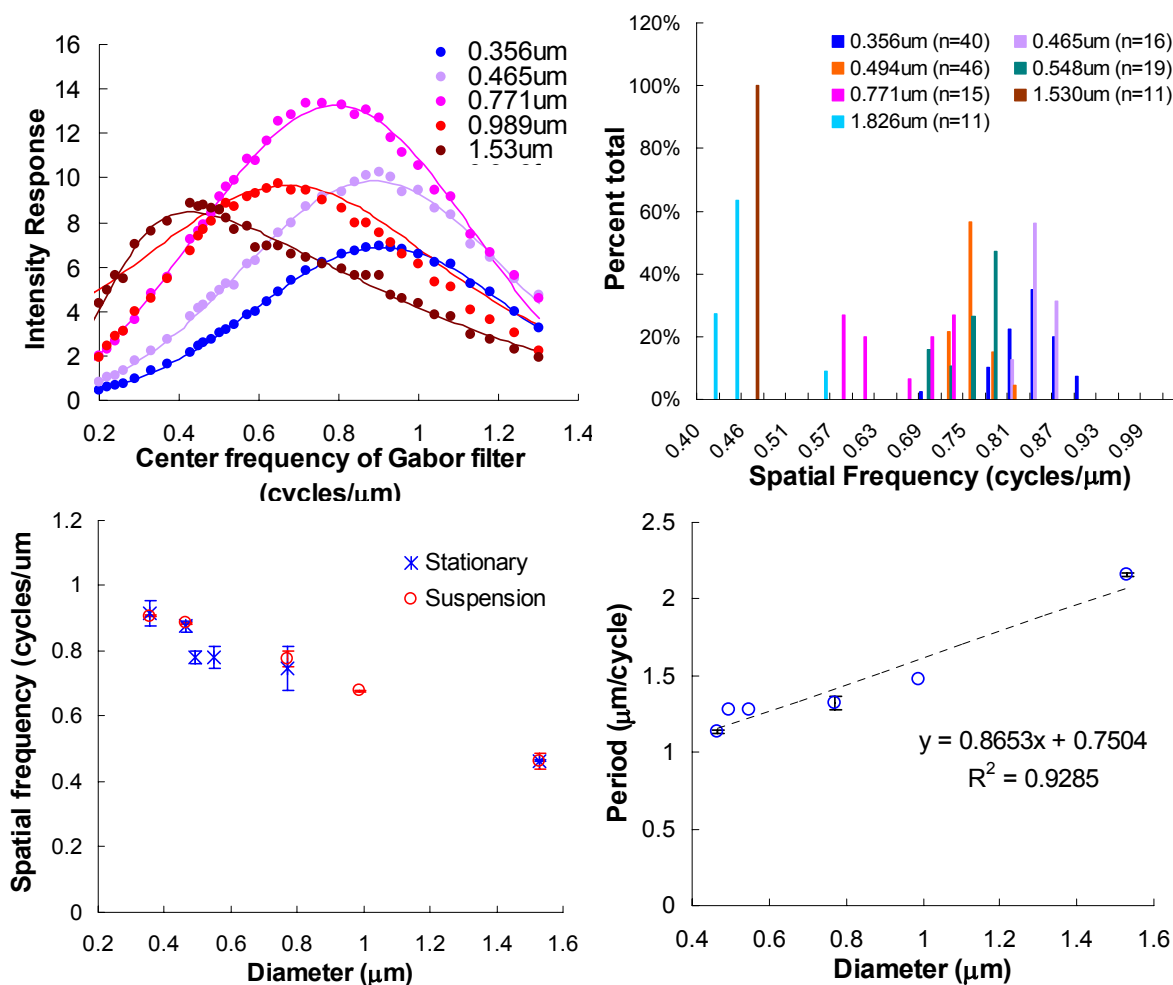
Figure 5-8 (A) Examples of intensity responses for spheres as a function of various optical Gabor-like filter frequency. Data shown are from suspensions of spheres. (B) Histogram of stationary spheres showing the relative number of particles vs. Gabor spatial frequency giving maximum intensity response at each sphere diameter. (C) Mean spatial frequency +/- standard deviation of the Gabor filter frequency giving maximum response for each sphere size for stationary (blue star) or suspension spheres (red circles). (D) Combined data of stationary and suspension spheres from (C). Spatial frequency was converted to period and the dashed line shows the linear trendline. The function of the trendline and R-squared value are displayed on the chart.

Figure 5-8C. We obtained reproducible results for the spheres either embedded in polyacrylamide gel or suspended in water. Therefore, we combined the results for both suspension and stationary spheres and converted the spatial frequency to period (Figure 5-8D). A linear function was fit to the data and could be used as a calibration curve to predict the size of unknown particles.

We also evaluated the ability of Gabor filters to discriminate particles based on size in a mixture of 0.465 μm and 0.494μm spheres and E. coli (Figure 5-9). The histograms of 0.465 μm and 0.494μm spheres were centered at 0.83 cycles/μm and 0.78 cycles/μm, respectively. The E-coli histogram had a large sharp peak at 0.66 cycles/mm and a smaller peak at 0.97 cycles/mm that could be clearly distinguished from the spheres histograms despite the fact that the E-coli width is ~0.5μm. Thus interestingly, though we disregarded the orientation of the E. coli in this analysis, the elongated shape of the E-coli likely contributed to shifting their histograms to a lower spatial frequency (main peak at 0.66 cycles/μm) allowing us to distinguish them from the spheres. The smaller peak at 0.97 cycles/μm is likely due to shorter E. coli.
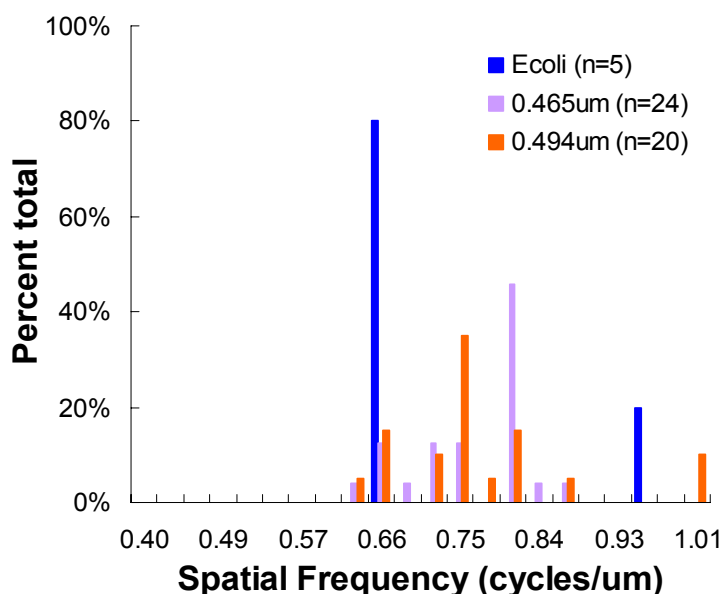
Figure 5-9 Histogram of spatial frequency corresponding to maximum intensity response for mixture of 0.465 μm and 0.494μm spheres, and E. coli.

5.4 Discussion

In this study, we used optical Gabor-like filters with various orientations to look for scatter anisotropies with respect to the azimuthal angle of scatter, ϕ (Figure 3-1). Here, we accomplished optical Gabor-like filtering by implementing Gabor filters, which are Gaussian shape bandpass filters in the Fourier domain[90], on to the DMD. Since the DMD can only generate binary images, we approximated the Gaussian by a stack of concentric discs and modulated the intensity of the scattering. We could better perform the Gabor filtering by using other kind of spatial light modulators; for example, a LCD microdisplay could generate gray-scale images and modulate the light in both intensity and phase. Since OSI manipulates the scattering signal directly in a conjugate Fourier plane, our measurement is not affected by image resolution. In particular using E. coli as a model sample, we showed that our method could retrieve the pattern of filtered responses in both high and low resolution conditions. Even when the image is too blurred to distinguish the detailed morphology of the E. coli, the shape of the intensity response could still be retrieved. Digital analysis relies greatly on the quality/resolution of the images, while our method relies on the resolution of the spatial filters and does not require high-resolution images. With a less stringent requirement on image resolution, we could perform our measurement at low resolution, increase the field of view to allow us to image more samples at once, and achieve high throughput measurement; this is an advantage of our technique over digital analysis.

To evaluate the ability of the optical Gabor filters to sort particles based on their shape and orientation, we used a mixture of spheres and paraformaldehyde fixed E coli as the model sample. The size of an E. coli is about 0.5μm ×1-3μm, which is roughly the size of a mitochondrion and makes E. coli a good candidate as an elongated object whose

size models mitochondria, which are involved in many biological functions. We used fluorescent spheres in the spheres/E. coli mixture to establish a priori knowledge about the identity of the particles. The orientation dependent filter bank was then used to get the intensity responses as a function of filter orientation. We were able to obtain two populations of particles with distinct aspect ratio values showing the feasibility of applying the Gabor based technique for discrimination of particles based on their roundness. The aspect ratio values were obtained by measuring the aspect ratio of the scattering pattern, which is related to the aspect ratio of the scattering particle. To get the actual aspect ratio of a particle, we could model responses or experimentally calibrate the data with particle standards. However, non-spherical standards are hard to assess. Though at present we could not know the particle's absolute dimension, for biological applications, and considering variations between biological samples, the relative morphological changes may have more meaning than obtaining absolute dimension. In this study, we used simple model samples consisting of round (spheres) vs. elongated (E. coli) particles, it is possible to extend the application to study more complex morphologies.

We also demonstrated feasibility of acquiring the filtered data from two subcellular regions containing punctate or tubular mitochondria, respectively. Our filtered data could differentiate the two regions based on the aspect ratio parameter measured at each pixel, and resulted in a lower aspect ratio measurement in the region with round mitochondria as expected. This is likely due to the fact that mitochondria are responsible for a large part of the scattering signal in the cytoplasm[94]. In this study, we labeled mitochondria with Mitotracker Green; however, the maker is only used to visualize the morphology of mitochondria and is not inherently required for our method. While labeling or staining is

specific for certain targets, our method is sensitive to overall particle morphology. Since our method records morphological information in situ, morphological measurements obtained by optical scatter imaging could be registered pixel by pixel with fluorescence microscopy data to establish the direct link between the measured elastic scattering parameters and specific organelles. Due to the present speed of acquisition (two minutes for the orientation dependent filter bank) and movement of the organelles during this time, pixel-by-pixel registration between OSI and fluorescent mitochondria was not possible in this study. Data acquisition speed will be readily improved by fully automating the setup and increasing signal (e.g. by increasing the power of the laser source).

Though we obtained two populations of particles with distinct aspect ratio values for the spheres and E. coli, the overlap between their aspect ratio parameter distributions make it difficult to separate the two particles based solely on aspect ratio. Hence, we fitted an ellipse function to the responses to facilitate sorting the spheres and E. coli. Since the ellipse function fitted better to the intensity responses for a sphere, we first defined particles as spherical by finding those that gave a better ellipsoidal fit. The remaining non-spherical particles were then considered as elongated particles or E. coli. The current method gave 93% and 84.6% accuracy on finding spheres and E. coli, respectively.

It is likely that the sorting failed on particles that were out of focus and hence gave rise aberration in the Fourier plane; in addition, elongated particles aligned along optical axis may have spherical responses. Those are the limitations of our current method that the objects must be in the depth of field and we are not yet about to perform 3-D imaging. Figure 5-10 shows examples of the intensity responses of the same sphere when it is in or

out of focus. When the sphere is in focus (Figure 5-10A) the aspect ratio of its intensity response is close to one (1.17), while when the sphere is gradually out of focus (Figure
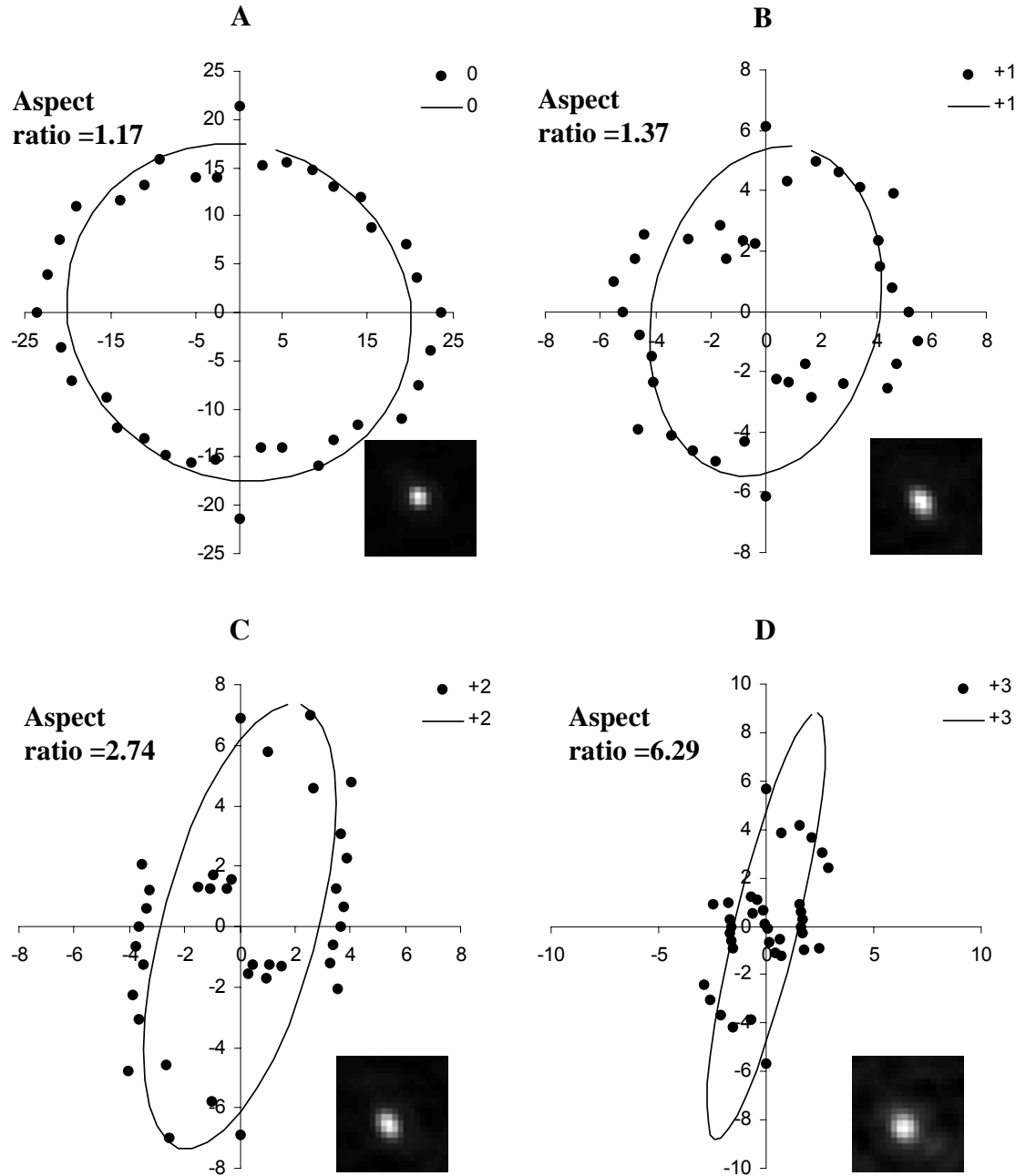
Figure 5-10 The intensity responses (circles) and ellipse fits (lines) of a sphere in or out of focus, the aspect ratio of the response getting from the fit is also indicated in the figure. The intersects show the dark field images of the sphere. (A) The sphere is in focus, 0 indicates that the sphere is in focus. (B), (C), (D) show the same sphere gradually out of focus. +1, +2, +3 indicate the objective 1, 2 or 3 steps out of focus and away from the sphere.

5-10B-D), the intensity responses become non-circular and the aspect ratio increases. The thickness of the sample is around 5 μm; hence not all the spheres are in the focal plane some maybe slightly out of focus. This is likely the reason that the spheres have aspect ratio peaked at around 1.4 instead of 1.0 in the histograms (Figure 5-2 and Figure 5-6).

This effect may underlie an aberration due to uncollimated scattered light from particles that are not in the focal plane or misalignment of the optics upstream of the DMD. Further investigation is required to better understand the focusing effects and to minimize the aberration so that we could get better estimate of the aspect ratio of a particle.

In addition to sorting particles based on roundness, the optical Gabor filters were used for sizing particles using a Gabor filter bank consisting of filters with various
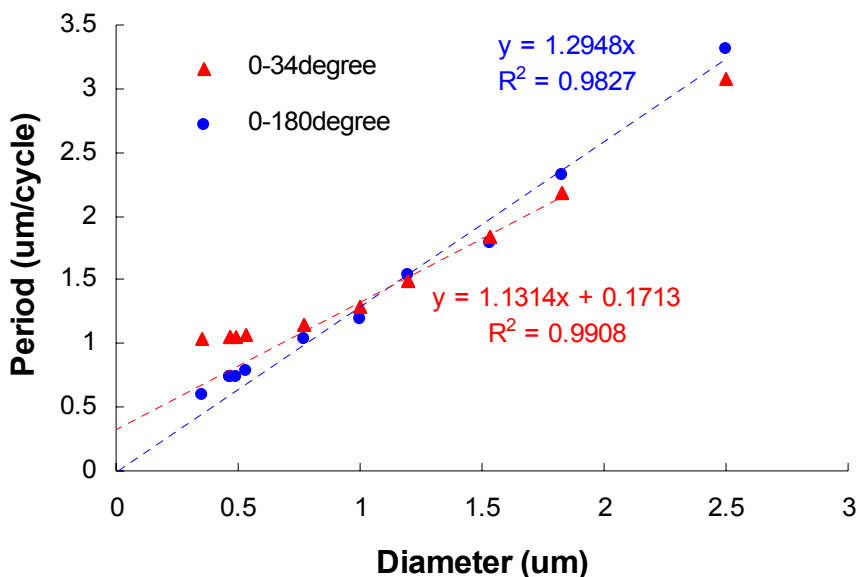
Figure 5-11 Simulation of Gabor filter period giving maximum response for different sphere sizes with index ratio, m=1.2. Scattering intensities of spheres were getting from Mie theory, the scattering intensity was then convoluted with a Gabor size sensitive filter bank to get intensity response. Blue circles: simulation considered scattering intensity up to 180°. Red triangles: simulation considered scattering intensity up to 34° which is about the NA of the 20x objective.

frequencies and finding the filter frequency giving the maximum intensity response. We were able to discriminate particles that differ in size by 100nm and for the diameter >0.45μm. Theoretically, the Gabor filter period giving maximum response as a function of sphere size should have linear response and has no intercept; however, our experimental data has linear response but has an intercept (Figure 5-8). This is likely due to the cut off of the NA of the 20x objective, which collects scattering up to about 34.32°. Simulation results (Figure 5-11) show the response is linear and has no intercept, if we collect scattering up to 180°. While when the scattering is cut off at 34°, the response is saturated for small particles; as for bigger size sphere, the response is linear but has an intercept. (Please note that the simulation here just a rough calculation and only shows the trend when collecting different scattering angles, the number can not represent the actual situation.) In our results, 0.356μm was below the system's resolution and could not be resolved. Thus, in our current setup with a 20x objective, filters with maximum response for objects < 0.45μm will give a maximum filter response, which will fall outside of the objective's NA (=0.75). To discriminate particles with diameter < 0.45μm using the present filter response analysis will require a higher NA (e.g. 63x, NA=1.4). Nonetheless, instead of finding the maximum response filter, one could analyze the shape of the full filter response rather than only the location of the maximum and estimate the size of unknown objects based on their full response to the filter bank. Our present system could measure relative size but not actual size. To find the actual size of a particle with great accuracy we would need to know its scattering pattern to predict its Gabor filter response. For example for spheres, the absolute size may be obtained by predicting the Gabor filter responses based on Mie theory. One could also use

experimental calibration using particle standards if similar particles are to be used in the samples of unknown size.

For quantifying particles spanning a larger size range or for obtaining higher resolution, a larger filter bank could ultimately be used to cover all the desired sizes and orientations. While the size of the filter bank depends on the range of sizes to be analyzed and desired resolution and could consist of over a hundred filters, these filtered images could still be acquired in seconds provided that the system allows for high light throughput and fast single image acquisition on the order of tens of milliseconds.

We adopted the concept of Gabor filtering and generated optical filter banks consisting of Gabor-like filters with various rotations or scales implemented on the DMD. Combining optical scatter imaging with Gabor filtering, we would be able to perform high throughput measurement without sacrificing morphological information. The application of optical Gabor-like filtering could be extended to perform particle sorting based on their morphology or size. Furthermore, our technique could distinguish regions with different mitochondrial morphology in living cells, and ultimately could be applied in a biological study to measure organelles' morphological change without fluorescence staining. For example, with further analysis and computational training (e.g. machine learning methods) to distinguish elongated mitochondria from background and from spherical organelles, we may be able to quantify dynamic changes in mitochondrial morphology such as mitochondria fission during apoptosis. Using a spatial light modulator as a spatial filter generator allows us to filter light at any combination of spatial frequencies, hence the application is not limited to Gabor filtering; any desired filtering scheme could be implemented on the spatial light modulator and be used in our optical scattering imaging system.

Chapter 6 Summary and Future Direction

Using circular high- and low- NA filters, we measured the scattering properties, in terms of OSIR, of cells expressing Bcl-x_L and Bcl-x_L mutants. We reported that the C-terminal transmembrane domain of Bcl-x_L mediates morphological changes in mitochondria and that the TM domain alone is sufficient to elicit the changes. Using electron microscopy, we found that the Bcl-x_L TM domain induced OSIR decrease was coincident with an increase in the proportion of mitochondria with an expanded matrix[1]. Further investigation using the YFP variant as control, we found that Bcl-x_L-ΔTM, which does not localize on mitochondria, also induced OSIR decrease but did not alter mitochondrial matrix morphology. Under normal condition, Bak localizes on mitochondria, while Bax is localized in the cytoplasm. Upon apoptotic stimulation, Bax undergoes conformation changes, which allows Bax to form homodimers or oligomers, and relocate to the mitochondrial outer membrane[95, 96]. Without the C-terminal transmembrane domain, Bcl-x_L-ΔTM also resides in the cytoplasm. However, the C-terminal domain of Bcl-x_L is required to mediate Bcl-x_L/Bax heterodimer formation [97]. Our measurements with iBMK W2 and D3 cells suggest that the presence of Bax and Bak does not affect the action of the Bcl-x_L-ΔTM induced scattering property alteration, while the effect of TM requires the interaction with Bax or Bak. However, from the OSIR values measured with the DMD-based system were lower than expected. Thus, the results of the D3 cells remain inconclusive. The lower OSIR value measured with the DMD-based OSI system is likely due to insufficient signal from cell samples, because 98% of laser light was lost passing the spinning diffuser and result in low signal-to noise ratio. On the other hand, the OSIR measurement reported increased OSIR in Bax- and Bak-deficient iBMK D3 cells compared with wild-type iBMK W2 cells. This increase is 1.3

and 1.5 folds measured with initial and DMD-based OSI systems, respectively. Therefore, with the DMD-based system, though the OSIR reading is lower than expected, the relative difference still holds true. The OSIR measurements of polystyrene spheres matched Mie theory prediction. Therefore the angular scattering properties of the cells represented by OSIR can be considered equivalent to the OSIR properties of a sphere of a given size, and the OSIR can then be converted to an "equivalent scattering diameter". In this case, the OSIR decrease due to Bcl-x_L transmembrane domain corresponds to an increase of the equivalent scattering diameter and the OSIR increase in the absence of Bax and Bak corresponds to a decrease in this "equivalent scattering diameter".

Recent studies suggested that overexpression of Bcl-x_L significantly elongated mitochondria in neuronal processes[98] and produced fused mitochondria[99]. Bcl-x_L could promote mitochondrial fusion through an interaction with Mfn2 (Mitofusin2), and could also facilitate mitochondrial fission dependent on Drp1 (dynamin-related protein 1)[98-100]. It was suggested that Bcl-x_L may tip the balance in favor of fusion or fission depending on its expressing level[99]. Drp1 recycles between the cytoplasm and mitochondria with a half-time of 50s[88]. Bcl-x_L-ΔTM could interact with Drp1 and prevent it from localizing to mitochondria and reduce mitochondrial fission, which could result in longer mitochondria and lower OSIR. Therefore, the reduced OSIR could be due to the fine geometrical structure of the mitochondrial matrix, mitochondrial fusion or fission or other changes, and the simple OSIR measurement is not able to tell which the likely case is. However, the OSIR measured with simple high- and low- NA filters successfully detected the morphological changes of mitochondria which could not be observed by DIC or fluorescence images under the same image resolution. This technique does not rely on labeling and could non-invasively observed dynamic morphology in real time with

minimum sample manipulation. Though the OSIR could not tell detailed morphological differences, it could be applied for quick screening for a time point at which the morphology is changing in a time-lapse experiment, drug treatment or genetic manipulations, which trigger morphological alteration, especially when the type of change and its effect on OSIR is known.

We extended our size-sensitive optical scatter imaging (OSI) method to analyze the shape of the scattering objects by utilizing a spatial light modulator for spatial filtering. A spatial light modulator could be programmed to generate any pattern of 2-D filters and pass any combinations of angles of scattering. We choose a digital micromirror device (DMD) to filter light in a reflectance mode and also tried a liquid crystal (LC) microdisplay to perform filtering in transmission. The DMD has several advantages, including high efficiency, high contrast ratio, and high mirror actuation speed. However these advantages were offset by specific issues pertaining to the use of the DMD in a conjugate Fourier plane. In particular, the array of tilted mirrors acts as a blazed grating, which causes significant chromatic aberrations and precludes imaging samples with a broad band emission. This is particularly significant for combining scattering and fluorescence measurement through the DMD on the same microscopy port. Thus in our study, broadband fluorescent images of spheres or cells were collected on a separate camera and post-registered with the scatter images. This problem was not presented using a different spatial light modulator, such as a liquid crystal device (LCD), which does not involve tilted pixels. We also found that this 800x600 pixel LCD device did not exhibit the same edge-generated geometric aberrations that we saw with the DMD. Despite the expected high throughput and efficiency of the DMD, signal loss was still a problem due to the use of the spinning diffuser to wash out speckle when imaging with

the laser source. It is nevertheless important to note that the DMD blaze wavelength is 656nm, and using a laser source with a wavelength closer to this value could slightly improve throughput. A comparison between the throughput of the DMD-based system under our present conditions vs. that of a state-of-the-art LCD remains to be fully assessed to select the optimum spatial light modulator for this optical scatter imaging application. One remaining advantage of the DMD over an LCD is the intensity contrast ratio between off and on pixels. This intensity ratio is important in our application, where inefficient blocking of the light at the chosen spatial frequencies can result in significant background and increased noise in the filtered images. The image overlap issue appeared in both DMD and LC microdisplay system, whereas the bigger pixel sizes of the LC microdisplay worsen the overlap. We have shown preliminary data indicating that this image overlap could be eliminated by deconvoluting the images and got satisfying result by comparing signal before and after eliminating the overlapping images. More careful measurements of deconvolution effect on actual particle signal should be evaluated when applying this method on future experimental data.

Using the DMD-based OSI system, we demonstrated the ability of the optical Gabor-like filters to distinguish particles based on their size or roundness. We generated an optical Gabor-like size-sensitive filter bank, which consisted of 36 filters with three rotations and various scales/center frequencies. Each filter is sensitive to a specific particle size. Finding the Gabor filter center frequency providing maximum intensity response, we could estimate the corresponding size of the particle. We have shown sphere sizing using either OSIR or Gabor filtering. The advantage of using OSIR is that only two filters are needed while Gabor filtering requires a bank of filters. The size of filter bank depends on the desired resolution and dynamic range. Hence, Gabor filtering

is much more time consuming. When a 20x objective is used, the OSIR could resolve

0.365μm spheres while the Gabor filtering couldn't. Because the OSIR uses the

information within the whole NA while the Gabor filtering looks for the frequency giving

maximum response; when this maximum response falls outside the NA of the objective,

the size is no longer resolvable. The resolution of Gabor filtering might be improved by

comparing the whole response curve instead of only the peak of the responses. Since the

scattering pattern changes when index ratio is the different, the Gabor filter frequency

giving maximum intensity response also changes. However, the response will still be

linear but with different slope (Figure 6-1). Hence, when using Gabor filter for sizing

particles, the index ratio of the particle must be taken into account. On the other hand,

Figure 4-5 shows that the OSIR measurement is independent of index ratio, m, for

1<m<1.2; because OSIR can be considered normalized to low- NA image. In the case of

the sphere suspensions, a large amount of spheres is moving due to Brownian motion and

the signal comes from this large amount of spheres. In the case of stationary spheres, the

number of spheres is low, and the signal comes from individual spheres. Therefore, for
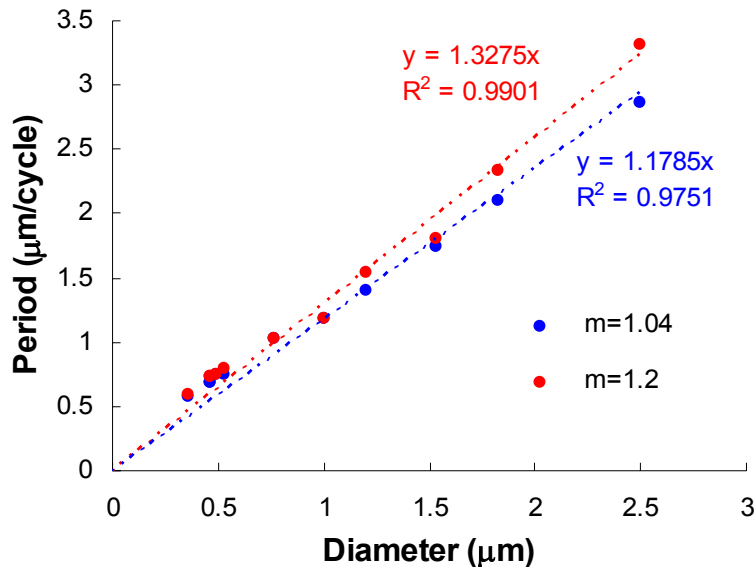
Figure 6-1 Simulation of Gabor filter period giving maximum response for different sphere sizes with index ratio, m=1.04 (blue circles) and m=1.2(red circles). Scattering intensities of spheres were obtained from Mie theory, the scattering intensity was then convoluted with a Gabor size sensitive filter bank to get intensity response.

small sphere sizes, the signal is very weak and signal-to-noise ratio is low. This is especially for the OSIR measurement, which takes the ratio of HNA to LNA images, and will result in dividing the HNA signal by very low value giving rise to an unreasonably high ratio hence the large error. When measuring cell samples, the index ratio of organelles (m~1.04) is lower than polystyrene spheres (m=1.2) and the signal is weaker, this may be why the OSIR was lower than expected in the 20x case. On the other hand, Gabor filtering is affected less by the signal-to-noise ratio and gives reasonable measurement even when the signal is weak. In addition, the Gabor filtering has a linear response, which makes it easier to predict size of unknown particle. The OSIR is only suitable for measuring the diameter of spherical particles, while the Gabor filtering can be used to measure particle size along any direction, and hence could estimate the full dimension of a particle.

We also generated an optical Gabor-like orientation dependent filter bank consisting of 18 filters with a fixed center spatial frequency and variable rotations. Each of these filters is sensitive to particles with orientation perpendicular to the rotation of the filter. We displayed the 18 intensity responses on a polar plot in which the angles represent the rotation and the magnitudes represent the intensities of the responses. We have shown that, even under low image resolution, at which the image is blurred and cannot reveal the detailed morphology of a particle, the plot of intensity responses still retrieves the shape of the filter responses. This advantage could ultimately allow us to image samples under low magnification and increase field of view to allow imaging more samples at a time. Applying the orientation dependent filter bank on iBMK W2 cells, we successfully distinguished two cellular regions with distinct populations of mitochondria with elongated and round morphology. These data suggest that sufficient signal may be

collected from living cells to perform the Gabor based optical filtering. In healthy cells, Bax or Bak is required for normal mitochondria to fuse into elongated tubules by interacting with Drp1, and the Bax/Bak double knockout (Bax/Bak) cells contain a significantly higher amount of mitochondria with fragmented morphology [2]. Our OSIR measurement reported a smaller equivalent scattering diameter in D3 cells but is not able to tell the shape difference and the optical Gabor-like filtering has the potential to further show that D3 cells contain more round features than W2 cells[87].

The resolution of the OSI system does not rely on the resolution in the image plane but on spatial frequency resolution in the Fourier plane. Magnifying the conjugate Fourier plane to fall on the whole active area of the spatial light modulator allows us to obtain the best frequency resolution. However, we could only use the center 300x300 micromirrors to avoid the geometric aberration. In this case, though the pixel size of single element of the LC microdisplay ($32 \times 32 um^2$) is bigger than a micromirror of a DMD ($13.68 \times 13.68 um^2$) and the pixel number of the LC microdisplay (800x600) is less than the DMD (1024x768); more pixels of the LC microdisplay could be utilized (600x600) and better resolution could be provided. The resolution also depends on the size of Gabor-like filter bank; the more filters in a filter bank the better the resolution, however, also the longer the time to process. Minimizing the time required to process an optical Gabor-like filter bank is especially important when studying living biological samples, in which the organelles are moving. If the position or shape of an organelle changes during the time of processing a filter bank, we will not be able to measure the correct size and shape of the organelle and will not be able to capture the time point when the change occurs. Currently, we manually actuate the DMD and acquire the images, which adds a lot more time on to the actual exposure time required for each filtered

image. We are working on automating the whole process, which will not only reduce acquisition time but will also reduce human errors. In this project we separated the orientation (18 filters) and size (36 filters) to simplify the problem and study either orientation/roundness or size. The advantage of doing optical Gabor-like filtering is to combine the two filter banks to measure the dimensions of non-spherical particles. The idea is to measure size at each filter rotation and estimate the full shape of the particles. However, the filter bank will be very large (containing 18x36 filters). Data acquisition speed will be improved by fully automating the setup and increasing signal (e.g. by increasing the power of the laser source). In digital analysis, the process speed is usually improved by parallel analyzing. Therefore, to improve the data acquisition speed, we may apply the concept and design an optical system for parallel processing. For example, we may miniaturize the system and use an array of optical processing units for each Gabor filter.

The large Gabor filter bank is very useful to gain information of dimension and shape of unknown particles. However, if the object of interest is already known, we may design filters to pick up the object. For example, if we are only interested in picking up elongated particles in certain orientation, we may design slit-like filter perpendicular to the desired orientation. We have tested the slit-like filters to pick up E. coli with certain orientations and got good results (data not shown).

The OSI technique does not rely on labeling hence minimizes sample preparation and provides general subcellular morphology in situ. If observation of a specific target is desirable, OSI could be facilitated by fluorescent labeling and performing pixel-by-pixel registration to assess the morphological information of the specific target. Optical Gabor-like filtering, although requires a huge number of filters, provides an enormous

number of parameters pertaining to the particles' scattering property. With proper computerized training processes, we might be able to classify organelles according to their scattering property and may ultimately perform pattern recognition without the aid of labeling. In addition, though Gabor filtering is affected less by image resolution, we analyze intensity response of each pixel in the image; hence if the particle is smaller than the resolution element and more than one particle may be included within the resolution element the intensity responses would be the combined response of the particles within the pixel. Because the resolution element, which is defined by the Gabor σ is typically bigger than a pixel. Using computer-training methods, we may be able to differentiate particles that are included in this pixel. In addition, different biological particles will have different time responses and these could be used to differentiate them from each other based on their different dynamics. Ultimately, we seek to apply this technique in biological study to measure organelles' dynamic morphological change without fluorescence staining.

Acknowledgment of Previous Publications

The above work was published in the following publications and presentations:

Publications
- **J.Y. Zheng**, Y.C. Tsai, P. Kadimcherla, R. Zhang, J. Shi, G.A. Oyler, N.N. Boustany, "The C-terminal transmembrane domain of Bcl-x_L mediates changes in mitochondrial morphology", Biophysical J., 94 (1): 286-297, 2008.
- R.M. Pasternack, Z. Qian, **J.Y. Zheng**, D.N. Metaxas, E. White, N. N. Boustany, "Measurement of subcellular texture by optical Gabor-like filtering with a digital micromirror device", Opt Lett., 33 (19): 2209-11, 2008.
- R. M. Pasternack, Z. Qian, **J.Y. Zheng**, D. N. Metaxas, and N. N. Boustany, "Highly sensitive size discrimination of sub-micron objects using optical Fourier processing based on two-dimensional Gabor filters", Opt. Express **17**, 12001-12012 (2009).
- **J.Y. Zheng,** R. M. Pasternack, N. N. Boustany, "Optical Scatter Imaging with a Digital Micromirror Device", Opt. Express (2009, to be published).

Oral Presentations
- **J.Y. Zheng**, Y.C. Tsai, J. Shi, G.A. Oyler, N.N. Boustany, "Transmembrane domain mediates Bcl-x_L induced changes in subcelluar particle size distributions", Presented at annual meeting of the Biophysical Society, Salt Lake City, UT, Feb. 2006.
- **J.Y. Zheng**, Z. Qian, R.M. Pasternack N.N. Boustany, "Microscopy with Spatial Filtering for Sorting Particles and Monitoring Subcellular Morphology", Presented at annual meeting of the SPIE Photonics West, San Jose, CA, Jan. 2009.

Conference proceedings
- **J.Y. Zheng**, B. Griffel, Y.C. Tsai G.A. Oyler and N.N. Boustany, "Characteristic Organelle Size Distributions within Apoptosis Resistant Cells", Presented at the BMES 2004 Annual Fall Meeting, Philadelphia, PA, Oct. 13-16, 2004.
- B. griffel, **J.Y. Zheng**, and N.N. Boustany, Fourier filtering with a Digital Micromirror Device, presented at the Annual Meeting of the Biomedical Engineering Society, Philadelphia, PA, Oct. 2004
- **J.Y. Zheng,** Y.C. Tsai, J. Shi, G.A. Oyler and N.N. Boustany, "Mitochondrial protein targeting via Bcl-x_L Transmembrane Domain alters angular light scattering", Presented at the BMES 2005 Annual Fall Meeting, Baltimore, MD, Sep 28-Oct 1, 2005.
- **J.Y. Zheng** and N. N. Boustany, "Direct measurement of particle diameter distributions in dark-field microscopy", Presented at the Optical Soc. of Am. Topical Meeting on Biomedical Optics, Fort Lauderdale, FL, Mar. 19-22, 2006.
- N.N. Boustany and **J.Y. Zheng**, "Light –scattering-based morphometric cellular response to transfection by the Bcl-xl transmembrane domain", International Society for Analytical Cytology XXIII Congress, Abstract # 373, Quebec City, Quebec, Canada, May 20-24 2006.
- N.N. Boustany and **J.Y. Zheng**, "Effect of Bcl-2 family proteins on subcellular particle size distribution", in Biomedical Applications of Light Scattering, Proceedings of the SPIE, Vol. 6446, Jan. 2007.
- R.M. Pasternack, Z. Qian, **J.Y. Zheng**, and N.N. Boustany, Measurement of subcellular morphology by light scatter filtering with a digital micromirror device, in Biomedical Applications of Light Scattering, Proceedings of the SPIE, Vol. 7187, Jan. 2009.
- N.N. Boustany, **J.Y. Zheng**, R.M. Pasternack, Z. Qian, Optical Fourier processing microscope to quantify subcelluar structure and dynamics, Proceedings of the IEEE International Conference on Complex Medical Engineering, Tempe, AZ April 9-11 2009.
- R.M. Pasternack, **J.Y Zheng**, Z. Qian, J. Zhou, D.N. Metaxas, E. White, and N.N. Boustany, Optical Processing of Cell and Tissue Structure, Workshop on Microscopic Image Analysis with Applications in Biology (MIAAB2009), NIH Campus, Bethesda, MD, Sep 3-4 2009.

References

1. J. Y. Zheng, Y. C. Tsai, P. Kadimcherla, R. Zhang, J. Shi, G. A. Oyler, and N. N. Boustany, "The C-terminal transmembrane domain of Bcl-xL mediates changes in mitochondrial morphology," Biophys J **94**, 286-297 (2008).

2. M. Karbowski, K. L. Norris, M. M. Cleland, S.-Y. Jeong, and R. J. Youle, "Role of Bax and Bak in mitochondrial morphogenesis," Nature **443**, 658-662 (2006).

3. D.-F. Suen, K. L. Norris, and R. J. Youle, "Mitochondrial dynamics and apoptosis," Genes Dev. **22**, 1577-1590 (2008).

4. N. N. Boustany, S. C. Kuo, and N. V. Thakor, "Optical scatter imaging: subcellular morphometry in situ with Fourier filtering," Opt. Lett. **Vol. 26**, 1063-1065 (2001).

5. E. Betzig, G. H. Patterson, R. Sougrat, O. W. Lindwasser, S. Olenych, J. S. Bonifacino, M. W. Davidson, J. Lippincott-Schwartz, and H. F. Hess, "Imaging Intracellular Fluorescent Proteins at Nanometer Resolution," Science **313**, 1642-1645 (2006).

6. G. Donnert, J. Keller, R. Medda, M. A. Andrei, S. O. Rizzoli, R. Lührmann, R. Jahn, C. Eggeling, and S. W. Hell, "Macromolecular-scale resolution in biological fluorescence microscopy," Proceedings of the National Academy of Sciences **103**, 11440-11445 (2006).

7. M. G. L. Gustafsson, "Nonlinear structured-illumination microscopy: Wide-field fluorescence imaging with theoretically unlimited resolution," Proceedings of the National Academy of Sciences of the United States of America **102**, 13081-13086 (2005).

8. V. Backman, V. Gopal, M. Kalashnikov, K. Badizadegan, R. Gurjar, A. Wax, I. Georgakoudi, M. Mueller, C. W. Boone, R. R. Dasari, and M. S. Feld, "Measuring cellular structure at submicrometer scale with light scattering spectroscopy," Selected Topics in Quantum Electronics, IEEE Journal of **7**, 887-893 (2001).

9. J. C. Ramella-Roman, P. R. Bargo, S. A. Prahl, and S. L. Jacques, "Evaluation of Spherical Particle Sizes With an Asymmetric Illumination Microscope," IEEE J. Sel. Top. Quantum Electron. **9**, 301-306 (2003).

10. M. T. Valentine, A. K. Popp, D. A. Weitz, and P. D. Kaplan, "Microscope-based static light-scattering instrument," Opt. Lett. **26**, 890-892 (2001).

11. J. D. Wilson, C. E. Bigelow, D. J. Calkins, and T. H. Foster, "Light scattering from intact cells reports oxidative-stress-induced mitochondrial swelling," Biophys J **88**, 2929-2938 (2005).

12. C. Xu, P. Carney, and S. Boppart, "Wavelength-dependent scattering in spectroscopic optical coherence tomography," Opt. Express **13**, 5450-5462 (2005).

13. C. Mujat, C. Greiner, A. Baldwin, J. M. Levitt, F. Tian, L. A. Stucenski, M. Hunter, Y. L. Kim, V. Backman, M. Feld, K. Munger, and I. Georgakoudi, "Endogenous optical biomarkers of normal and human papillomavirus immortalized epithelial cells," Int J Cancer **122**, 363-371 (2008).

14. H. Fang, M. Ollero, E. Vitkin, L. M. Kimerer, P. B. Cipolloni, M. M. Zaman, S. D. Freedman, I. J. Bigio, I. Itzkan, E. B. Hanlon, and L. T. Perelman, "Noninvasive Sizing of Subcellular Organelles With Light Scattering Spectroscopy," IEEE J. Sel. Top. Quantum Electron. **9**, 267-276 (2003).

15. L. T. Perelman, V. Backman, M. Wallace, G. Zonios, R. Manoharan, A. Nusrat, S. Shields, M. Seiler, C. Lima, T. Hamano, I. Itzkan, J. V. Dam, J. M. Crawford, and M. S. Feld, "Observation of Periodic Fine Structure in Reflectance from Biological Tissue: A New Technique for Measuring Nuclear Size Distribution," Phys. Rev. Lett. **80**, 627-630 (1998).

16. Y. L. Kim, Y. Liu, R. K. Wali, H. K. Roy, M. J. Goldberg, A. K. Kromin, K. Chen, and V. Backman, "Simultaneous measurement of angular and spectral properties of light scattering for characterization of tissue microarchitecture and its alteration in early precancer," IEEE J. Sel. Top. Quantum Electron. **9**, 243-256 (2003).

17.   J. R. Mourant, T. M. Johnson, S. Carpenter, A. Guerra, T. Aida, and J. P. Freyer, "Polarized angular dependent spectroscopy of epithelial cells and epithelial cell nuclei to determine the size scale of scattering structures," J. Biomed. Opt. **7**, 378–387 (2002).

18.   A. Curry, G. Nusz, A. Chilkoti, and A. Wax, "Substrate effect on refractive index dependence of plasmon resonance for individual silver nanoparticles observed using darkfield microspectroscopy," Opt. Express **13**, 2668-2677 (2005).

19.   J. P. Ogilvie, E. Beaurepaire, A. Alexandrou, and M. Joffre, "Fourier-transform coherent anti-Stokes Raman scattering microscopy," Opt. Lett. **31**, 480-482 (2006).

20.   K. J. Chalut, L. A. Kresty, J. W. Pyhtila, R. Nines, M. Baird, V. E. Steele, and A. Wax, "In situ Assessment of Intraepithelial Neoplasia in Hamster Trachea Epithelium Using Angle-Resolved Low-Coherence Interferometry," Cancer Epidemiol Biomarkers Prev **16**, 223-227 (2007).

21.   C. Yang, L. T. Perelman, A. Wax, R. R. Dasari, and M. S. Feld, "Feasibility of field-based light scattering spectroscopy," J. Biomed. Opt. **5**, 138–143 (2000).

22.   H. Fang, L. Qiu, E. Vitkin, M. M. Zaman, C. Andersson, S. Salahuddin, L. M. Kimerer, P. B. Cipolloni, M. D. Modell, B. S. Turner, S. E. Keates, I. Bigio, I. Itzkan, S. D. Freedman, R. Bansil, E. B. Hanlon, and L. T. Perelman, "Confocal light absorption and scattering spectroscopic microscopy," Appl Opt **46**, 1760-1769 (2007).

23.   R. Dzakpasu, and D. Axelrod, "Dynamic light scattering microscopy. A novel optical technique to image submicroscopic motions. II: Experimental applications," Biophys J **87**, 1288-1297 (2004).

24.   R. K. Wali, H. K. Roy, Y. L. Kim, Y. Liu, J. L. Koetsier, D. P. Kunte, M. J. Goldberg, V. Turzhitsky, and V. Backman, "Increased microvascular blood content is an early event in colon carcinogenesis," Gut **54**, 654-660 (2005).

25.   A. V. Kyrylyuk, and A. V. Zatovsky, "Light scattering from solutions of nonspherical particles exposed to an external electric field," Journal of Molecular Liquids **120**, 55-57 (2005).

26.   P. H. Kaye, "Spatial light-scattering analysis as a means of characterizing and classifying non-spherical particles," Measurement Science and Technology, 141 (1998).

27.   G. N. Constantinides, D. Gintides, S. E. Kattis, K. Kiriaki, C. A. Paraskeva, A. C. Payatakes, D. Polyzos, S. V. Tsinopoulos, and S. N. Yannopoulos, "Computation of Light Scattering by Axisymmetric Nonspherical Particles and Comparison with Experimental Results," Appl. Opt. **37**, 7310-7319 (1998).

28.   O. Kusmartseva, and P. R. Smith, "Robust method for non-sphere detection by photon correlation between scattered polarization states," Meas. Sci. Technol. , 336 (2002).

29.   J. P. Barton, "Light scattering calculations for irregularly shaped axisymmetric particles of homogeneous and layered compositions," Meas. Sci. Technol. , 151 (1998).

30.   N. N. Boustany, R. Drezek, and N. V. Thakor, "Calcium-induced alterations in mitochondrial morphology quantified in situ with optical scatter imaging," Biophys J **83**, 1691-1700 (2002).

31.   L. J. Hornbeck, "Deformable-Mirror Spatial Light Modulators," Spatial Light Modulators and Applications III **1150**, 86-102 (1989).

32.   M. Fulwyler, Q. S. Hanley, C. Schnetter, I. T. Young, E. A. Jares-Erijman, D. J. Arndt-Jovin, and T. M. Jovin, "Selective Photoreactions in a Programmable Array Microscope (PAM): Photoinitiated Polymerization, Photodecaging, and Photochromic Conversion," Cytometry A **67**, 68-75 (2005).

33.   L. J. Hornbeck, "Current status of the digital micromirror device (DMD) for projection television applications," in *Electron Devices Meeting, 1993. IEDM '93. Technical Digest., International*, (1993), pp. 381-384.

34.   M. R. Douglass, "Lifetime estimates and unique failure mechanisms of the Digital Micromirror Device (DMD)," in *Reliability Physics Symposium Proceedings, 1998. 36th Annual. 1998 IEEE International*, (1998), pp. 9-16.

35.	C. MacAulay, and A. Dlugan, "Use of digital micro mirror devices in quantitative microscopy," Proc. SPIE **3260**, 201-206 (1998).

36.	A. L. P. Dlugan, C. E. MacAulay, and P. M. Lane, "Improvements to Quantitative Microscopy Through the Use of Digital Micromirror Devices," Proc. SPIE **3921**, 6-11 (2000).

37.	S.-H. Chao, T. T. H. Ren, S. A. Gales, M. R. Holl, S. C. McQuaide, and D. R. Meldrum, "Automated digital light modulation microscope (DLMM) for living cell array analysis: pattern recognition and spatial alignment," in *Biomedical Robotics and Biomechatronics, 2006. BioRob 2006. The First IEEE/RAS-EMBS International Conference on*, (2006), pp. 977-981.

38.	M. Liang, R. L. Stehr, and A. W. Krause, "Confocal pattern period in multiple-aperture confocal imaging systems with coherent illumination," Opt. Lett. **22**, 751-753 (1997).

39.	Q. S. Hanley, P. J. Verveer, M. J. Gemkow, D. Arndt-Jovin, and T. M. Jovin, "An optical sectioning programmable array microscope implemented with a digital micromirror device," Journal of Microscopy **196**, 317-331 (1999).

40.	V. Bansal, S. Patel, and P. Saggau, "High-speed addressable confocal microscopy for functional imaging of cellular activity," Journal of Biomedical Optics **11**, 034003-034009 (2006).

41.	P. M. Lane, A. L. P. Dlugan, R. Richards-Kortum, and C. E. MacAulay, "Fiber-optic confocal microscopy using a spatial light modulator," Opt. Lett. **25**, 1780-1782 (2000).

42.	D. M. Rector, D. M. Ranken, and J. S. George, "High-performance confocal system for microscopic or endoscopic applications," Methods **30**, 16–27 (2003).

43.	C. Zhang, P. S. Huang, and F.-P. Chiang, "Microscopic Phase-Shifting Profilometry Based on Digital Micromirror Device Technology " Appl. Opt. **41**, 5896-5904 (2002).

44.	T. Fukano, and A. Miyawaki, "Whole-field fluorescence microscope with digital micromirror device: imaging of biological samples," Appl. Opt. **42**, 4119-4124 (2003).

45.	D. J. Cuccia, F. Bevilacqua, A. J. Durkin, F. R. Ayers, and B. J. Tromberg, "Quantitation and mapping of tissue optical properties using modulated imaging," Journal of Biomedical Optics **14**, 024012 (2009).

46.	A. C. Bovik, M. Clark, and W. S. Geisler, "Multichannel texture analysis using localized spatial filters," Pattern Analysis and Machine Intelligence, IEEE Transactions on **12**, 55-73 (1990).

47.	A. K. Jain, N. K. Ratha, and S. Lakshmanan, "Object detection using gabor filters," Pattern Recognition **30**, 295-309 (1997).

48.	T. P. Weldon, W. E. Higgins, and D. F. Dunn, "Gabor filter design for multiple texture segmentation," Optical Engineering **35**, 2852-2863 (1996).

49.	N. N. Boustany, Y. C. Tsai, B. Pfister, W. M. Joiner, G. A. Oyler, and N. V. Thakor, "BCL-xL-dependent light scattering by apoptotic cells," Biophys J **87**, 4163-4171 (2004).

50.	B. Beauvoit, T. Kitai, and B. Chance, "Contribution of the mitochondrial compartment to the optical properties of the rat liver: a theoretical and practical approach," Biophys J **67**, 2501-2510 (1994).

51.	B. Beauvoit, S. M. Evans, T. W. Jenkins, E. E. Miller, and B. Chance, "Correlation Between the Light Scattering and the Mitochondrial Content of Normal Tissues and Transplantable Rodent Tumors," Analytical Biochemistry **226**, 167-174 (1995).

52.	N. N. Danial, and S. J. Korsmeyer, "Cell death: critical control points," Cell **116**, 205-219 (2004).

53.	A. L. Lehninger, "Reversal of Thyroxine-induced Swelling of Rat Liver Mitochondria by Adenosine Triphosphate," The Journal of Biological Chemistry **234**, 2187-2195 (1959).

54.	L. Packer, "Metabolic and Structural States of Mitochondria," The Journal of Biological Chemistry **235**, 242-249 (1960).

55. C. R. Hackenbrock, "Ultrastructural bases for metabolically linked mechanical acivity in mitochondria I.," The Journal of Cell Biology **30**, 269-297 (1966).

56. L. Packer, "Energy-Linked Low Amplitude Mitochondrial Swelling," in *Methods in Enzymology, Vol. 10*, R. W. Estabrook, and M. E. Pullman, eds. (Academic Press, New York, 1967), pp. 685-697.

57. R. A. Harris, M. A. Asbell, J. Asai, W. W. Jolly, and D. E. Green, "The Conformational Basis of Energy Transduction in Membrane Systems. V. Measurement of Configurational Changes by Light Scattering," Archives of Biochemistry and Biophysics **132**, 545-560 (1969).

58. D. R. Hunter, R. A. Haworth, and J. H. Southward, "Relationship between Configuration, Function, and Permeability in Calcium-treated Mitochondria," The Journal of Biological Chemistry **251**, 5069-5077 (1976).

59. L. Scorrano, M. Ashiya, K. Buttle, S. Weiler, S. A. Oakes, C. A. Mannella, and S. J. Korsmeyer, "A Distinct Pathway Remodels Mitochondrial Cristae and Mobilizes Cytochrome C during Apoptosis," Developmental Cell **2**, 55-67 (2002).

60. A. Olichon, L. Baricault, N. Gas, E. Guillou, A. Valette, P. Belenguer, and G. Lenaers, "Loss of OPA1 Perturbates the Mitochondrial Inner Membrane Structure and Integrity, Leading to Cytochrome c Release and Apoptosis," The Journal of Biological Chemistry **278**, 7743-7746 (2003).

61. C. A. Mannella, "The relevance of mitochondrial membrane topology to mitochondrial function," Biochimica et Biophysica Acta **1762**, 140-147 (2006).

62. S. Cipolat, T. Rudka, D. Hartmann, V. Costa, L. Serneels, K. Craessaerts, K. Metzger, C. Frezza, W. Annaert, L. D'Adamio, C. Derks, R. Dejaegere, L. Pellegrini, R. D'Hooge, L. Scorrano, and B. DeStrooper, "Mitochondrial Rhomboid PARL Regulates Cytochrome c Release during Apoptosis via OPA1-Dependent Cristae Remodeling," Cell **126**, 163-175 (2006).

63. C. Frezza, S. Cipolat, O. M. d. Brito, M. Micaroni, G. V. Beznoussenko, T. Rudka, D. Bartoli, R. S. Polishuck, N. N. Danial, B. DeStrooper, and L. Scorrano, "OPA1 Controls Apoptotic Cristae Remodeling Independently from Mitochondrial Fusion," Cell **126**, 177-189 (2006).

64. C. A. Mannella, "Structure and dynamics of the mitochondrial inner membrane crsitae," Biochimica et Biophysica Acta **1763**, 542-548 (2006).

65. G. Schuele, E. Vitkin, P. Huie, C. O'Connell-Rodwell, D. Palanker, and L. T. Perelman, "Optical spectroscopy noninvasively monitors response of organelles to cellular stress," J. Biomed. Opt. **10**, 051404-051401 (2005).

66. B. Beauvoit, and B. Chance, "Time-Resolved Spectroscopy of mitochondria, cells and tissues under normal and pathological conditions," Molecular and Cellular Biochemistry **184**, 445-455 (1998).

67. L. J. Johnson, W. Chung, D. F. Hanley, and N. V. Thakor, "Optical Scatter Imaging Detects Mitochondrial Swelling in Living Tissue Slices," NeuroImage **17**, 1649-1657 (2002).

68. M. Gonzalez-Garcia, R. Perez-Ballestero, L. Ding, L. Duan, L. H. Boise, C. B. Thompson, and G. Nunez, "bcl-XL is the major bcl-x mRNA form expressed during murine development and its product localizes to mitochondria," Development **120**, 3033-3042 (1994).

69. K. Degenhardt, G. Chen, T. Lindsten, and E. White, "BAX and BAK mediate p53-independent suppression of tumorigenesis," Cancer Cell **2**, 193-203 (2002).

70. T. Kaufmann, S. Schlipf, J. Sanz, K. Neubert, R. Stein, and C. Borner, "Caharacterization of the signal that directs Bcl-xL, but not Bcl-2, to the mitochondrial outer membrane," The Journal of Cell Biology **160**, 53-64 (2003).

71. C. Borner, I. Martinou, C. Mattmann, M. Irmler, E. Schaerer, J.-C. Martinou, and J. Tschopp, "The Protein bcl-2a Does Not Require Membrane Attachment, but Two Conserved Domains to Suppress Apoptosis," The Journal of Cell Biology **126**, 1059-1068 (1994).

72.   A. Cuconati, and E. White, "Viral homologs of BCL-2: role of apoptosis in the regulation of virus infection," Genes and Development **16**, 2465-2478 (2002).

73.   A. P. Halestrap, "The regulation of the matrix volume of mammalian mitochondria in vivo and in vitro and its role in the control of mitochondrial metabolism.," Biochimica et Biophysica Acta **973**, 355-382 (1989).

74.   R. A. Eliseev, J. D. Salter, K. K. Gunter, and T. E. Gunter, "Bcl-2 and tbid proteins conter-regulate mitochondrial potassium transport," Biochimica et Biophysica Acta **1604**, 1-5 (2003).

75.   A. J. Kowaltowski, R. G. Cosso, C. B. Campos, and G. Fiskum, "Effect of Bcl-2 Overexpression on Mitochondrial Structure and Function," The Journal of Biological Chemistry **277**, 42802-42807 (2002).

76.   C. D. Stoner, and H. D. Sirak, "Adenine nucleotide-induced contraction of the inner mitochondrial membrane, 1. General characterization," The Journal of Cell Biology **56**, (1973).

77.   C. D. Stoner, and H. D. Sirak, "Adenine nucleotide-induced contraction of the inner mitochondrial membrane, 2. Effect of bongkrekic acid," The Journal of Cell Biology **56**, 65-73 (1973).

78.   M. Klingenberg, K. Grebe, and B. Scherer, "Opposite effects of bongkrekic acid and atractyloside on the adenine nucleotides induced mitochondrial volume changes and on the efflux of adenine nucleotides," FEBS Letters **16**, 253-256 (1971).

79.   M. Klingenberg, "The ADP-ATP Translocation in Mitochondria, a Membrane Potential Controlled Transport," The Journal of Membrane Biology **56**, 97-105 (1980).

80.   M. Das, J. E. Parker, and A. P. Halestrap, "Matrix volume measurements challenge the existence of diazoxide/glibencamide-sensitive K ATP channels in rat mitochondria," Journal of Physiology **547**, 893-902 (2003).

81.   T. Brustovetsky, N. Shalbuyeva, and N. Brustovetsky, "Lack fo manifestations of diazoxide/5-hydroxydecanoate-sensitive KATP channel in rat brain nonsynaptosomal mitochondria," Journal of Physiology **568**, 47-59 (2005).

82.   A. D. Beavis, R. D. Brannan, and K. D. Garlid, "Swelling and Contraction of the Mitochondrial Matrix," The Journal of Biological Chemistry **260**, 13424-13433 (1985).

83.   M. G. Vander-Heiden, N. S. Chandel, P. T. Schumacker, and C. B. Thompson, "Bcl-xL Prevents Cell Death following Growth Factor Withdrawal by Facilitating Mitochondrial ATP/ADP Exchange," Molecular Cell **3**, 159-167 (1999).

84.   A.-S. Belzacq, H. L. A. Vieira, F. Verrier, G. Vandecasteele, I. Cohen, M.-C. Prevost, E. Larquet, F. Pariselli, P. X. Petit, A. Kahn, and R. Rizzuto, "Bcl-2 and Bax Modulate Adenine Nucleotide Translocase Activity," Cancer Research **63**, 541-546 (2003).

85.   E. Doran, and A. P. Halestrap, "Cytochrome c release from isoloated rat liver mitochondria can occur independently of outer-membrane rupture: possible role of contact sites," Biochemical Journal **348**, 343-350 (2000).

86.   K. Degenhardt, R. Sundararajan, T. Lindsten, C. Thompson, and E. White, "Bax and Bak independently promote cytochrome C release from mitochondria," J Biol Chem **277**, 14127-14134 (2002).

87.   R. M. Pasternack, Z. Qian, J.-Y. Zheng, and N. N. Boustany, "Measurement of subcellular morphology by light scatter filtering with a digital micromirror device," in *Biomedical Applications of Light Scattering III*, (SPIE, San Jose, CA, USA, 2009), pp. 71871E-71878.

88.   S. Wasiak, R. Zunino, and H. M. McBride, "Bax/Bak promote sumoylation of DRP1 and its stable association with mitochondria during apoptotic cell death," J Cell Biol **177**, 439-450 (2007).

89.   J. G. Daugman, "Uncertainty relation for resolution in space, spatial frequency, and orientation optimized by two-dimensional visual cortical filters," J. Opt. Soc. Am. A **2**, 1160-1169 (1985).

90. R. M. Pasternack, Z. Qian, J.-Y. Zheng, D. N. Metaxas, E. White, and N. N. Boustany, "Measurement of subcellular texture by optical Gabor-like filtering with a digital micromirror device," Opt. Lett. **33**, 2209-2211 (2008).

91. N. Otsu, "A Threshold Selection Method from Gray-Level Histograms," Systems, Man and Cybernetics, IEEE Transactions on **9**, 62-66 (1979).

92. R. M. Haralick, and L. G. Shapiro, "Computer and Robot Vision," Addison-Wesley **1**, 158-205 (1992).

93. V. D. Boomgaard, and V. Balen, "Image Transforms Using Bitmapped Binary Images," Computer Vision, Graphics, and Image Processing: Graphical Models and Image Processing **54**, 254-258 (1992).

94. J. D. Wilson, W. J. Cottrell, and T. H. Foster, "Index-of-refraction-dependent subcellular light scattering observed with organelle-specific dyes," Journal of Biomedical Optics **12**, 014010 (2007).

95. C. Gelinas, and E. White, "BH3-only proteins in control: specificity regulates MCL-1 and BAK-mediated apoptosis," Genes Dev **19**, 1263-1268 (2005).

96. M. Suzuki, R. J. Youle, and N. Tjandra, "Structure of Bax: coregulation of dimer formation and intracellular localization," Cell **103**, 645-654 (2000).

97. S.-Y. Jeong, B. Gaume, Y.-J. Lee, Y.-T. Hsu, S.-W. Ryu, S.-H. Yoon, and R. J. Youle, "Bcl-xL sequesters its C-terminal membrane anchor in soluble, cytosolic homodimers," The EMBO Journal **23**, 2146-2155 (2004).

98. S. B. Berman, Y. B. Chen, B. Qi, J. M. McCaffery, E. B. Rucker, 3rd, S. Goebbels, K. A. Nave, B. A. Arnold, E. A. Jonas, F. J. Pineda, and J. M. Hardwick, "Bcl-x L increases mitochondrial fission, fusion, and biomass in neurons," J Cell Biol **184**, 707-719 (2009).

99. P. Delivani, C. Adrain, R. C. Taylor, P. J. Duriez, and S. J. Martin, "Role for CED-9 and Egl-1 as regulators of mitochondrial fission and fusion dynamics," Mol Cell **21**, 761-773 (2006).

100. H. Li, Y. Chen, A. F. Jones, R. H. Sanger, L. P. Collis, R. Flannery, E. C. McNay, T. Yu, R. Schwarzenbacher, B. Bossy, E. Bossy-Wetzel, M. V. Bennett, M. Pypaert, J. A. Hickman, P. J. Smith, J. M. Hardwick, and E. A. Jonas, "Bcl-xL induces Drp1-dependent synapse formation in cultured hippocampal neurons," Proc Natl Acad Sci U S A **105**, 2169-2174 (2008).

Curriculum Vitae

Jing-Yi Zheng

Education

Jun 1999   **National Tsing Hua University**, Hsinchu, Taiwan
Bachelor of Science in Nuclear Science
GPA 3.5/4.0

Jun 2001   **National Tsing Hua University**, Hsinchu, Taiwan
Master of Nuclear Science
"The Optimization of cDNA Microarray and Its Preliminary Studies on The Applications of Gene expression of MRC-5 Exposed to Ultraviolet"
Advised by Dr. Ian C. Hsu
GPA 4.0/4.0

Oct 2009   **Rutgers University**, New Brunswick, New Jersey
Candidate for Ph. D. Biomedical Engineering
"Microscopy with Spatial Filtering for Sorting Particles and Monitoring Subcellular Morphology"
• Develop an optical scatter imaging (OSI) based on light scattering and spatial filtering to non-invasively track real-time changes in particle morphology with sub-micron resolution in situ.
Advised by Dr. Nada Boustany
GPA 3.61/4.0

Experience

01/02-12/02   **Research Assistant**
Department of Molecular Pharmacology, UMASS Medical School, Worcester, MA

01/03-06/03   **Research Associate**
Department of Pharmacology, UMDNJ-Robert Wood Johnson Medical School, Piscataway, NJ

09/07-12/08   **Teaching Assistant**
Department of Biomedical Engineering, Rutgers University, Piscataway, NJ

Publications

- **J.Y. Zheng**, Y.C. Tsai, P. Kadimcherla, R. Zhang, J. Shi, G.A. Oyler, N.N. Boustany, "The C-terminal transmembrane domain of Bcl-x_L mediates changes in mitochondrial morphology", Biophysical J., 94 (1): 286-297, 2008.

- R.M. Pasternack, Z. Qian, **J.Y. Zheng**, D.N. Metaxas, E. White, N. N. Boustany, "Measurement of subcellular texture by optical Gabor-like filtering with a digital micromirror device", Opt Lett., 33 (19): 2209-11, 2008.

- R. M. Pasternack, Z. Qian, **J.Y. Zheng**, D. N. Metaxas, and N. N. Boustany, "Highly sensitive size discrimination of sub-micron objects using optical Fourier processing based on two-dimensional Gabor filters", Opt. Express **17**, 12001-12012 (2009).

- **J.Y. Zheng,** R. M. Pasternack, N. N. Boustany, "Optical Scatter Imaging with a Digital Micromirror Device", Opt. Express, Submitted (2009).